UNIVERSITÀ DEGLI STUDI DELLA CALABRIA

Facoltà di Scienze Matematiche, Fisiche e Naturali

Dottorato di Ricerca in Fisica

XIX Ciclo
Settore Scientifico-Disciplinare: FIS/05

TESI di DOTTORATO

Complexity in Astrophysical and Laboratory Plasmas

Sergio Servidio

Supervisori:
prof. Vincenzo Carbone
dott. Leonardo Primavera

Coordinatore:
prof. Gennaro Chiarello

2003 — 2006

to my wife ...

Introduction

A complex system is any system featuring a large number of interacting components (agents, processes, elements, etc.) whose aggregate activity is nonlinear (not derivable from the summations of the activity of individual components) and typically exhibits hierarchical self–organization processes [1].
There are many definitions of complexity, therefore many natural, artificial and abstract objects or networks can be considered to be complex systems, and their study (complexity science) is highly interdisciplinary. Apart for classical media like fluid flows or continuous physical systems, examples of complex systems include some different topics in many areas of science and social systems [2–4].
The complexity in nature can manifests itself through the occurrence of *chaos* [5, 6], *turbulence* [7, 8] and *bursty phenomena* [9]. Nonlinear couplings, self–organization processes and long range interaction can generate several kind of objects like: vortexes, nonlinear waves, instabilities, solitons and so on [10]. By the way, the point of view that complex phenomena have a complicate mathematical description is not true, in fact intrinsic nonlinearities can make complex phenomena be described also by simple equations. In specific circumstances, for example, they may exhibit low dimensional behavior. Traditional methods of mathematical modeling are adept at handling systems with few degrees of freedom that interact strongly, such as the paradigmatic simple harmonic oscillator, while statistical methods are useful for systems with very many degrees of freedom all of which interact weakly, such as a box of gas.
Plasmas in nature and in laboratory are an example of systems where complexity manifests through the occurrence of turbulence, chaos and bursty phenomena. In particular, turbulence is often defined as the most interesting and yet unsolved phenomenon of classical physics [11]. Being ubiquitous in nature, turbulent dynamics can be observed everywhere in fluids, for exam-

ple in laboratory and atmospheric flows [11,12] as well as in astrophysical [13] and laboratory plasmas [14]. Of course numerical simulations, supported by actual multi–processors computers, give a great contribution in understanding and analyzing turbulent flows [15].
In this thesis we investigate some phenomena in plasmas, from astrophysical to laboratory, seen as a complex system. Modeling the plasma state, we can get some insight into the nature of the problem and, often, into a physical explanation of some different processes. The plan of the thesis is as follows.
In Chapter 1 we will describe briefly laboratory and space plasmas, in particular toroidal fusion reactors, linear devices and the Sun–Earth system.
In Chapter 2 we will study small-scale fluctuations in turbulence. By using direct numerical simulation of Hall Magnetohydrodynamics equations we investigate the role of Hall effect in the dynamical behaviour of the turbulent state of the system. Our results are strongly compatible with observations of the Cluster satellite in the magnetopause boundary layer.
In Chapter 3 we describe and analyze the bursty behaviour observed both in toroidal and linear plasma devices. We named this phenomenon "bursty turbulence". We numerically investigate dynamics of two–dimensional $\mathbf{E}\times\mathbf{B}$ turbulence in a polar geometry, similar to a poloidal section of laboratory plasmas. By using forcing input of charges we generate bursts (or *blobs*) that propagate from the core to the boundaries of the simulation domain. Properties of this kind of turbulence are then analyzed and discussed.
In Chapter 4 is studied the complex picture of the Reversed–Field Pinch (RFP) turbulence, in which turbulent fields evolve stochastically over a broad range of modes. Sometimes the spectral structure of the magnetic field is dominated by few poloidal and toroidal modes. By using a simplified model of the Reduced Magnetohydrodynamics (RMHD), obtained from a Galerkin approximation, we will show how the nonlinear dynamic of RMHD turbulence is able to generate states similar to that observed in several RFPs.

Contents

1 Laboratory and Space Plasmas **9**

1.1 Space plasmas: the Sun–Earth system 10

1.1.1 The turbulent layer of the magnetopause 11

1.2 Laboratory plasmas 15

2 Nonlinear Dynamics of Hall MHD Equations: Magnetosonic Fluctuations as Observed in Space Plasmas **23**

2.1 Kelvin–Helmholtz Instability at the MP 25

2.2 Observations of magnetosonic structures in space plasmas . . . 27

2.3 The compressible Hall Magnetohydrodynamics 32

2.3.1 Hall MHD equations in a dimensionless form 33

2.4 The numerical simulation 35

2.4.1 The numerical technique 40

2.5 Results of the simulations 43

2.5.1 The starting point of the energy cascade 43

2.5.2 Fully developed magnetosonic turbulence 47

2.5.3 Comparisons between Hall MHD and MHD 55

2.6 Conclusions 58

3 "Bursty Turbulence" in Laboratory Plasmas **59**

3.1 Intermittent turbulence in laboratory plasmas 60

3.2 A simple "$\mathbf{E} \times \mathbf{B}$" model 68

3.3 The third–order mixed correlations 71

3.4 Numerical simulation of forced bursty turbulence 73

3.5 Statistical properties of the "$\mathbf{E} \times \mathbf{B}$ turbulence" 79

3.5.1 The radial current 80

3.5.2 Statistics of the bursts energy, waiting times and duration times 81
3.5.3 The third–order mixed correlations 84
3.6 Conclusions 86

4 Nonlinear Phenomena in RFP Devices: Multiple–Helicity and Quasi–Single–Helicity States 89
4.1 Magnetic turbulence in RFP devices 90
4.2 Observations of Quasi–Single–Helicity states 93
4.3 The MHD approach 96
4.4 A simple model: inviscid Reduced Magnetohydrodynamics . . 96
4.4.1 The equilibrium ensemble of 2D–MHD 99
4.5 The numerical technique 100
4.6 The appearance of QSH states in RMHD 102
4.7 Conclusions 108

Chapter 1

Laboratory and Space Plasmas

There are three classic states of matter: *solid*, *liquid*, and *gas*; however, *plasma* is considered by some scientists to be the *fourth state* of matter. Plasmas are gases composed mainly by charged particles and its dynamics is dominated essentially by electromagnetic forces. Generally speaking, a plasma is composed of a sufficient number of charged particles so that the gas, as a whole, exhibits a collective response to external electric and magnetic fields. In turn, the particles motion generates its own electromagnetic fields. This kind of interactions makes plasmas unique and fascinating complex systems.

Much of the impetus for the development of plasma physics over the second half of the twentieth century came from research into controlled thermonuclear fusion on the one hand and space plasma phenomena on the other. Fusion scientists are interested in plasmas for practical purposes and, in an effort to harness fusion energy on Earth, they study devices that create very hot plasmas confined by very strong magnetic fields. Fusion devices or, less frequently, linear devices, are used also for basic plasma processes investigations.

The state of plasma largely dominates the matter in space. For example, by studying processes that occur in the Earth's magnetosphere (where Earth's magnetic field has a greater influence than the Sun's interplanetary field), in interplanetary space, in the solar wind, and around other planets, we are better able to appreciate the important role of plasmas throughout the Universe.

In this thesis we will study complexities in three different magnetic plasma configurations: toroidal fusion reactors, linear laboratory plasmas and astro-

physical plasmas.

1.1 Space plasmas: the Sun–Earth system

The outer layers of the Sun and stars in general are made up of matter in an ionized state and from these regions winds blow through the interstellar space contributing, along with stellar radiation, to the ionized state of the interstellar gas. Thus, much of the matter in the Universe exist in the plasma state. The external regions of the Sun are characterized by a complex magnetic structure, composed of both closed (anchored on the photosphere) magnetic field lines. On the other hand, the strong pressure gradient between the hot ($\sim 10^6 K$) solar corona and the cold ($\sim 10K$) interstellar medium generates a flux of charged particles from the Sun to the heliosphere. This flux of particles is the *solar wind* (SW). For the SW the mean free path is ~ 1 AU (150 millions of kilometers), thus it is a highly non–collisional plasma. This implies that the solar magnetic field is frozen into the wind and is carried away from the Sun, thus contributing to the complex magnetic structure described above. Far away from the Sun that field is usually called the *interplanetary magnetic field* (IMF).
The Earth, as other solid objects in the solar system, is an obstacle to the SW and with its lower atmosphere forms a plasma–free *oasis* in a plasma universe. Due to the supersonic velocity of the SW, a standing shock wave, the *bow shock*, is formed in front of the Earth. Downstream of the bow shock the thermalized solar wind is decelerated to subsonic velocities flowing around the Earth, this region is named *magnetosheath* (MSH). Since the presence of the Earth's magnetic field, the description of the SW–Earth interaction is very complicated. Due to the frozen–in condition, the interplanetary and terrestrial magnetic fields cannot mix and a boundary layer called *magnetopause* (MP) develops between the two fields. In the anti–sunward direction the Earth's magnetic field is confined in a comet–like cavity, the *magnetosphere* (MSP), at which the solar wind is deflected by the geomagnetic field. The outer boundary of the MSP occurs at about 10 R_E, where R_E denotes the Earth's radius. The geomagnetic field is swept into space in the form of a huge cylinder, many millions of kilometers in length, known as the *magnetotail*. The MP separates cold (~ 100 eV) and dense (~ 30 cm^{-3}) plasmas embedded in the magnetosheath magnetic field lines from hot (~ 1 keV) and tenuous (~ 1 cm^{-3}) plasmas in the magnetosphere. Fig. 1.1 shows a

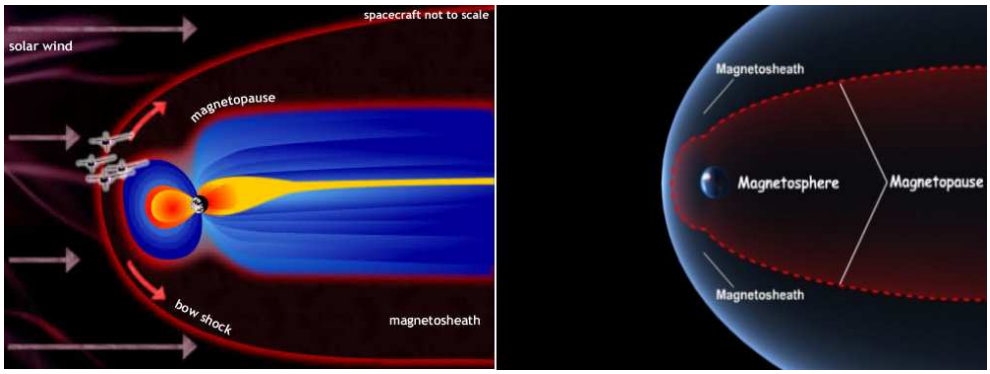

Figure 1.1: A sketch of the *solar wind–Earth* system (left and right both). The bow shock separates the supersonic solar wind from the shocked and thermalized plasma, namely the magnetosheath (MSH). Going toward the Earth, then, the magnetopause (MP) is the layer that separates MSH from the region dominated by the Earth magnetic field, namely the magnetosphere (MSP).

cartoon of the SW–Earth interaction. The interaction between the MSP and the MSH is of great interest for scientific investigations, due to the presence of a large amount of nonlinear phenomena as: plasma instabilities [16–18], vortex generation and merging [10], nonlinear waves [14], emergence of coherent structures [15], and in general for the occurrence of a wide spectrum of large–amplitude fluctuations [19, 20].

1.1.1 The turbulent layer of the magnetopause

The MP is a surface whose location and shape are locally prescribed by the balance between solar wind and magnetospheric pressures. Across the MP the magnetic field changes orientation and magnitude, thus the MP is embedded in a current layer. In normal conditions the MP is an impenetrable boundary due to the frozen–in condition for both the solar and the magnetospheric plasmas. Though valid, this picture provides only a first order approximation. There is in fact much evidence that solar wind plasma penetrates through the MP. Also magnetospheric plasma has been observed outside the magnetopause in the magnetosheath boundary layer. Several processes have been proposed to explain this transfer of plasma across the MP [21], but the problem is not yet completely understood.

Figure 1.2: Artist's impression of the Cluster spacecraft.

In the last years decisive advances in the magnetospheric physics were obtained from the multi–point *Cluster project*[1] [22]. It is a SW–magnetospheric mission with four identical spacecrafts in which they move along their orbit in a *tetrahedrical* configuration with variable inter–spacecraft separation. Cluster satellite so allows the study of structures such as magnetospheric boundaries and was the first satellite that gave informations about currents. The structure of satellites allow us to obtain several interesting information about plasma dynamics, and is currently investigating the small–scale structure of the Earth's plasma environment, such as those involved in the interaction between the SW and the magnetospheric plasma [23], in global magnetotail dynamics [24], in cross–tail currents [25], and in the formation and dynamics of the neutral line and of plasmoids [26]. In Fig. 1.2 an artistic representation of the 4–satellites system is shown. A sketch of Cluster orbit is shown in Fig. 1.3.
The MP is a turbulent "oscillating" boundary layer and when this bound-

[1]The Cluster mission was first proposed in November 1982 in response to an ESA Call for Proposals for the next series of science missions. The idea was developed into a proposal to study the cusp and the magnetotail regions of the Earth's magnetosphere with a polar orbiting mission. The Cluster idea developed into a proposal and then a mission. In 1996, Cluster was ready to be launched.

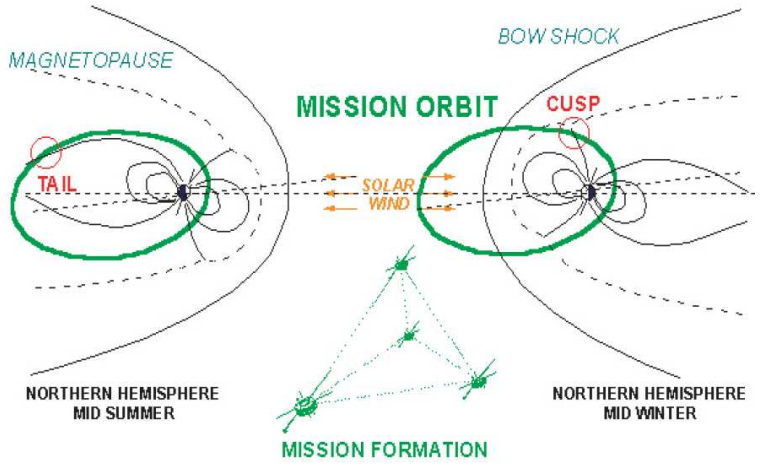

Figure 1.3: Cluster orbits in two different period of the year.

ary moves over a spacecraft, its instruments will record abrupt changes in magnetic field and plasma properties, but as the speed of the boundary motion is unknown a–priori, one cannot determine its thickness [27]. Using the timing of the crossings recorded by the four Cluster spacecraft, we can directly determine the orientation and velocity of the magnetopause, and from these informations we can calculate its thickness. Together with the known changes in the magnetic field across the current layer one can also compute the net electric current flowing within the MP. The MP thickness is highly variable, it ranges from 200 km in the sub–polar point to 3000 km in the dusk flank [28–31].
The dusk flank of the MP, as shown in Fig. 1.4, is characterized by the presence of strong gradients in the magnetic and velocity field, due to the strong difference between shocked solar wind and the Earth magnetic field region. Along with this magnetic field variation, due to a total pressure balance, a density gradient is usually observed at the same location or slightly shifted. Therefore, on a very short distance (a few Larmor radii), most parameters undergo discontinuities. All these discontinuities are able to trigger instabilities, and it has been supposed that these instabilities are the explanation of the increasing level of electromagnetic turbulence that is observed on the MP. The boundary regions are a fundamental piece of the system, since they are the gateway for energy and particles, but they are also the most difficult

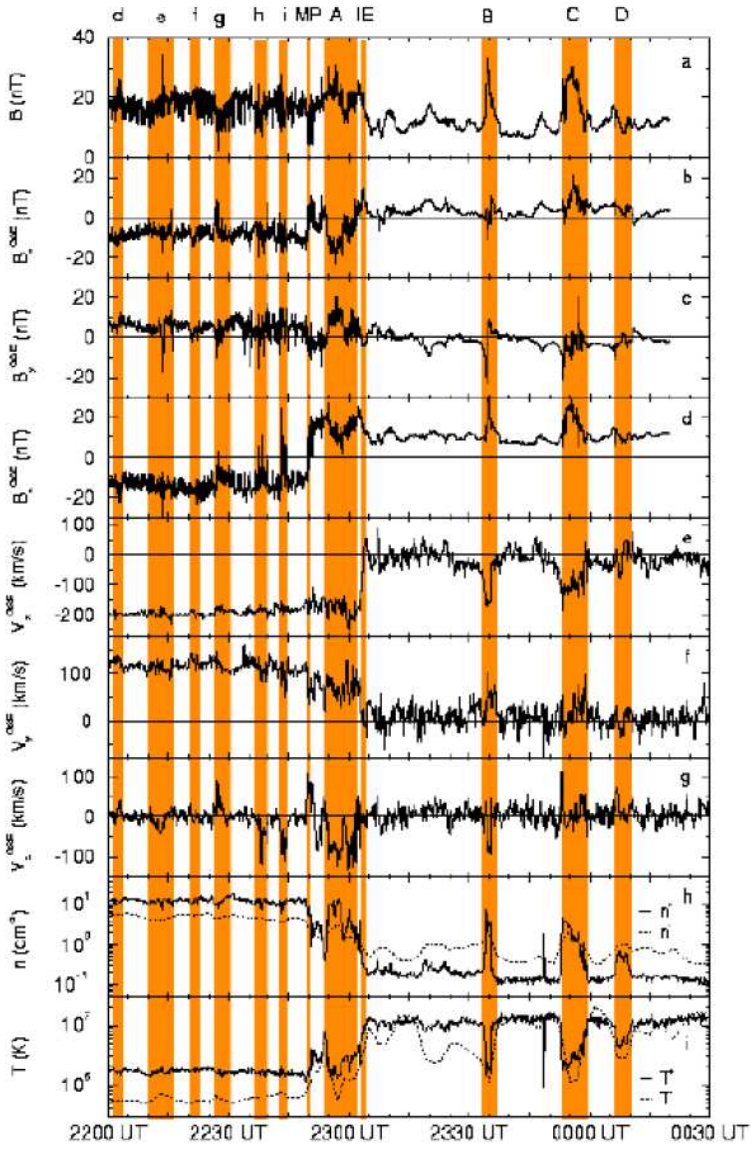

Figure 1.4: February 15–16, 1996: dusk side inbound crossing of the MP by Interball–Tail spacecraft. It's shown following Interball–Tail data: (a–d) the magnetic field magnitude and its GSE (Geocentric Solar Ecliptic reference system) components, (e–g) the GSE ion velocity components, (h) the ion and electron densities n^+ and n^-, and the ion and electron temperatures T^+ and T^-. The MP crossing (labeled 'MP' in the top figure) occurs near $22:50UT$ (*Universal Time*) and is identified by large magnetic field changes. This MP crossing is followed by four distinct transients (labeled A, B, C, and D), interpreted as the signature of high–amplitude solitary fluctuations [32].

regions to explore. The MP plays a key role in the exchanges between the solar wind and the Earth environment, and in this region many nonlinear phenomena were observed: magnetic field lines reconnection [33], Kelvin–Helmholtz instability [34–36], shock waves [37], plasma turbulence [38], and solitary traveling structures [39, 40]. The magnetospheric region is governed by a complex dynamics, and we will describe these nonlinear phenomena in Chapter 2.

1.2 Laboratory plasmas

Revived interest in plasma physics in the United States began in 1952 with the attempts of a program, then classified, known as *Project Sherwood* [41,42], to develop a controlled thermonuclear fusion reactor. Similar programs were started in England, France, and Russian about the same time. Since 1952, the development of a controlled fusion reactor began one of the more challenging practical applications of plasma physics. Nowadays several kind of plasma reactors exist, as for example: *Tokamak*, *Reversed–Field Pinch* (RFP), *Stellarator* and some *linear devices*.
A tokamak is a machine producing a toroidal ("doughnut–shaped") magnetic field for confining a plasma. The term tokamak is a transliteration of a Russian word *TOroidalnya KAmera ee MAgnetnaya Katushka* (toroidal chamber in magnetic coils)[2] [43]. The tokamak is characterized by azimuthal (rotational) symmetry and by the use of the plasma current to generate the helical component of the magnetic field necessary for a stable equilibrium. This can be contrasted to another toroidal magnetic confinement device, the *stellarator*, which has a discrete rotational symmetry and in which all of the confining magnetic fields are produced by external coils with a negligible current flowing through the plasma. Ions and electrons in a tokamak plasma are at very high temperatures and, correspondingly, have very significant velocities. Magnetic confinement fusion devices exploit the fact that charged particles in a magnetic field experience a Lorentz force and fall into spiral paths along the field lines. In order to produce continuous fusion reactions, the device must ensure that the hot plasma does not lose its particles from the core (hotter region). This is the well–known, yet unsolved, *confinement problem*.

[2]It was invented in the 1950s by Igor Yevgenyevich Tamm and Andrei Sakharov (who were in turn inspired by an original idea of O.A. Lavrent'ev).

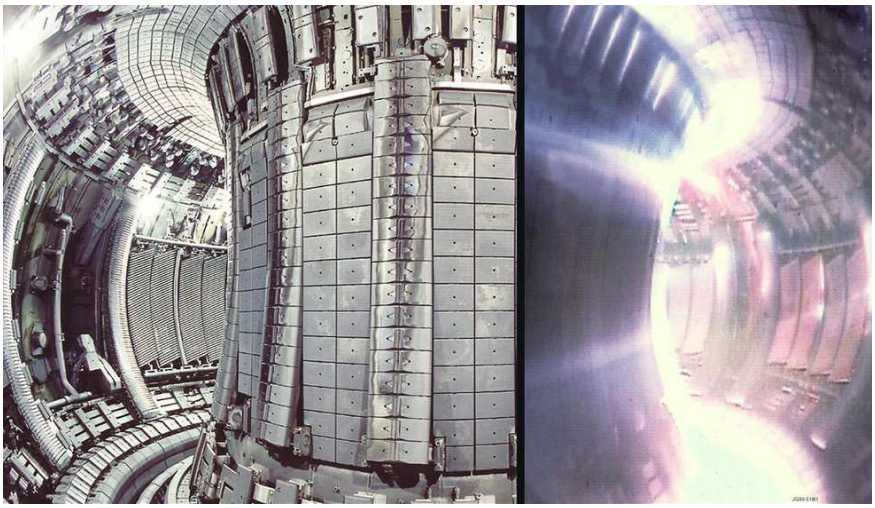

Figure 1.5: An image of the innerpart of the JET tokamak (left and right). On the left, the structure of the device is shown; on the right is displayed the plasma during a shot. The visible light–emitting areas are actually the coolest, since the hotter plasma in the middle of the tube emits X–rays.

In Fig. 1.5 the vacuum chamber of the JET tokamak[3] is shown. This is one of several kind of magnetic confinement devices and, at the present time, the leading candidate for generating fusion energy.
Generally in tokamaks, via a system of coils, a strong toroidal magnetic field is obtained, with a small (more or less zero) poloidal component, as shown in Fig. 1.6. The toroidal field effectively *stiffens* the plasma against instability. The most important idea of tokamaks is to obtain a more efficient equilibrium of plasmas, but in practice, numerous instabilities occur [44, 45], some of which are not yet fully understood [14].
Inside an operating fusion reactor, part of the energy generated is used to maintain a constant plasma temperature as fresh deuterium and tritium (typical fusion materials) are introduced. However, in the startup of a reactor, either initially or after a temporary shutdown, the plasma will have to be heated to its operating temperature greater than $10keV$ (over 100 million Celsius degrees). In current magnetic fusion experiments insufficient fusion

[3]Situated at Culham in the UK, the Joint European Torus (JET) is run as a collaboration between all European fusion organizations and with the participation of scientists from all the globe.

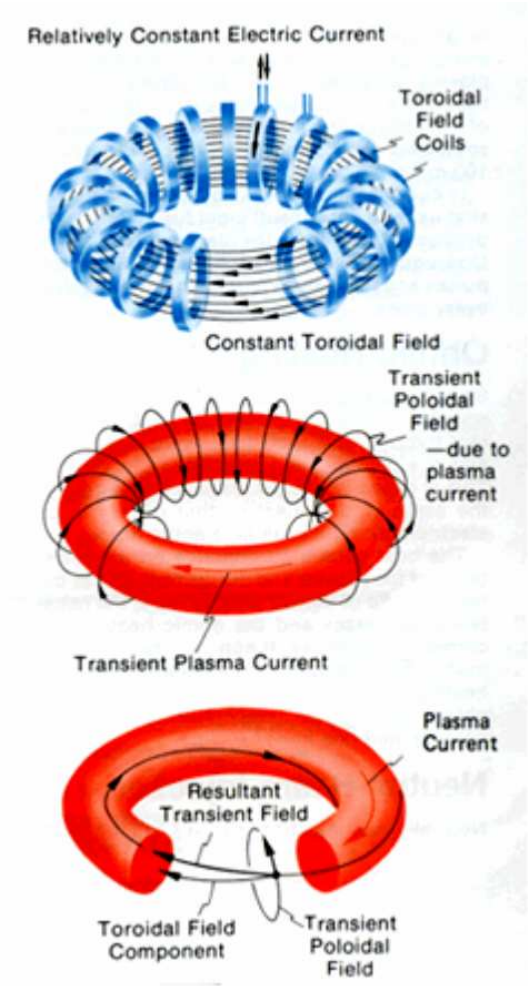

Figure 1.6: The tokamak system of coils (top panel), poloidal and toroidal currents (middle panel) and the resulting magnetic field configuration (bottom panel).

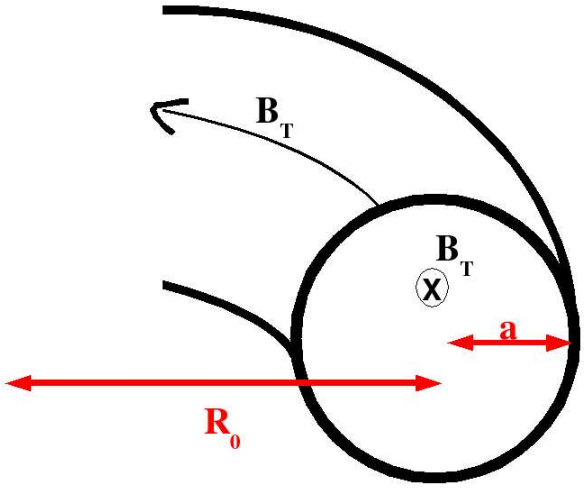

Figure 1.7: A sketch of the tokamak geometry. The tokamak configuration is characterized by the presence of a strong toroidal field B_T. R_0 and a are the major and the minor radius respectively.

energy is produced to maintain the plasma temperature and instabilities prevent operation. Consequently, the devices operate in short pulses and the plasma must be heated again in every pulse.
Here it is useful to define some plasma parameters that are frequently used. An important geometric parameter of tokamak configurations is the *aspect ratio*, *i. e.* the ratio between *major radius* R_0 and *minor radius* a, as sketched in Fig. 1.7. Generally, both R_0 and a have typical values that range from 0.1 to some meters. Typical aspect ratio values for toroidal plasma devices are listed in Table 1.1. The plasma parameter β is the ratio between kinetic pressure P_{kin} and magnetic pressure $B^2/2\mu_0$. In general, in laboratory plasmas the latter is higher than the former, thus the plasma β is very low, roughly $\beta \simeq 10^{-1}$. The safety factor

$$q(r) = \frac{rB_T(r)}{aB_P(r)} \tag{1.1}$$

where B_P and B_T are the poloidal and toroidal magnetic field respectively, measures the number of times a field line goes around a torus, the long way for each time around the short way.
Reversed–Field Pinches (RFPs) are one of the possible magnetic confinement alternative to the tokamak configuration. The RFP arrangement is

very similar to the one of tokamaks, but the device uses the electromagnetic properties of the plasma itself to self–sustain the confining magnetic field. RFP systems are being studied for possible low magnetic field, high plasma density confinement designs and to enhance understanding of the physics of toroidal confinement in operating regions that are outside the range of standard tokamak devices. The RFP configuration is less developed than the tokamak one but offers potential advantages. In fact it requires a much weaker magnetic field, which may result in a significant advantage for fusion reactors. However, the reduced magnetic field also reduces plasma stability and confinement and other problems can occur during plasma discharge.
The magnetic configuration is axisymmetric and the plasma is confined by a combination of a poloidal field, produced by the plasma current flowing around the torus, and a toroidal field, produced by currents flowing both in the plasma and in external coils (similar to tokamak's system shown in Fig. 1.6). Schematically, the RFP system is similar to a tokamak and consists of a toroidal vessel, in which the plasma is formed, surrounded by a toroidal winding that generates the initial toroidal field, and coupled to a coaxial transformer whose secondary winding is the plasma current. The configuration gets its name from the fact that the toroidal magnetic field in the outer region is reversed with respect to its direction in the plasma core, as shown in Fig. 1.8. Due to the inversion of B_T near the boundaries of the device, large amplitude fluctuations in magnetic and velocity fields are present and strong turbulent processes develop (*edge turbulence*).
The magnetic configuration of plasma confinement is characterized by the fact that the poloidal magnetic field B_P (or B_θ) is of the same order of magnitude of the toroidal component B_T (or B_ϕ), that is $\langle B_T \rangle \simeq \langle B_P \rangle$. In Table 1.1 some RFP devices and their aspect ratio parameters are reported.
Linear devices are magnetic configurations in which the plasma is confined by a linear magnetic field. With respect to tokamak and RFP the confinement in such devices is very reduced due to the loss of plasma at the boundaries of the camera. The mean goal of linear devices is to study plasma instabilities and other complex phenomena, using a simplified geometry with respect to toroidal magnetic structures. An example of linear device is LAPD[4] [46].

[4]The LArge Plasma Device (LAPD) is part of the Basic Plasma Science Facility (BaPSF) at the University of California, Los Angeles. The LAPD is a modern, large plasma device constructed by Walter Gekelman (the director) and his staff of research scientists and technicians. The first plasma was achieved in July 2001 and the machine is now in operation.

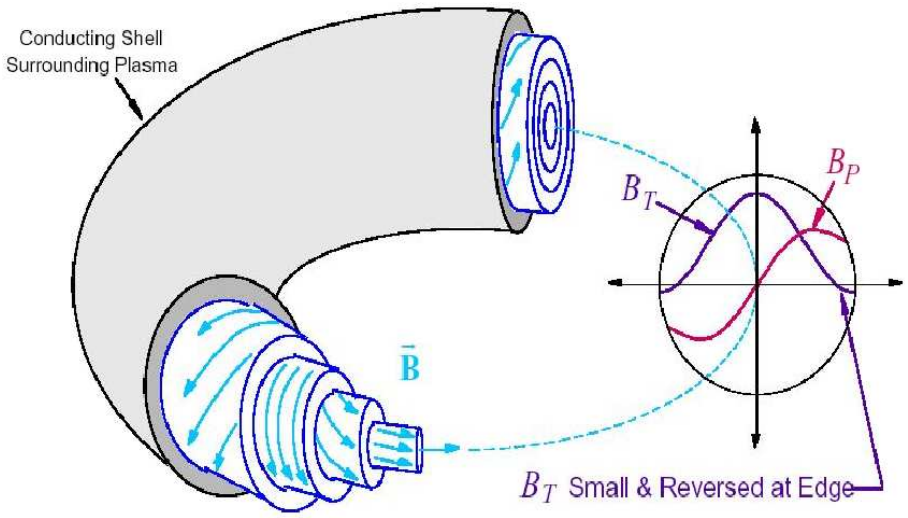

Figure 1.8: Representation of the total magnetic field in the RFP configuration. Toroidal (B_T) and poloidal (B_P) components of the magnetic field are of the same order, and B_T (see inset) changes sign near the conducting shell. The resultant magnetic surface is helicoidal. This is a solution of a *magnetostatic equilibrium* [14].

RFP device	aspect ratio
MST (USA)	$R_0/a = 2.88$
TPE–RX (J)	$R_0/a = 3.82$
RFX (EU)	$R_0/a = 4.35$
EXTRAP–T2R (EU)	$R_0/a = 6.89$

Table 1.1: Some RFP devices and corresponding aspect ratios.

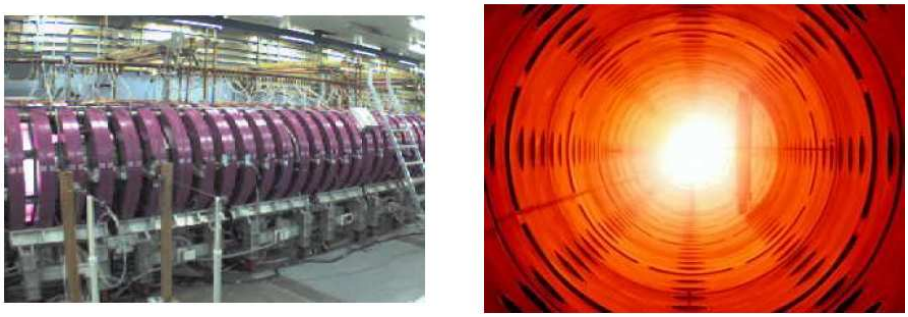

Figure 1.9: The LAPD device (left) and its internal camera (right).Typical plasma parameters are $n_e \sim 1 \times 10^{12} cm^{-3}$, $T_e \sim 5eV$, $T_i \sim 1eV$, and $B \lesssim 2kG$. The gases used in these experiments are helium and neon.

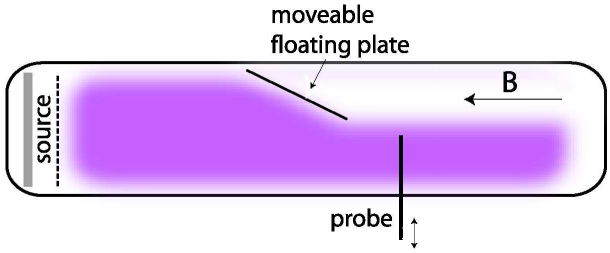

Figure 1.10: A schematic of the LAPD showing the experimental geometry. The cathode is the source of plasma that is injected in the vacuum chamber, where a strong magnetic field exists. A floating plate can be closed in order to produce a density gradient.

Figure 1.9 shows this device. This linear reactor is an $18 - m$–long, $1 - m$–diameter cylindrical vacuum chamber surrounded by 90 magnetic–field coils. The length of the LAPD plasma column can be changed by closing a hinged, electrically floating aluminum plate located 10 m from the cathode, as shown in Fig. 1.10. In experiments the plate is partially closed and used to limit the plasma column. When the plate is partially closed, there is no parallel to the magnetic field source of plasma for the region behind the plate and any observed plasma density must come from cross–field transport.

Chapter 2

Nonlinear Dynamics of Hall MHD Equations: Magnetosonic Fluctuations as Observed in Space Plasmas

Small–scale fluctuations have been commonly observed in a variety of space plasmas [47,48], for example in the solar wind (SW) [13,49,50], in the Earth magnetopause (MP) [51, 52], in auroral regions [53, 54], in dense molecular clouds [55] and in accretion disks [56]. This kind of fluctuations are well described through Hall–Magnetohydrodynamics (HMHD) equations [57], in which the effect of *ion inertia* is taken into account. The model, derived from the two–fluid MHD description by neglecting the *electron inertia*, differs from the traditional Magnetohydrodynamics (MHD) equations for the introduction of a new characteristic length: $\lambda_i = c/\omega_{pi}$ (c is the speed of light and ω_{pi} the ion plasma frequency), namely the *ion skin depth* (or *ion inertial length*).

Among other, an interesting physical application of HMHD model might be the magnetopause boundary layer (MPBL) where, for typical parameters, λ_i is a non–negligible fraction of the boundary layer thickness [28, 29]. The ion skin depth can range in the MPBL from $30km$ to $250km$ [39, 40, 58]. If Δ_{MP} represents the width of the inhomogeneous zone, typically one has: $\Delta_{MP}/\lambda_i \simeq 2 \div 20$ [28,40]. This is one of the best cases in which the inclusion of the Hall term in Ohm's law is a must. In this case one can write the Ohm's

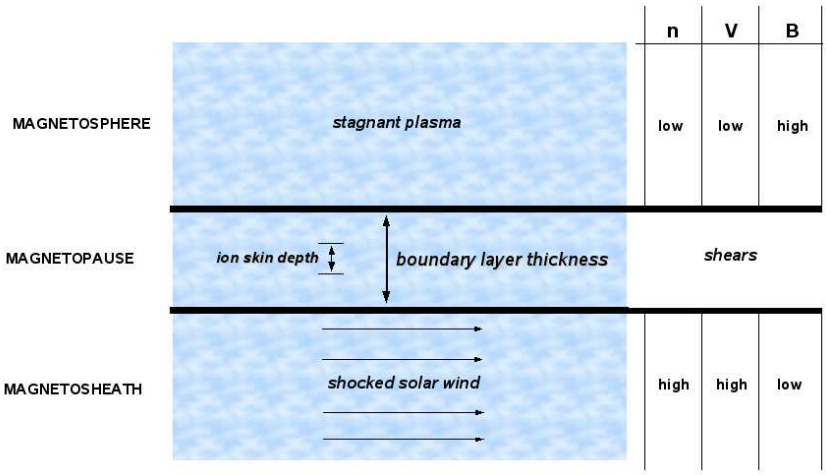

Figure 2.1: A sketch of the magnetopause boundary layer (MPBL) in the dusk flank. In the magnetosheath (MSH) the shocked and thermalized solar wind (SW) flows, adjacent to the MPBL, with supersonic and super–Alvénic speed. In the magnetosphere (MSP), the region dominated by strong magnetic field and low density, the plasma is more or less stagnant.

law as:

$$\mathbf{E} = -\mathbf{V} \times \mathbf{B} + \frac{1}{n\,e}\mathbf{J} \times \mathbf{B} \tag{2.1}$$

where, as usual, $\mathbf{E}$ is the electric field, $\mathbf{J}$ is the current density field, $\mathbf{V}$ is the ion bulk velocity, $\mathbf{B}$ the magnetic field and n the plasma density. The Hall correction is represented by the second term in the right–hand side of Eq. (2.1). A direct consequence of the introduction of this term is that the magnetic flux is no longer frozen into the ions, but in the electron fluid, which moves with the velocity $\mathbf{V}_e = \mathbf{V} - \mathbf{J}/(n\,e)$. By neglecting the term $\mathbf{J} \times \mathbf{B}$ in Eq. (2.1), one neglects an important nonlinear coupling between density, velocity and magnetic field [59]. Therefore, this term plays a very important role in describing small–scales of highly turbulent plasmas. It gives rise to interesting plasma phenomena as filamentations [60–62], an increase of the magnetic reconnection rate [63–67], relaxation processes [68–70] and accelerated dynamo action [71, 72].

At the MPBL the Cluster satellite reveals the existence of large–amplitude fluctuations of density and magnetic field [39, 40]. These structures were detected in the MSH, after the bow shock going from the Sun toward the

Earth, under conditions of low–magnetized plasma ($\beta \simeq 8 \div 10$). Data shows increases of magnetic field and plasma density 2–5 times the ambient values, or local decreases (holes) by 50–80 %.
These structures were detected also at the *dusk flank* of the MSP, where $\beta \simeq 0.3$. In Fig. 2.1 a typical configuration of the dusk flank is sketched. The satellite reveals the presence of high magnetic field fluctuations (up to 85%), accompanied with enhancements of the plasma density, that were propagating from MP to magnetosphere. In this region magnetic fluctuations are lower and these structures are more rare to observe, in fact, with respect to magnetosheath observations, they looks like *solitary* events. Some authors [39,40] identified these objects as *solitons* that propagate slowly with respect to the Alfvén speed and have perpendicular size of the order of few λ_i. Stasiewicz *et al.* [40] provided a theoretical description of these observations by using a linearized HMHD model [39, 73, 74].
In this Chapter we use direct numerical simulations to investigate the importance of Hall effect on the nonlinear dynamics of the MPBL. The nonlinear dynamics of a compressible Hall Magnetohydrodynamic plasma is investigated in a $2 + \frac{1}{2}D$ geometric configuration[1]. Two main features occur at small–scales where the Hall effect dominates, namely: i) an increase of the compressibility of the system and the breakdown of the strong link between velocity and magnetic field typical of usual MHD; ii) the excitation of small–scale fluctuations characterized by an anti–correlation between density and magnetic field intensity. These features evidence the excitation of a quasi–perpendicular magnetosonic turbulence that can be interpreted as the small scale signature of the break down of the nonlinear energy cascade due to Hall effect. Finally, we perform comparison between our model's results and Cluster's data, which turn out to be in very good agreement.

2.1 Kelvin–Helmholtz Instability at the MP

In the MPBL, due to the presence of a strong velocity shear (see data in Fig. 1.4 and the cartoon in Fig. 2.1), a large scale *Kelvin–Helmholtz Instability* (KHI) [16, 17, 75–77] may develop[2]. Observations have shown signatures

[1] Is a configuration in which all quantities depend only on two coordinates but vector fields still retain three components.

[2] The KHI can occur when velocity shear is present within a continuous fluid or when there is sufficient velocity difference across the interface between two fluids. The theory

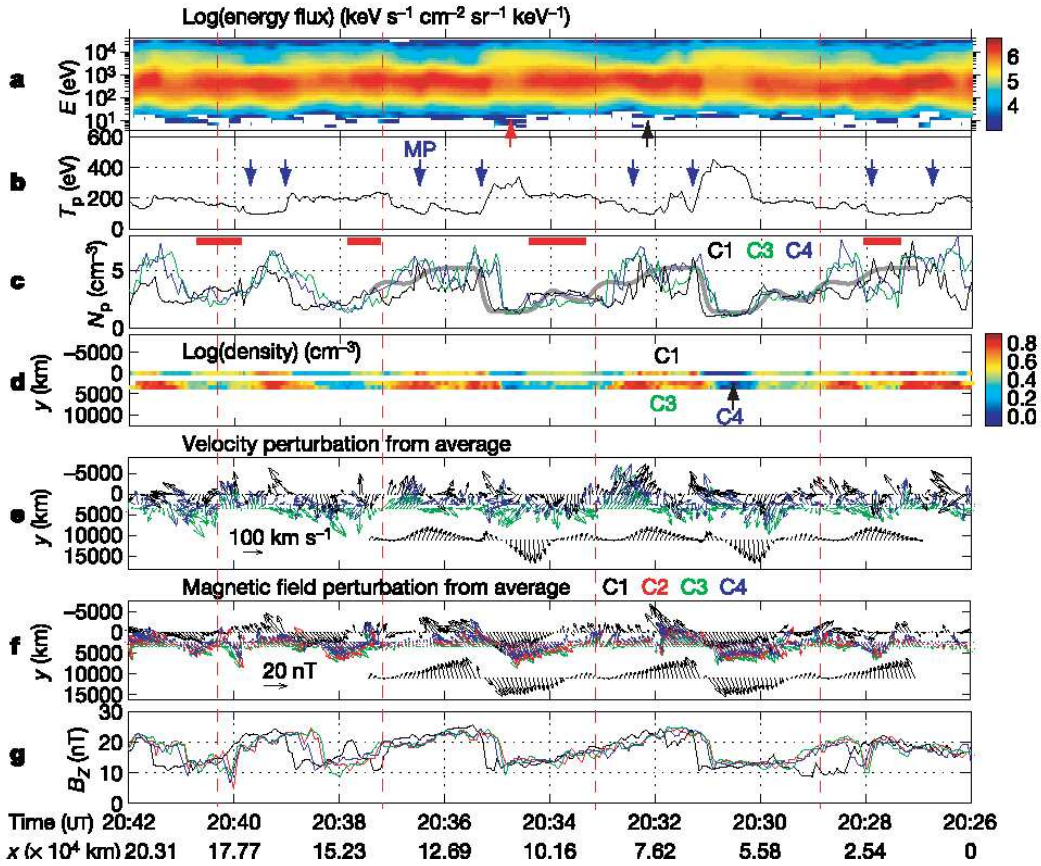

Figure 2.2: Detection by Cluster of rolled–up plasma vortices on November, 20th 2001 (20:26–20:42 UT) [34]. Time progresses to the left, and is translated into the position of the spacecraft as follows. In Earth's rest frame, the spacecraft motion is neglected as compared to that of the vortices. $-x$ is in the direction of the vortex motion in the spacecraft frame. The vortex velocity, $\mathbf{V}_{mean}$, is computed by averaging over the above interval the ion bulk velocity vectors measured by C1, C3 and C4 (see Chapter 1). y is orthogonal to both x and the direction of the averaged magnetic field, $\mathbf{B}_{mean}$, and points outward along the MP normal. Panel **a**, omni–directional energy spectrogram of ions observed by the Cluster 1 spacecraft (C1); panel **b**, ion temperature obtained by C1. The blue arrows mark approximate locations of the MP; panel **c**, plasma density variations. Red bars indicate instances when C1 observed higher density than C3 and C4; panel **d**, plasma density color–coded, projected along the spacecraft trajectories; panels **e**, **f**, x–y projection of the velocity and magnetic field deviations from $\mathbf{V}_{mean}$ and $\mathbf{B}_{mean}$, respectively (C1, black; C2, red; C3, green; and C4, blue). The red dashed vertical lines mark the approximate center of the vortex; panel **g**, z component of the measured magnetic field.

of this instability quite often in the MP [34, 78]. Typical length scales of the KHI are very large, that is around $10R_E$ (R_E being the Earth's radius). These scales correspond, based on the Taylor hypothesis, to frequencies less than $0.01Hz$. As in usual fluid flows, a nonlinear evolution of the instability drives a turbulent energy cascade towards small–scales, and a consequent formation of a turbulent spectrum. The KHI may occur along the flanks of the MSP, where the shocked SW is flowing fast relative to the stagnant magnetospheric plasma. Multiple and quasi–periodic encounters by spacecraft with the MP and vortex–like flow perturbations near the MP have been observed, and are often interpreted as surface waves or vortices excited by the KHI. Consequently, the KH vortices evolve only along the low–latitude MP and only low–latitude portions of the magnetospheric and solar–wind field lines are entrained into the vortices, inducing characteristic field perturbations in regions off the equatorial plane where the Cluster spacecraft were located. The profile of density, velocity and magnetic field, observed when a satellite passes through the center of the KH vortices in a direction parallel to the MPBL, is a multiple and quasi–periodic signal, as reported in Fig. 2.2 [34].

2.2 Observations of magnetosonic structures in space plasmas

The Cluster spacecraft detected several slow–mode magnetosonic structures that were traveling across MPBL. These structures, characterized by a strong anti–correlation between density and magnetic field, resemble slow mode that are a linear solution of the MHD theory [14, 41]. They were identified by some authors [39, 40] as *solitons*, *i. e.* solitary structures that travel in a background medium, in a persistent way, preserving their shape. Solitons are fluctuations that develop via an equilibrium between nonlinearities and dispersive effects [79, 80]. Because the multi–point capabilities of Cluster make it possible to determine the velocity of the structures, these authors estimate their propagation angles and velocities. In the MSH there is a large number of the above structures associated to both weaker and stronger magnetic field intensities [81]. Moreover, during the bow shock and MSH crossing of 3

can be used to predict the onset of instability and transition to turbulent flow in fluids of different densities moving at various speeds. Helmholtz studied the dynamics of two fluids of different densities when a small disturbance such as a wave is introduced at the boundary connecting the fluids.

	Observation 1	Observation 2
(magnetic field) B_0	40 nT	20 nT
(density) n_0	1 cm^{-3}	40 cm^{-3}
(Alfvén velocity) V_A	800 km/s	60 km/s
(ion skin depth) λ_i	200 km	40 km
(electron skin depth) λ_e	5 km	1 km
(pressures ratio) β	0.25	10
satellite position	$(-4, 17, 5)R_E$	$(10, 3.8, -7.6)R_E$

Table 2.1: Typical plasma parameters near the MPBL. The first column is related to Cluster observation of Ref. [39], in the dusk flank of the magnetosphere. In the second column (Observation 2) plasma parameters of the post–bow shock in the magnetosheath [40] are reported. The position of satellite is expressed in the GSE system (see note 3).

February 2002, Cluster spacecraft observed other very interesting stochastic fluctuations, with an anti–correlation between density and magnetic field. During this event the four Cluster satellites, separated at a distance of 200 km, were traveling at low speed ($\sim 2km/s$) towards the Earth. They passed through the foreshock and entered the main shock region at a radial distance of $13.5R_E$. The Cluster satellites encountered during this passage hundreds of large amplitude fluctuations [82]. Fig. 2.3 shows an example of a turbulent signal measured by Cluster in the MSH. The observed plasma parameters during this event are reported in Tab. 2.1 (Observation 2). The data analysis shows that the velocities of the structures in the plasma frame are not negligible (of the order of $0.1 \div 0.3V_A$) and have directions quasi–perpendicular to $\mathbf{B}$ (with an angle $\alpha \simeq 90^o$ with respect to $\mathbf{B}$). Determination of the velocity of the structure from the time difference of measurements on the four spacecrafts gives $\mathbf{V} = (-40, -110, 0)$ km/s in the GSE system[3]. This means that perturbations move with respect to the plasma at velocity about $10 \div 20$ km/s. The propagation direction with respect to the magnetic field is found to be $\alpha \simeq 84^o \pm 3^o$.
These fluctuations were detected by the Cluster spacecraft also at the dusk

[3]The Geocentric Solar Ecliptic System (GSE) has its X–axis pointing from the Earth towards the sun and its Y–axis is chosen to be in the ecliptic plane pointing towards dusk (thus opposing planetary motion). Its Z–axis is parallel to the ecliptic pole.

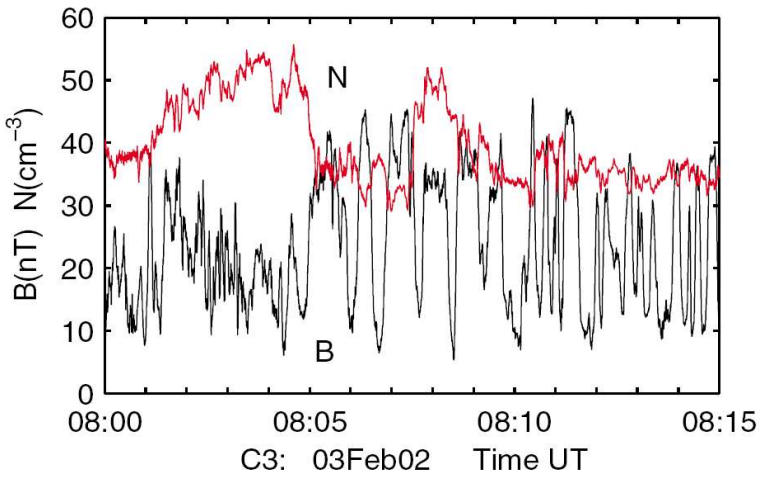

Figure 2.3: Cluster measurements of large amplitude magnetosonic structures in the MSH, shown with total magnetic field (black) and plasma density (red).

flank of the MSP. They look like a pressure balance between strong magnetic field depressions (up to 85 %) and enhancement of the plasma density and temperature [80]. On November–$25th$, 2001, the satellites were moving near the MP, in the magnetospheric region. The ambient plasma parameters are described in Tab. 2.1 (Observation 1). In this period the satellites reveal the presence of strong perturbations in the magnetic field which propagate with a speed of about $\sim 250km/s$ over slowly moving satellites ($1.3km/s$). The depression of magnetic field was -85% B_0, and propagate along a quasi–perpendicular direction with respect to B_0. In Fig. 2.4 a moving structures, seen by two spacecraft ($C2$,$C4$[4]) with a relative time delay of $6s$ which corresponds to a velocity $250km/s$ (deduced from the known separation between satellites) is shown [80]. The structure have a size of few ion inertial lengths. Structures are observed inward from the MP with tail–ward boundary layer flows (negative in the x–GSE direction). The adjacent flow in the MSH is much higher and reaches $800km/s$. This fluctuation in the magnetic field is accompanied by an increase of the plasma pressure through both the temperature and the number density derived from the satellite potential. The plasma density is represented in Fig. 2.5. From projections of the velocity vectors onto the inter–spacecraft position vector, one can estimate the struc-

[4]Labels $C1$, $C2$, $C3$ and $C4$ corresponds to 4 Cluster satellites.

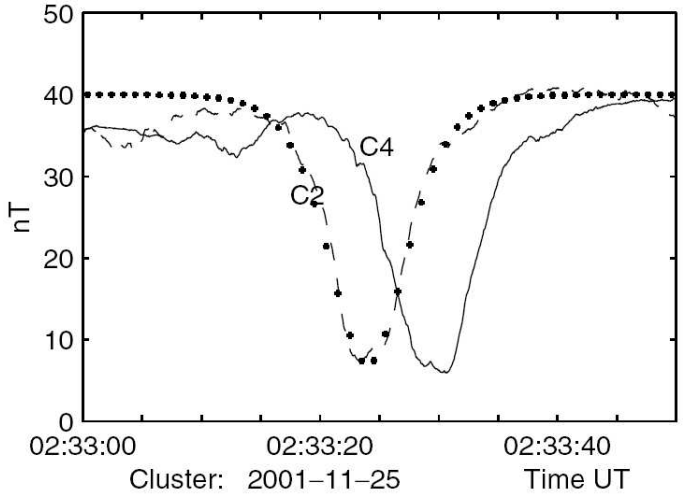

Figure 2.4: A magnetic depression observed by Cluster spacecraft C2 (dashed line) and C4 (solid line) in the total magnetic field. The structure moves with velocity $u_0 \simeq 250 km/s$ and has a width of $\sim 10\lambda_i$. The position of Cluster satellites was $(-4, 17, 5)$ R_E in the GSE coordinate system.

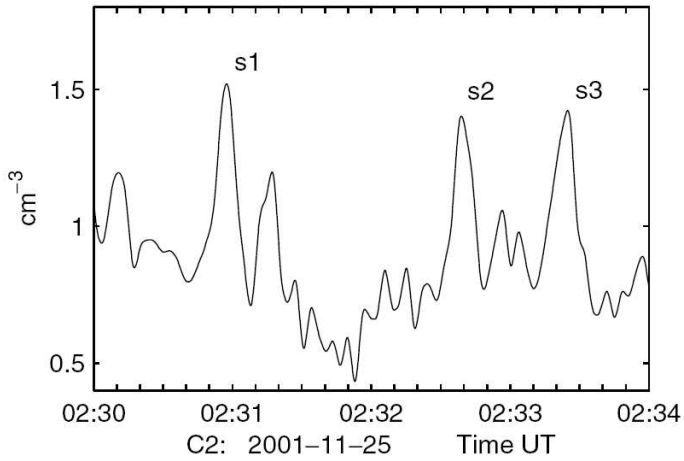

Figure 2.5: Density enhancements (s1, s2, s3) that correspond to three deep magnetic holes similar to that in Fig. 2.4. Peak labeled $s3$ corresponds to C2 in Fig. 2.4.

ture's speed relative to the medium as $80km/s$, that is a small ratio of the local Alfvén speed, and therefore could correspond, in the linear approximation of MHD theory, to the slow magnetosonic mode [14, 17, 20].
Stasiewicz *et al.* conjectured these observations in the frame of nonlinear waves and solitons in collisionless plasmas [82–84]. They took into account two–fluid equations of magnetohydrodynamics (Hall MHD). Natural wave modes at frequencies below the ion gyrofrequency are the Alfvén wave and two magnetosonic modes (slow and fast) [57]. For propagation at sufficiently large angles to a uniform magnetic field, it was shown using reductive perturbation theory that nonlinear dispersive fast and slow MHD waves obey to a Schrödinger–like equations. In this case the dispersion of magnetosonic waves comes from the ion perpendicular inertia caused by the finite frequency effect (the Hall effect in the generalized MHD description), while nonlinearities arise due to the ion advection and divergence of the nonlinear ion flux, as well as from the nonlinear Lorentz forces acting on the electron and ion fluids. Following this interpretation, for quasi–parallel propagation the dynamics of modulated Alfvén wave packets is governed by the DNLS[5] model. It is well known that, when the Hall effect is taken into account, the two basic MHD propagation modes (slow and fast) are modified and a third mode can propagate [14, 41, 86], namely the slow mode. The finite frequency effects are not included in ideal MHD: to take them into account, the ion inertia terms must be added in the Ohm's law, thus modifying MHD into Hall–MHD. Of course using such a model, the calculations are less complicated than in a fully kinetic model but not all physical effects are included in the model: spatial effects related to the ion Larmor radius ask for a different treatment to be accounted for [87]. Nevertheless, the Hall–MHD model is expected to provide a good description of the problem, as long as we don't consider frequencies too close to the multiples of the gyrofrequency.
In addition, when studying MP dynamics, other effects are to be taken into account simultaneously to get reliable results (as shown in Fig. 1.4): the magnetopause density gradient, the temperature effects, the magnetic field inhomogeneity, and the velocity shear must be introduced while remaining in the framework of ideal MHD.

[5]The Derivative NonLinear Schrödinger equation (DNLS) was proposed to describe nonlinear Alfvén waves in plasma [84, 85]

2.3 The compressible Hall Magnetohydrodynamics

From a theoretical point view, ideal MHD gives a description of the SW/MSP interaction that is in qualitative agreement with the observations. At the MP, the $\beta \simeq 1$ and therefore both a cold plasma approximation and the assumption of incompressibility are not fully satisfied. A third assumption has to be taken off, it is the assumption that the frequency is negligible with respect to the proton gyrofrequency ω_{pi}. Since the spectrum of the fluctuations extends up to the lower hybrid frequency [88], it is necessary to include finite frequency effects in the model and this can be done by introducing the effect of ion inertial length in MHD equations [89–92].
By combining the density of ions and electrons, fluid equations, whose variables are the *total* mass density, center–of–mass velocity and magnetic field, can be obtained. By using these assumptions one can obtain the following set of equations:

$$\frac{\partial N}{\partial t} + \nabla \cdot (N\ \mathbf{V}) = 0 \tag{2.2}$$

$$N\ m_i \left[\frac{\partial \mathbf{V}}{\partial t} + (\mathbf{V}\cdot\nabla)\mathbf{V}\right] = \mathbf{J}\times\mathbf{B} - \nabla\cdot\mathbb{P}_{tot} \tag{2.3}$$

where N is the density, $\mathbf{V}$ the ion bulk velocity, $\mathbf{B}$ the magnetic field, and $\mathbb{P}_{tot}$ the kinetic pressure tensor. Moreover the Maxwell equation for the magnetic field is needed:

$$\frac{\partial \mathbf{B}}{\partial t} = -\nabla\times\mathbf{E} \tag{2.4}$$

where

$$\mathbf{E} = -\mathbf{V}\times\mathbf{B} + \frac{1}{N\ e}\left[\mathbf{J}\times\mathbf{B} - \nabla P_e\right] \tag{2.5}$$

is the Ohm's law for the electric field. $\mathbf{J}$ is the current and P_e the electron pressure. By using Eq. (2.4) and Eq. (2.5), the following *induction equation* is obtained:

$$\frac{\partial \mathbf{B}}{\partial t} = \nabla\times\left[\mathbf{V}\times\mathbf{B} - \frac{1}{N\ e}\mathbf{J}\times\mathbf{B} + \frac{1}{N\ e}\nabla P_e\right] \tag{2.6}$$

The "$\mathbf{J}\times\mathbf{B}$" is the *Hall correction*, and the term ∇P_e is the *first Larmor radius correction*. By the way, as we shall discuss later, if one uses an adiabatic closure for the pressure, this last term doesn't give any dynamical

information on the system. Equations (2.2), (2.3) and (2.6) are the full set of the HMHD equations. Together with remaining Maxwell laws, the Ohm's law, and an equation of state, they can be used to describe the dynamics of a plasma in the two–fluid MHD approximation.
The role of the $\mathbf{J} \times \mathbf{B}$–term is fundamental since its presence means that there is a coupling between magnetic field, current, and density. In addition there is no scalar relationship between $\mathbf{J}$ and $\mathbf{E}$; there must be a component of $\mathbf{E}$ which is perpendicular to $\mathbf{J}$ and $\mathbf{B}$ to balance the $\mathbf{J} \times \mathbf{B}$ term. This is the "Hall effect". A simple way to investigate the relevance of the Hall effect is to compare the $\mathbf{J} \times \mathbf{B}$ and the $\mathbf{V} \times \mathbf{B}$ term:

$$\frac{|\mathbf{J} \times \mathbf{B}|}{|N\ e\mathbf{V} \times \mathbf{B}|} \sim \left(\frac{\lambda_i}{L_0}\right)\left(\frac{c_s}{V_0}\right)\left(\frac{T_e}{T_i}\right)^{1/2} \tag{2.7}$$

where $c_s = (K_B T_e/m_i)^{1/2}$ is the ion acoustic speed, $T_{i(e)}$ the ion (electron) temperature, L_0 a typical length of the system, V_0 is a typical velocity. Since we assume $T_e \sim T_i$, we see that in order to neglect the $\mathbf{J} \times \mathbf{B}$ term we must require $(\lambda_i/L_0) << (V_0/c_s)$.

2.3.1 Hall MHD equations in a dimensionless form

Eqs. (2.2), (2.3) and (2.6) can be written in a dimensionless form by introducing the following relation involving a typical plasma density N_0, the large scale L_0 of the system, the Alfvén speed V_A related to the mean magnetic field B_0, the Alfvén traveling time $\tau_A = L_0/V_A$ and a typical mean pressure P_0:

$$\begin{aligned}
N &= N_0\ n \\
L &= L_0 l \\
\mathbf{V} &= V_A\ \mathbf{v} \\
t &= \tau_A \hat{t} \\
\mathbf{B} &= \mathbf{B}_0\ b \\
P_i &= P_0\ p_i \\
P_e &= P_{e0}\ p_e \\
\mathbf{E} = E_0\ \mathbf{e} &= V_A\ B_0 \mathbf{e} \\
\mathbf{J} = J_0\ \mathbf{j} &= \frac{B_0}{\mu_0 L_0}\mathbf{j}
\end{aligned} \tag{2.8}$$

symbol	definition	name
V_A	$B_0/\sqrt{\mu_0\ N_0\ m_i}$	Alfvén velocity
λ_i	c/ω_{pi}	ion inertial length
β	$2\mu_0 P_0/B_0^2$	plasma beta
β_e	$2\mu_0 P_{e0}/B_0^2$	electron beta
r_i	$\lambda_i\ \sqrt{\beta}$	ion larmor radius
M_A	V_0/V_A	Alfvénic Mach number
c_s	$\sqrt{\frac{\partial P}{\partial \rho}}$	sound speed

Table 2.2: Some plasma parameters

where n, l, v, $\hat{t}$, b, p_i, p_e, e and j are dimensionless quantities. In our numerical simulations we use the whole set of compressible Hall MHD equations by using expression (2.1) for the electric field. Assuming an adiabatic closure for electrons, the term ∇p_e does not give contribute to the equation. In fact, choosing for the electron pressure $p_e = p = n^\gamma$ and neglecting constants, it follows:

$$\frac{1}{n}\nabla(n^\gamma) = \frac{\gamma}{\gamma-1}\nabla\left(n^{\gamma-1}\right)$$

Now, evaluating $\nabla \times \mathbf{E}$ for the evolution of the magnetic field, the electron pressure contribution is vanishing:

$$\nabla \times \mathbf{E}_{P_e} = \nabla \times \nabla\left\{\frac{\gamma}{\gamma-1}\nabla\left(n^{\gamma-1}\right)\right\} = 0$$

By using plasma parameters in Table 2.2 and (2.8), Eqs. (2.2), (2.3) and (2.6) read:

$$\frac{\partial n}{\partial t} = -(\mathbf{v}\cdot\nabla)n - n(\nabla\cdot\mathbf{v}) \tag{2.9}$$

$$\frac{\partial \mathbf{v}}{\partial t} = -(\mathbf{v}\cdot\nabla)\mathbf{v} + \frac{1}{n}\left[(\nabla\times\mathbf{b})\times\mathbf{b} - \frac{\beta_0}{2}\,\nabla\cdot\mathbb{P}\right] + \nabla\cdot\sigma \tag{2.10}$$

$$\frac{\partial \mathbf{b}}{\partial t} = \nabla\times\left[\mathbf{v}\times\mathbf{b} - \frac{\lambda_i}{L_0 n}(\nabla\times\mathbf{b})\times\mathbf{b} - \frac{1}{S_\mu}\nabla\times\mathbf{b}\right] \tag{2.11}$$

Moreover, to close the set of equations, we assume

$$P_{ij} = n^\gamma \delta_{ij} \tag{2.12}$$

The elements of the viscous stress tensor σ in the Eq. (2.10) are

$$\sigma_{i\,j} = \frac{1}{S_\nu}\left[\left(\frac{\partial v_i}{\partial x_j} + \frac{\partial v_j}{\partial x_i}\right) - \frac{2}{3}\frac{\partial v_k}{\partial x_k}\right] \tag{2.13}$$

where $S_\nu = L_0 V_A/\nu$ (ν being the plasma diffusivity) is the *Reynolds number* [12]. Of course, magnetic field must be divergenceless:

$$\nabla \cdot \mathbf{b} = 0 \tag{2.14}$$

The quantity $S_\mu = (4\pi L_0 V_A)/(c^2\eta)$ (η being the plasma resistivity) appearing in Eq. (2.11) is the *Lundquist number*, namely the analogous of the Reynolds number for the magnetic field–lines diffusion [14]. As clearly visible from Eq. (2.11), the Hall term consists of second–order derivatives multiplied by a small coefficient (λ_i/L_0). The actual value of the dimensionless numbers S_ν and S_μ are large in typical astrophysical situations ($10^6 \div 10^{12}$). Therefore, the actual meaning of the coefficients S_ν and S_μ, as we will discuss in the following section, is to represent an artificial viscosity that ensure the numerical stability of the code.

2.4 The numerical simulation

We integrate Eqs. (2.9)–(2.11) in a cartesian box, as shown in Fig. 2.6. We study a sheet of plasma on the equatorial plane of the Earth, located at the flank boundary of the MP, where the solar magnetic field, carried by the SW, and the magnetic field of the Earth mix together. This region is highly inhomogeneous, as shown in Fig. 1.4, since the magnetic fields of the Earth and SW have different intensities and directions. On the other hand, also the density and the velocity field turn out to be inhomogeneous. Because the two fluids are in different thermodynamic conditions, the density will change by going from inside the magnetosphere to the solar wind. Moreover, since the velocity of the solar wind is much higher than the plasma velocity inside the magnetosphere, also the velocity field will be sheared in the boundary layer zone, like the situation sketched in Fig. 2.1.
Basically, we want to describe the dusk flank of the MP. We work in a $2+\frac{1}{2}D$ cartesian geometry configuration: vector quantities are represented by three cartesian components, but only variations along two independent directions (x and y) are allowed, namely all quantities are considered as constant along

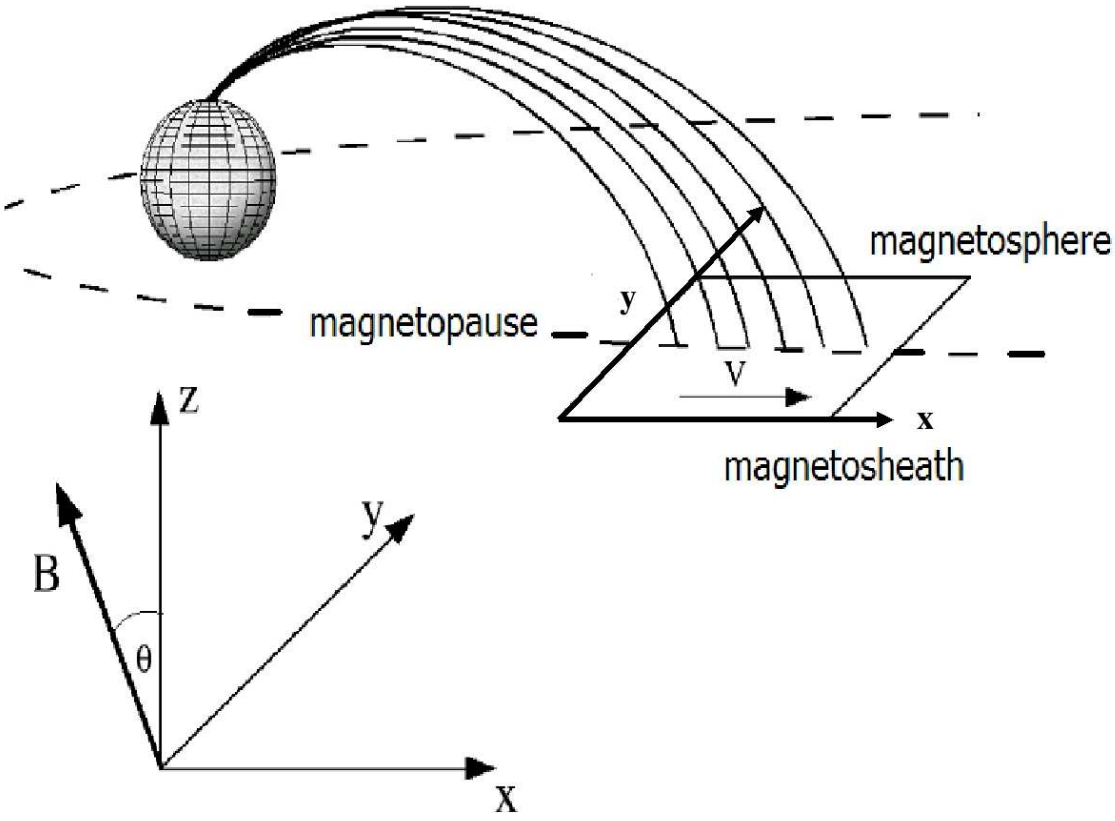

Figure 2.6: In the upper figure is represented the MP flank along with the geometrical configuration of the simulation. Down is represented our reference frame with the magnetic field vector.

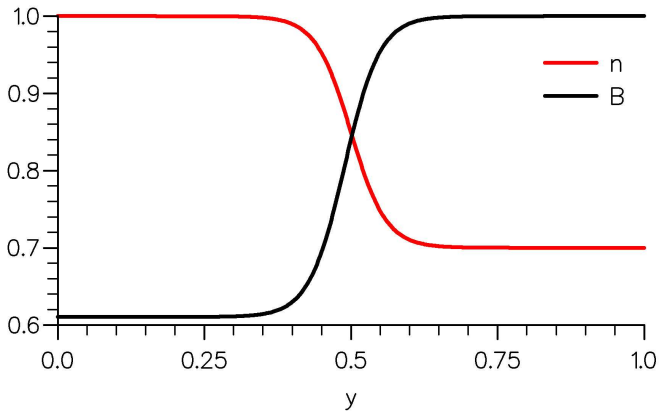

Figure 2.7: The density (red) and the magnetic field intensity (black) in the 1–D tgh–equilibrium.

z. In our model x and y axes have opposite directions with respect to the GSE system. The y direction is perpendicular to the MPBL. The magnetic field, due to the presence of the SW flow, is tilted by an angle θ with respect to the z–axis. Due to normalization (2.8), variables x, y ranges between 0 an 1.
In order to identify these entry processes it is first necessary to build a realistic equilibrium model of the MP, then to perturb this equilibrium in response to SW variations. The simplest equilibrium state of the MP is that of a one–dimensional tangential discontinuity of finite thickness, that qualitatively simulates spacecraft observations like that reported in Fig. 1.4. Hyperbolic tangents are the best choice to simulate a jump–like profile in a fluid–like formalism [93], so we will build a *tgh–equilibrium*. We use the following expressions for the equilibrium density $n_0(y)$ and velocity field $\mathbf{v}_0(y)$:

$$n(x, y, t = 0) = n_0(y) = \frac{1}{2}\left[1 + \alpha - (1 - \alpha) \cdot \tanh\left(\frac{y - 0.5}{\Delta}\right)\right] \tag{2.15}$$

$$\mathbf{v}(x, y, t = 0) = \mathbf{v}_0(y) = \frac{A_v}{2} \cdot \left[1 - \tanh\left(\frac{y - 0.5}{\Delta}\right)\right] \hat{\mathbf{u}}_x \tag{2.16}$$

where $\hat{\mathbf{u}}_x$ represents the unit vector along the x direction, Δ is the width of the inhomogeneous zone, α and A_V are parameters that determine the jumps

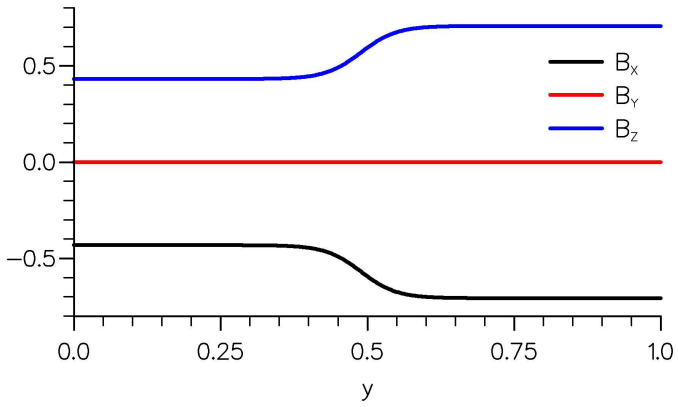

Figure 2.8: Magnetic field components in the 1–D tgh–equilibrium.

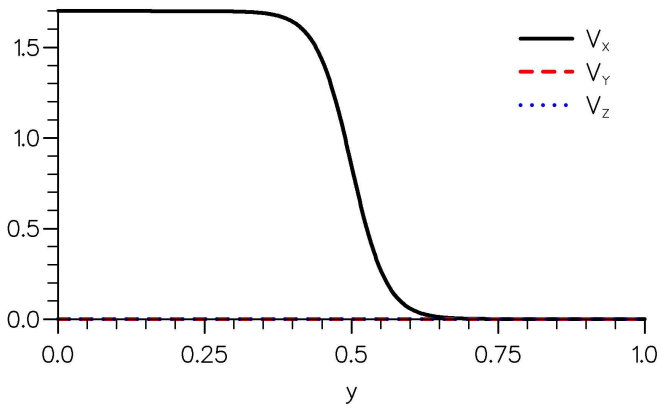

Figure 2.9: Velocity field components in the 1–D tgh–equilibrium

in the density and velocity profiles, respectively. Due to the adiabatic approximation, defining the density means also defining the kinetic pressure. In order to obtain an *ideal equilibrium*[6], we need to balance the inhomogeneous kinetic pressure with the magnetic pressure. Thus, we define the equilibrium magnetic field in the following way:

$$\mathbf{b}(x,y,t) = \mathbf{b}_0(y) = \sqrt{C_b - \beta n_0^\gamma(y)}\,(\cos\theta\hat{\mathbf{u}}_z - \sin\theta\hat{\mathbf{u}}_x) \tag{2.17}$$

where θ is the angle between magnetic field and z axis as seen in Fig. 2.6. C_b is an arbitrary constant that must be imposed at boundaries from the total pressure balance

$$C_b = \mathbf{b}_0^2(y_*) + \beta n_0^\gamma(y_*)$$

where y_* is the value of y at the boundary. The equilibrium profile of the density and magnetic field strength is reported in Fig. 2.7. As described by Eq. (2.17), the magnetic field has two components, and the component normal to the boundary layer is zero. Fig. 2.9 shows the velocity shears described by Eq. (2.16): only the x–component of $\mathbf{v}$ is non vanishing. The profile defined by Eqs. (2.15)–(2.17) is a stationary solution of Eqs. (2.9)–(2.11), when neglecting dissipative terms.
The equilibrium configuration specified above is forced, during the simulation, by averaging quantities along the periodic x direction. Then, the mean values are subtracted from the fields and replaced with expressions described by Eqs. (2.15)–(2.17). This procedure permits to retain constant in time the mean profile of n, $\mathbf{v}$ and $\mathbf{b}$. This procedure is equivalent to a large scale forcing. The aim of adding forcing terms to Eqs. (2.9)–(2.11) is to obtain a statistically stationary state, that is a balance between large–scale injection and the small–scale artificial dissipation.
We perturbed the equilibrium described by Eq. (2.15), (2.16) and (2.17) with the following superposition of fluctuations:

$$v_y(x,y,t=0) = A_{v_y} \sum_{m_x=1}^{3} \sin(2\pi m_x x + \psi_{m_x}) \tag{2.18}$$

where ψ_{m_x} are random phases, $A_{v_y} = 10^{-4}$ is the amplitude of the perturbation and m_x are wavenumbers in the periodic direction.

[6]This equilibrium is an exact solution of Hall MHD equations without dissipative terms.

2.4.1 The numerical technique

The code uses second order finite difference schemes to compute spatial derivatives. Since the final state of the evolution could be highly turbulent and shock waves will be probably present, one would need to use high viscosity and resistivity to ensure the numerical stability of the code. However, because of the presence of the Hall term in the equations, which acts as a dispersive filter on small–scale, we cannot use high values for the diffusivity, because the unrealistic diffusion, which allows the code to be numerically stable, would filter out the contribution of the Hall term in the spectrum. We reached a good compromise in such a matter through the use of upwind derivatives for the advection terms [94–96] and putting the dissipative terms on wavevectors which are at the limit of the *Nyquist frequency* in the spectra [97]. In fact, the upwind scheme alone would not help, since the Hall term cannot be put in hyperbolic form. Then we must avoid using *Godunov–like* [96, 98, 99] and *shock capturing* schemes [100][7]. Thus, we need anyway some dissipation to prevent numerical instabilities due to *whistler* waves [16, 57]. Precisely, we use forward or backward (upwind) differencing schemes [95], depending on the wave propagation. Moreover we still retain viscosities to act as a filter on high frequency waves that cannot be "captured" by the upwind scheme. This scheme is often used to integrate equations in which a centered finite difference scheme fails, as for example *Burgers equations* [95] in which shocks destabilize simulations. Moreover it can be shown that a non–centered scheme, in which derivative computing depends by the velocity of propagation, is very stable with respect to the *Courant* condition [94]. How the algorithm *chooses* points that must be used for spatial derivatives is sketched in Fig. 2.10. We use a second order Runge–Kutta scheme for time derivatives [97].
As usual with finite difference schemes, one needs some special technique in order to preserve a divergenceless magnetic field at each time step [102, 103]. We use a *projection–like* method [103]. The *Brackbill and Barnes* technique can be explained through five steps as follows:

[7] This kind of numerical techniques can only be applied to pure hyperbolic equations, in fact they need a *solver* (for further details see *Roe–type* solvers in the Ref. [101]) that compute the total flux for every finite volume to evaluate derivatives. Compressible Hall MHD equations are not purely hyperbolic, due to the presence of the dispersive term, so these schema are inadequate.

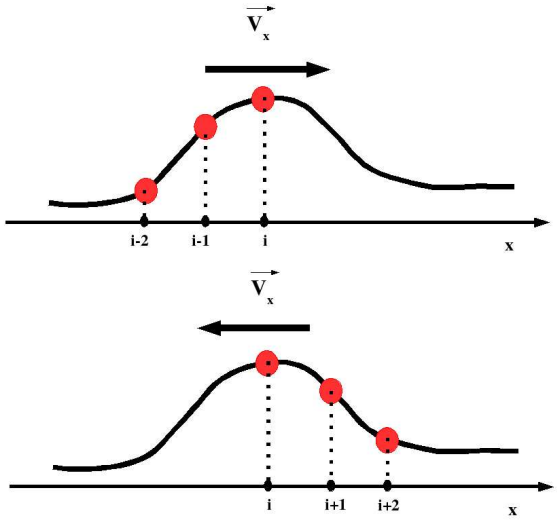

Figure 2.10: A representation of the up–wind technique for advection derivatives $[\mathbf{V}_x \cdot \partial_x de_x f(x_i)]$. Points used to evaluate the spatial derivative of a variable depend on the advection velocity, *i. e.* the algorithm uses points that *stay up* the wave.

0) Assume that $\mathbf{b}^* = \nabla \times \mathbf{A} + \nabla\phi$, where $\mathbf{A}$ is the vector potential and ϕ a scalar function.
1) Evaluate divergence–affected $\mathbf{b}^*$ by integrating Eqs. (2.9)–(2.11).
2) Evaluate the *error function* $\epsilon = \nabla \cdot \mathbf{b}^*$.
3) Invert the equation $\nabla^2\phi = \epsilon$ to obtain ϕ.
4) Obtain the divergenceless magnetic field $\mathbf{b}^{new}$ computing $\mathbf{b}^{new} = \mathbf{b}^* - \nabla\phi$.

Similar results can be obtained by adding an evolution equation for the divergence of the magnetic field containing dissipative terms which make the non–solenoidal part of the field to diffuse quickly in time [102, 103]. This ensures the divergenceless condition for the magnetic field at the same order of the numerical scheme. In this way one can add to Eqs. (2.9)–(2.11) the diffusion equation

$$\frac{\partial\phi}{\partial t} = \frac{1}{S_\phi}\nabla^2\phi - \nabla \cdot \mathbf{b} \tag{2.19}$$

and filter out divergence, in a similar way as described before. The parameter S_ϕ is an arbitrary viscous–like coefficient.
We use periodic boundary conditions along the x direction and zero–gradient

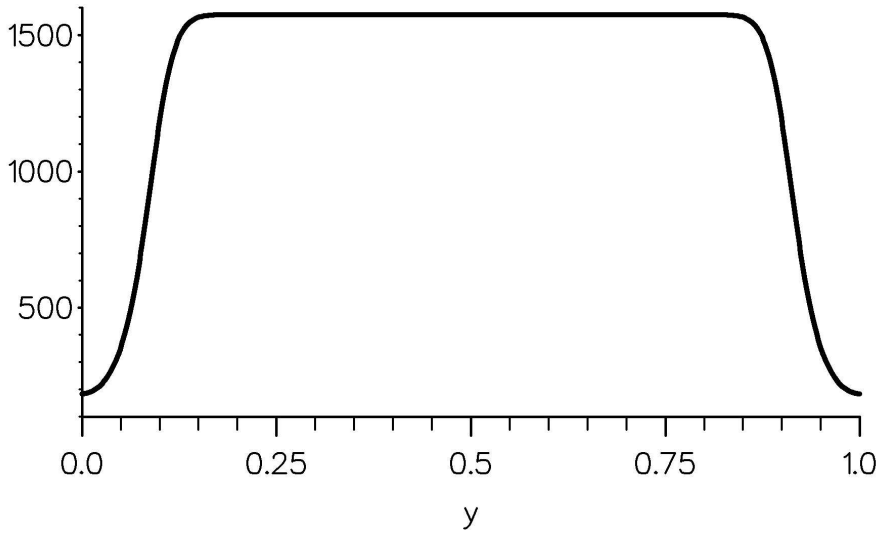

Figure 2.11: The y–profile of Reynolds number S_ν and Lundquist number S_μ. The expression is $S_\xi(y) = \left\{(\xi_b - \xi)\left[e^{-\frac{y^2}{2\sigma}} + e^{-\frac{(y-1)^2}{2\sigma}}\right] + \xi\right\}^{-1}$,with $\xi = \nu, \mu$. The parameter ξ_b is the viscosity (resistivity) at boundaries, and σ is the width of gaussians. We choose for this simulation $\sigma \simeq 8 \times 10^{-2}$, $\xi \simeq 6.3 \times 10^{-4}$ and $\xi_b \simeq 5.2 \times 10^{-3}$.

boundary conditions in the y direction ($\partial/\partial y = 0$) for all quantities, except for the y component of the magnetic field, which must to fulfill the divergenceless condition on the boundaries, as well. In this case, we first calculate the x component of the magnetic field, then the boundary condition for the y component is imposed from the relation (2.14). In addition we impose a decreasing Reynolds (Lundquist) number at the y boundaries to reduce numerical noises due to reflection or unrealistic boundary layers. The profile of S_ν and S_μ is a combination of gaussian functions, as shows Fig. 2.11.
The system of equations (2.9)–(2.11) is integrated on a numerical mesh of $N_x \times N_y = 512 \times 528$ gridpoints, N_x and N_y being the number of gridpoints along the x and y directions, respectively. The integration domain has extension: $[0,1] \times [0,1]$. The time step used in the simulation is $\Delta t = 1 \times 10^{-6}$. This value is very small due to the effects of whistler waves on the *CFL* condition that becomes $\Delta t \leq (N_{\lambda_i} \Delta x^2)/V_A$ [104]. All the runs are performed

using parallel computing with MPI directives[8]. We fixed, for the equilibrium described by Eqs. (2.15)–(2.17), in all simulations: $\Delta = 6 \times 10^{-2}$, $\alpha = 0.7$, $A_v = 1.7$, $\theta = \pi/4$ rad. The arbitrary constant C_b in the Eq. (2.17) is choosed in order to obtain the value of the magnetic field equal 1 at the boundary $y = 1$, that is $C_b \simeq 1.8$.
The plasma parameter $\beta(y) = 2\beta_0 n^\gamma(y)/B^2(y)$ represents the effective ratio between kinetic and magnetic pressure. Due to inhomogeneity of density and magnetic field, it changes along y directions. Free parameters β_0 and α are chosen in order that the plasma equilibrium parameter $\beta(y)$ varies in the range $[1.5 \div 7.5]$ across the y directions. This range overlaps, with good approximation, Cluster observations between the magnetosheath ($\beta = 4 \div 10$) and magnetosphere $\beta = 0.3 \div 1$ [16, 39, 40]. Moreover, in our simulations we use: $L_0/\lambda_i = 30$, namely the integral length scale is 30 times longer than the ion skip depth. This also means that Hall effect should dominate the behaviour of the plasma at length scales typically of order: $k_H^{-1} \sim L_0/\lambda_i$. The ratio between "our" MP thickness and λ_i is ~ 3. Of course the choice of parameters is based on a order of magnitude assessment, however we stress that MP parameters are highly variable both in time and space, so, a precise valuation is practically impossible.

2.5 Results of the simulations

2.5.1 The starting point of the energy cascade

The *tgh–equilibrium*, described by Eqs. (2.15)–(2.17), is unstable with respect to the KHI [105–107]. To observe the nonlinear evolution of the system we compute a Fast Fourier Transform (FFT) [97] along the periodic direction x, and then we integrate the spectrum in the inhomogeneous direction y. For a generic field f ($f = n,\ v,\ b$), the Fourier decomposition is

$$f(x, y, t) = \sum_{m_x} \hat{f}(m_x, y, t) e^{(2\pi m_x x + \phi_{m_x})} \tag{2.20}$$

[8] All these simulation are performed at the *High Performance Computing Center* of the *University of Calabria*, Cosenza (Italy), by using the 22–processors *Digital Alpha Server Galileo*.

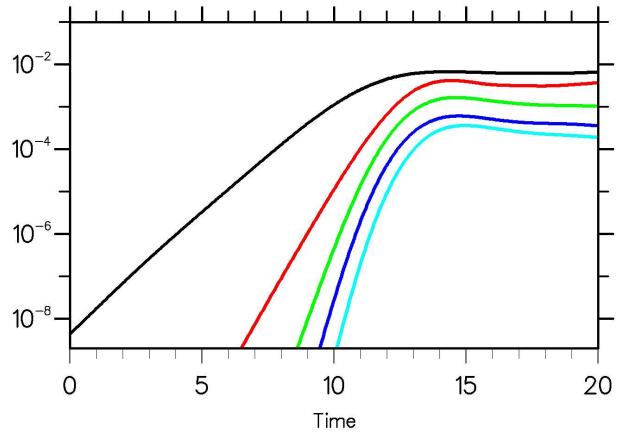

Figure 2.12: Total energy $E_n(m_x, t)$ as a function of time (normalized to Alfvén time τ_A), for $m_x = 1$ (black), 2 (red), 3 (green), 4 (blue), 5 (azure–blue).

Then we obtain the total energy associated to the field E_f as a function of the time t and of the wavenumber m_x:

$$E_f(m_x, t) = \int_0^1 |\hat{f}(m_x, y, t)|^2 dy \tag{2.21}$$

where $\hat{f}$ is the Fourier coefficient in Eq. (2.20). In Figs. 2.12–2.14 are shown respectively $E_n(m_x, t)$, $E_v(m_x, t)$ and $E_b(m_x, t)$ as a function of time, and for several wavenumbers. When the equilibrium is perturbed by the transverse fluctuations as in Eq. (2.18), we observe an exponential growth of the most unstable mode followed by the growth of modes with increasing wavevectors. This means that small–scale turbulent fluctuations are excited through a cascade process, and, after a time of the order of $t \simeq 10\tau_A$, the system reaches a turbulent statistically stationary state.
In the starting point of the cascade a large scale vortex is produced, as represented in Fig. 2.15. The KHI carries energy from large scale shears to small–scale, so large scale vortices drive the nonlinear cascade and, as represented in Figs. 2.12–2.14, secondary modes are then excited. The vortex is able to mix the two distinct regions, namely the one characterized by high values of β, and the region where $\beta \simeq 1$.

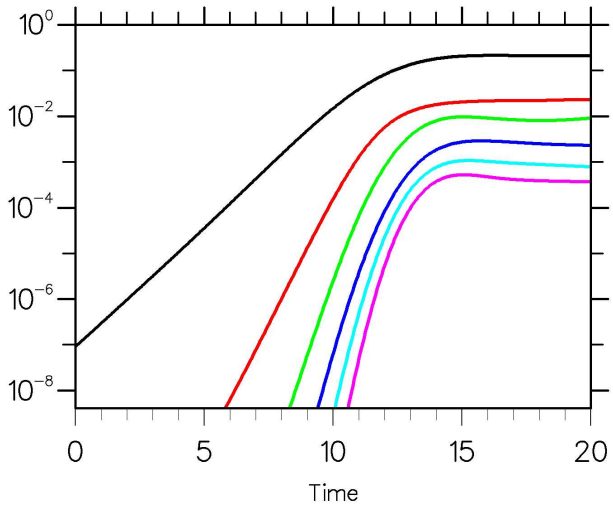

Figure 2.13: Total energy $E_b(m_x, t)$ as a function of time (normalized to Alfvén time τ_A), for $m_x = 1$ (black), 2 (red), 3 (green), 4 (blue), 5 (azure–blue), 6 (fuchsia)

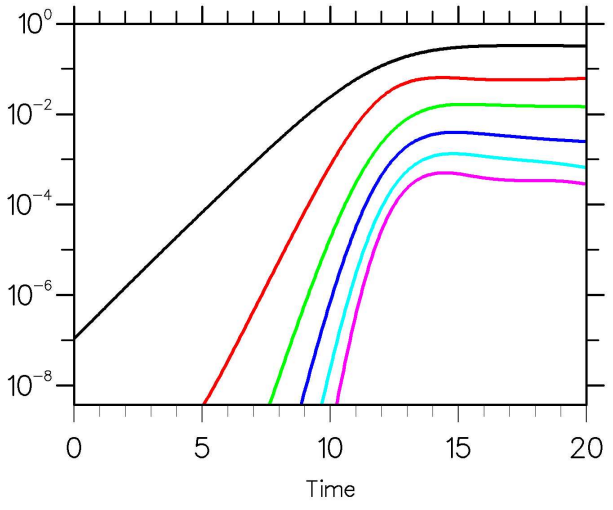

Figure 2.14: Total energy $E_v(m_x, t)$ as a function of time (normalized to Alfvén time τ_A), for $m_x = 1$ (black), 2 (red), 3 (green), 4 (blue), 5 (azure–blue), 6 (fuchsia)

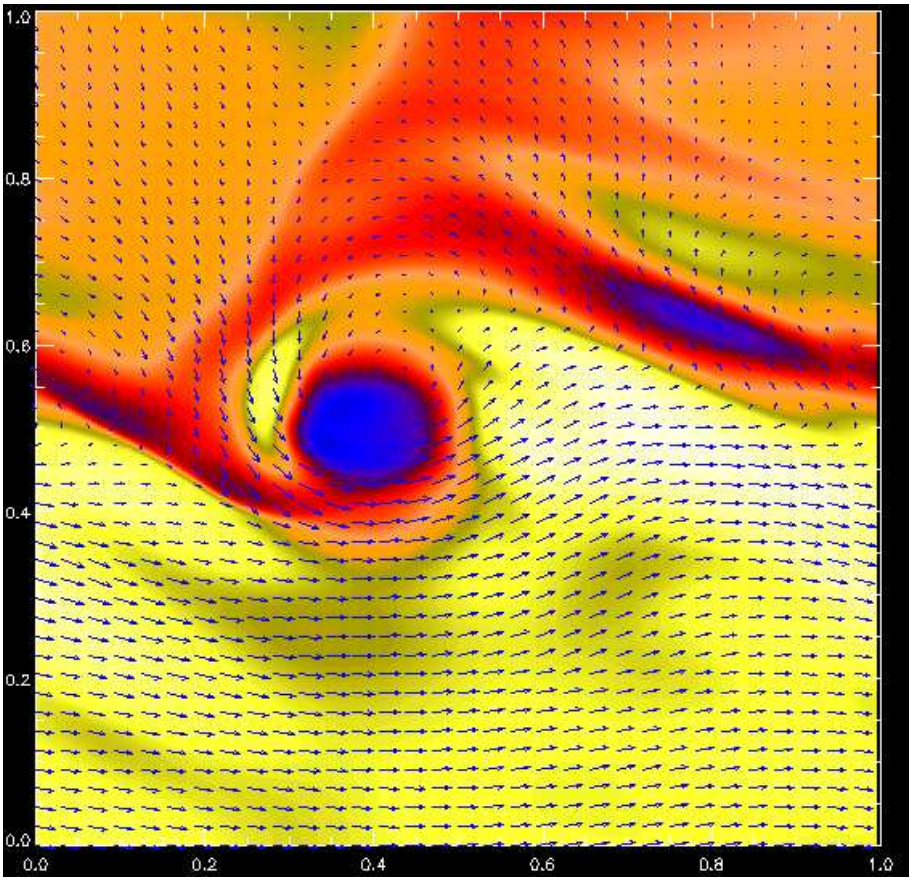

Figure 2.15: 2D–contour of a large scale in the density profile. Blue arrows represent the velocity field in the x–y plane.

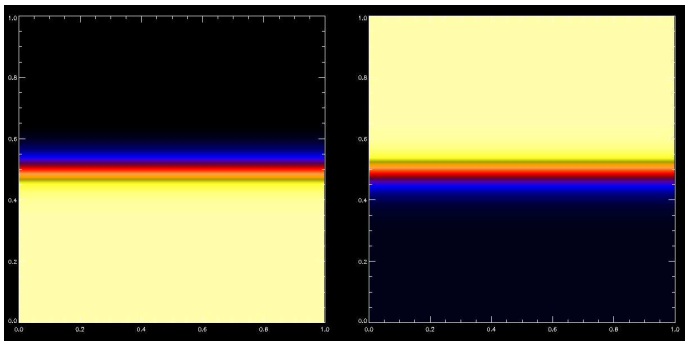

Figure 2.16: $2D$ contours of density (left) and magnetic field strength (right) at the initial time ($t = 0.0\ \tau_A$).

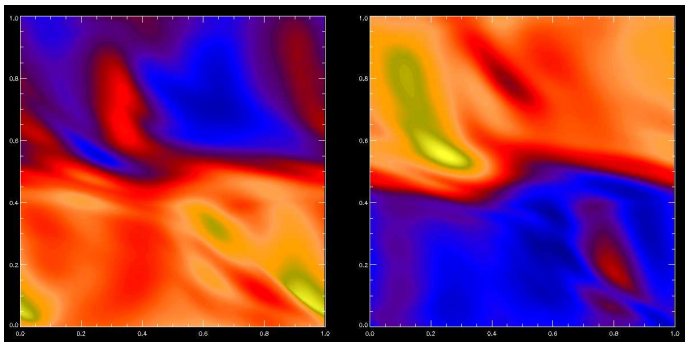

Figure 2.17: $2D$ contours of density (left) and magnetic field strength (right) at time $t = 7.0\tau_A$.

2.5.2 Fully developed magnetosonic turbulence

In Figs. 2.16–2.19, contour plots for the density $n(x, y, t)$ and the magnetic field intensity $b(x, y, t)$ are shown at different times, $t = 0, 7, 16, 19\ \tau_A$. When the saturation of instability occurs (see Fig. 2.20) the plots evidence two different regions: i) Region A (lower values of y), where the plasma $\beta(y)$ parameter is higher, characterized by the presence of an anti–correlation between n and b; ii) Region B (higher values of y), where the plasma $\beta(y)$ parameter is lower, characterized by the presence of strong gradients. In Fig. 2.20 differences between Region A and Region B are stressed.
In Fig. 2.21 we report fluctuations of both density and magnetic field with

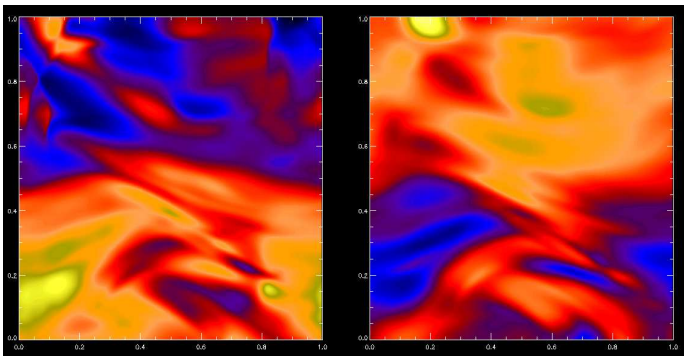

Figure 2.18: $2D$ contours of density (left) and magnetic field strength (right) at time $t = 16\ \tau_A$.

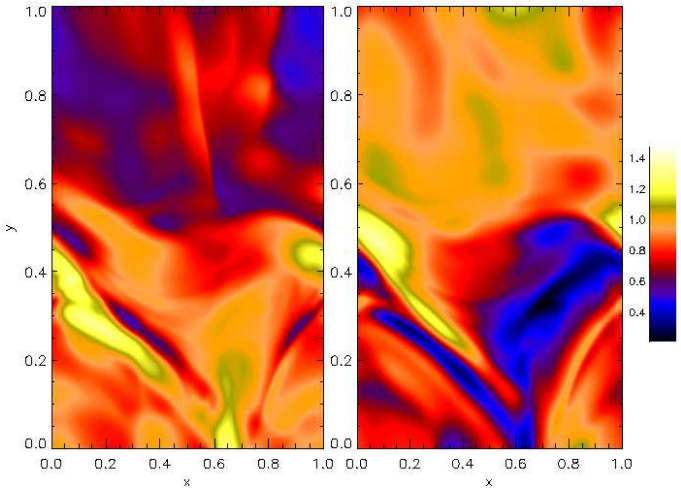

Figure 2.19: $2D$ contours of density (left) and magnetic field strength (right) at time $t = 19\ \tau_A$.

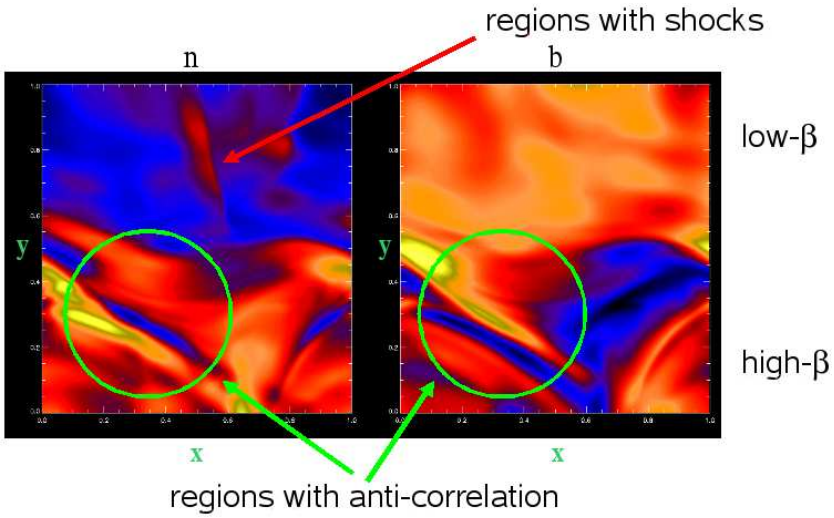

Figure 2.20: The region is highly turbulent and mixed, nonetheless there is a strong difference between low–β region (Region B, $y > 0.5$) and high–β region (Region A, $y < 0.5$): anti–correlated structures appears in high–β, while shock–wave propagate in low–β region.

respect to the equilibrium, namely $\delta n(x^*, y, t) = n(x^*, y, t) - n_{eq}(y)$ and $\delta b(x^*, y, t) = |B(x^*, y, t)| - |B_{eq}(y)|$, obtained by performing a cut along a value of x, namely $x^* = 0.5$ at times $t = 5\tau_A$ (linear stage of simulation) and $t = 18\tau_A$ (after saturation). When a stationary state is reached, the signal looks quite similar to that observed by Cluster mission, shown in Fig. 2.3.
In order to investigate the dependence on β we performed a cut for a fixed value of y in the quantities $\delta n(x, y^*, t)$ and $\delta b(x, y^*, t)$, as a function of x. In Fig. 2.22 we report, for $t = 17\tau_A$, the two quantities in the Region A ($y^* = 0.25$) and in the Region B ($y^* = 0.75$), respectively. Figures underlines the different magnetosonic turbulence that spontaneously develops in these two regions: in the high beta region, there is a clear evidence of slow magnetosonic, large amplitude fluctuations, while in the Region B, anti–correlated modes are less frequent, rather shock waves appear. As a further analysis in Fig. 2.23 we report the values of the correlation coefficient between density and magnetic field, averaged over the x direction, as a function of y at three

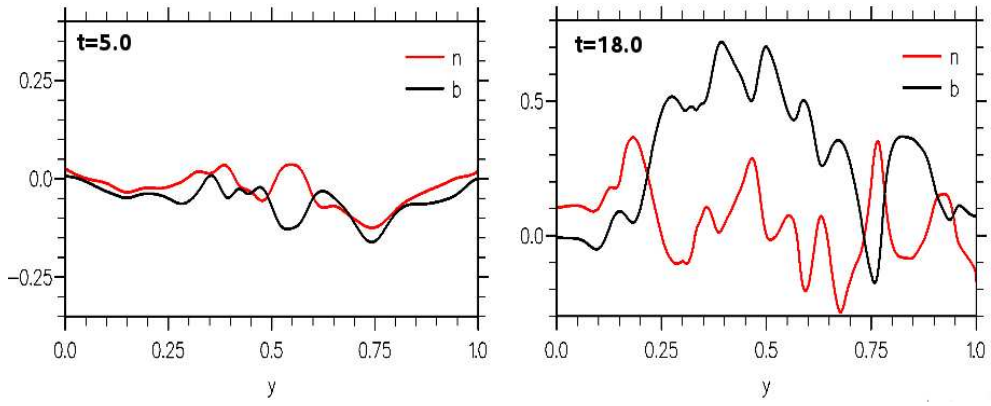

Figure 2.21: Fluctuations of density (red line) and magnetic field intensity (black line) at $t = 5.0\ \tau_A$ (left panel, before the saturation time) and $t = 18\ \tau_A$ (right panel, after the saturation time) as a function of the inhomogeneous direction y. When a stationary state is reached, strong anti–correlated fluctuations in the direction perpendicular to the mean magnetic field appear. These results can be compared with observations in Fig. 2.3.

different times, defined as:

$$C_{n,b}\ (y,t) = \frac{1}{\int_0^1 |\delta n(x,y,t)\delta b(x,y,t)|dx} \int_0^1 \delta n(x,y,t)\delta b(x,y,t)dx \qquad (2.22)$$

The anti–correlation in the high–β region develops during the formation of the energy spectrum (for $t < 10\tau_A$), and is then maintained during the saturation phase (for $t > 10\tau_A$). After that a statistically stationary state is reached, in Region A, $C_{n,b}(y,t) \simeq -1$, while $C_{n,b}(y,t) \to 0$ in the Region B. Note that the correlation is not completely zero in the Region B. This means that some anti–correlated structures can survive also where the plasma is more magnetized, as shown in Fig. 2.24.
Anti–correlated structures correspond to small–scale magnetosonic fluctuations that are spontaneously generated during the nonlinear evolution. These structures can be compared with Cluster observations (cfr. Ref. [39]), where a general anti–correlation between the density and the magnetic field intensity profiles appears. We then conjecture that the small–scale structures observed in space plasma could be generated during the nonlinear evolution of turbulence. In the low–β region, apart for strong gradients, slow magnetosonic

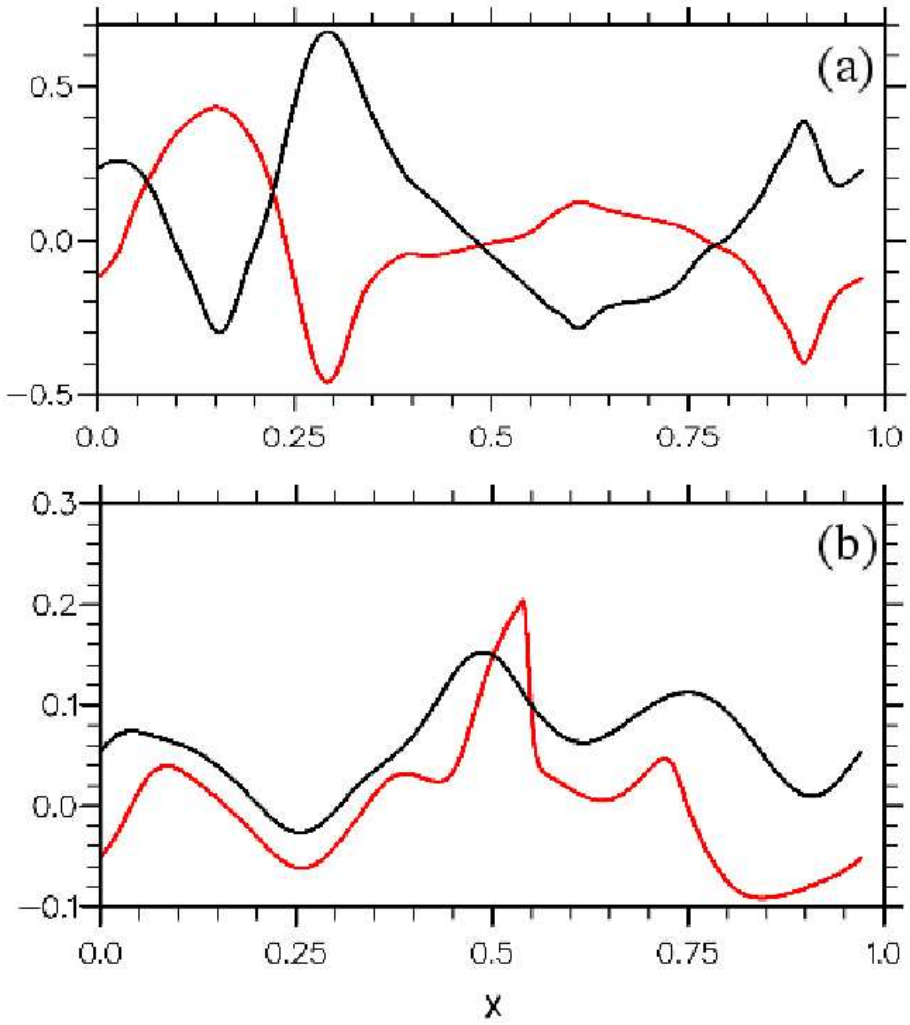

Figure 2.22: In the panel (a) is reported the density (red line) and magnetic field profile (black line) as a function of the periodic coordinate for $y = 0.225$ (Region A), in the panel (b) for $y = 0.75$ (Region B). There is a clear difference between these two regions: going from Region A to Region B anti–correlated structures evolves in shock waves.

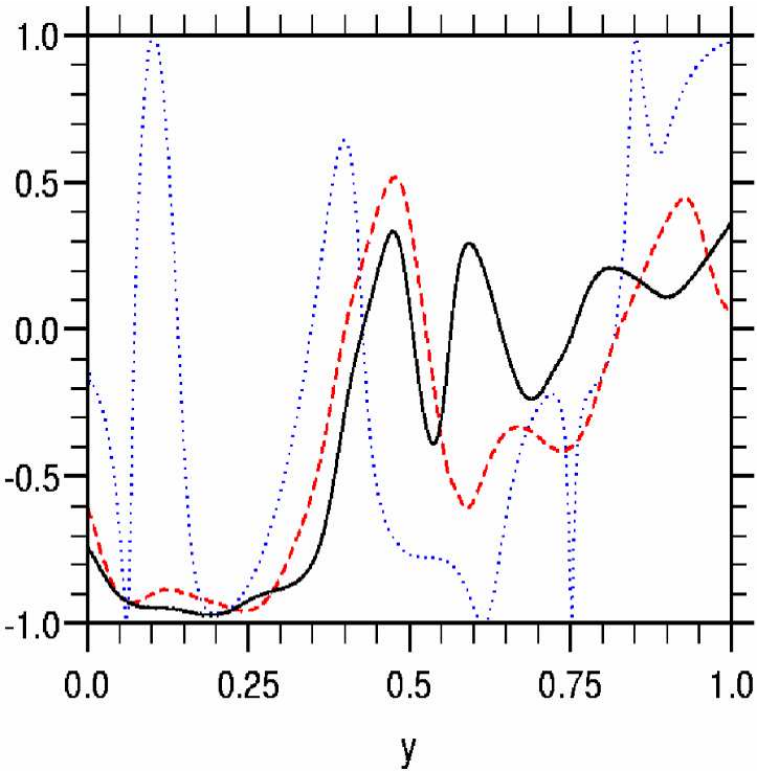

Figure 2.23: The correlation coefficient $C_{n,b}\ (y,t)$ between the density and magnetic field intensity, averaged over x, is reported as a function of y for three different times, namely $t = 5\tau_A$ (dotted blue line), $t = 12\tau_A$ (dashed red line) and $t = 20\tau_A$ (solid black line).

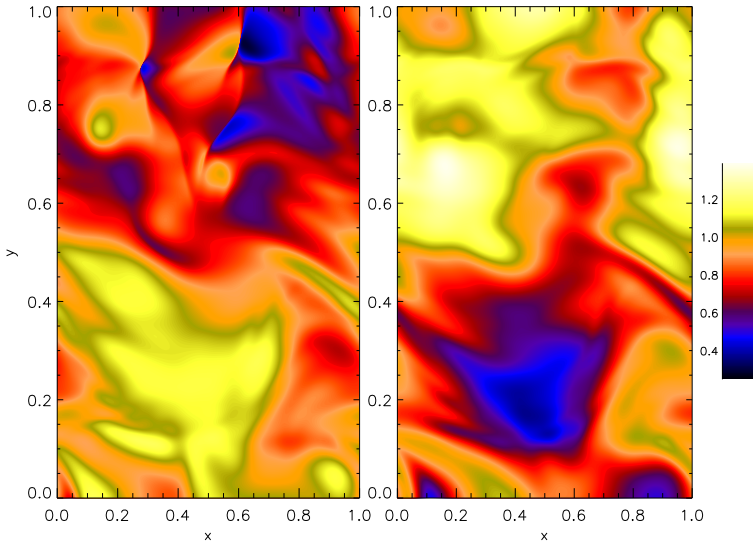

Figure 2.24: 2D contour of density (left) and magnetic field strength (right). At position ($x \simeq 0.17$,$y =\simeq 0.75$) a magnetosonic structure (slow–type) penetrates the low–β region.

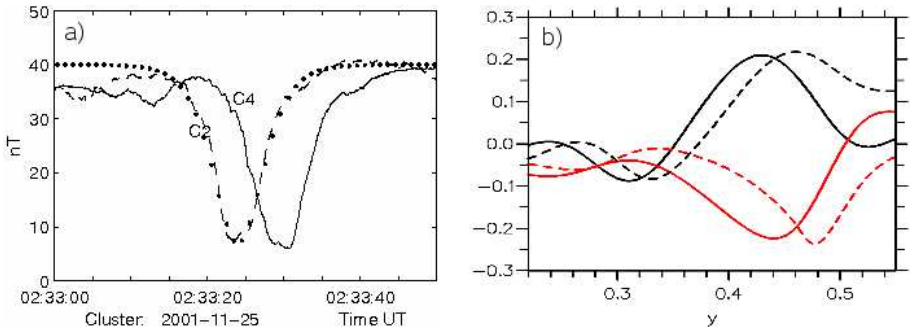

Figure 2.25: The panel a) represents a magnetic structure detected by two Cluster spacecrafts (C2, C4) with a relative time delay of $6s$ which corresponds to a velocity $250km/s$, deduced from the known separation distance between the satellites. In panel b), we report a single structure coming from numerical simulation. The solid line is taken at $t = 15.0\tau_A$ and dotted lines at $t = 15.5\tau_A$. Red line represents density and black line the magnetic field.

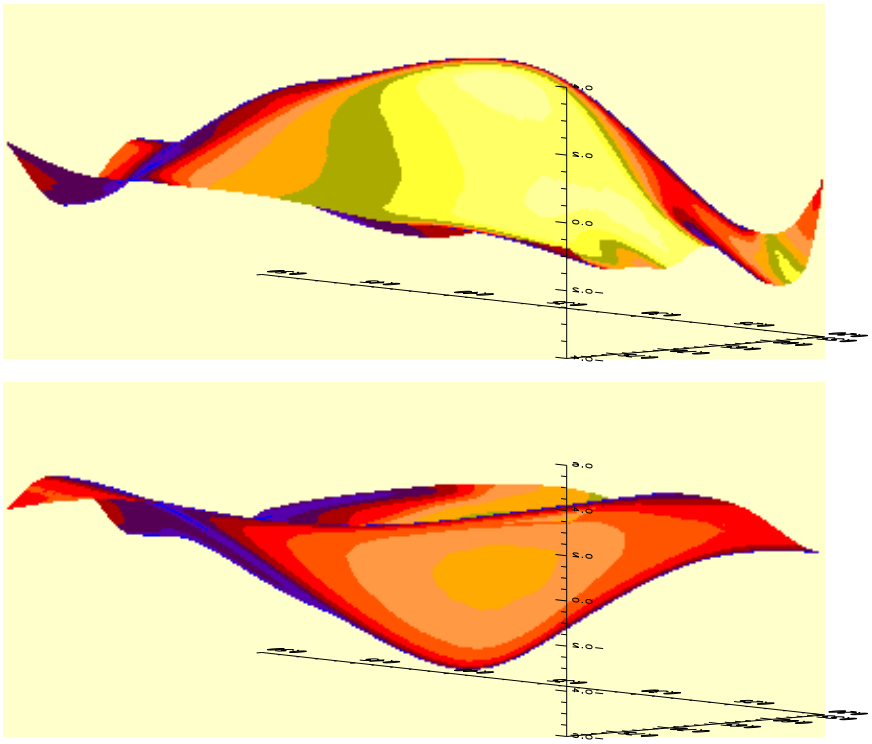

Figure 2.26: Shade surfaces of a pressure–balanced structure. Density is shown in the upper panel and magnetic field intensity in the lower panel.

structures survive. In Fig. 2.25 the profile of one single structure coming from our numerical simulations is reported at two different times [panel (b)]. As a comparison, a traveling structure detected in the space plasma by the Cluster satellites is also reported [panel (a)]. This kind of fluctuations are quite similar to solitons even if they cannot be considered as solitary waves. In Fig. 2.26 a $3D$ reconstruction of this density and magnetic field profile of a single anti–correlated structure is shown. The anti–correlation within turbulence grows during the excitation of small–scales, namely for times $t < 10\tau_A$, and is then maintained statistically stationary during the saturation phase ($t \geq 10\tau_A$).

2.5.3 Comparisons between Hall MHD and MHD

To investigate the difference of compressible MHD from compressible Hall MHD during the nonlinear energy cascade we calculate the Fourier coefficients for velocity field fluctuations $\delta\mathbf{v}(m_x, y, t)$, magnetic field fluctuations $\delta\mathbf{b}(m_x, y, t)$ and density fluctuations $\delta n(m_x, y, t)$, through a 1D Fourier transform of the fields along the x direction, using a superposition of Eq. (2.20). In Fig. 2.27 we report, as a function of m_x, the squared modulus of Fourier coefficients of fluctuations, namely $\sum_i |\delta u_i(m_x, y, t)|^2$, $\sum_i |\delta b_i(m_x, y, t)|^2$ and $|\delta n(m_x, y, t)|^2$, averaged over all times, for two different values of y. The corresponding MHD results are shown in the insets for comparison. In both MHD and Hall MHD cases at large scales the compressive part of fluctuations seems to be scarcely relevant, that is density fluctuations are lower than both velocity and magnetic field fluctuations. Turbulence, at larger scales, is Alfvénic [108], that is velocity and magnetic fluctuations are correlated up to a high degree[9]. A striking difference between MHD and Hall MHD is instead found at scales smaller than the scale k_H where the Hall effect starts to play a role. In fact, at these scales the coupling between velocity and magnetic fluctuations breaks down, while both fields seems to play an opposite role as far as Regions A and B are concerned. In Region B the velocity field is strongly coupled with density, while a depletion of the magnetic field is observed. On the contrary, in Region A, even if the situation is more confused, the magnetic field is coupled with density. Both features represent the spec-

[9]This kind of turbulence resembles linear Alfvén waves. Alfvén waves are transverse magnetic tension waves which travel along magnetic field lines and can be excited in any electrically conducting fluid permeated by a magnetic field. Hannes Alfvén deduced their existence from the equations of electromagnetism and hydrodynamics.

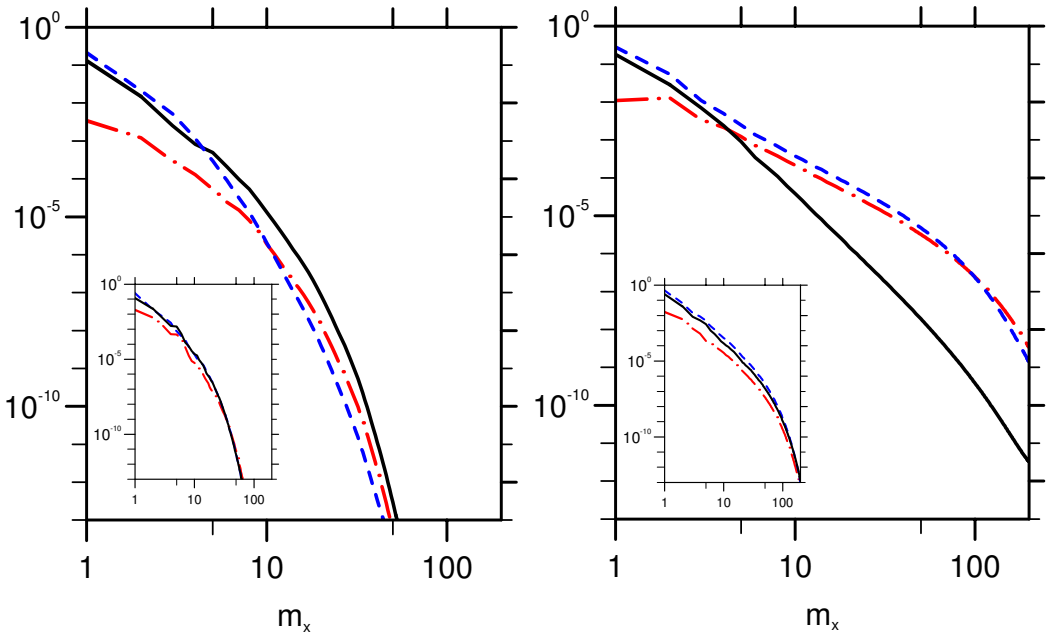

Figure 2.27: The time averaged wavenumber spectra of square modulus for density (dashed red lines), magnetic field (full black lines) and velocity field Fourier coefficients (dotted blue lines), extracted at $y = 0.2$ (left panel) and $y = 0.8$ (right panel). Insets refer to compressible MHD simulation shown for comparison.

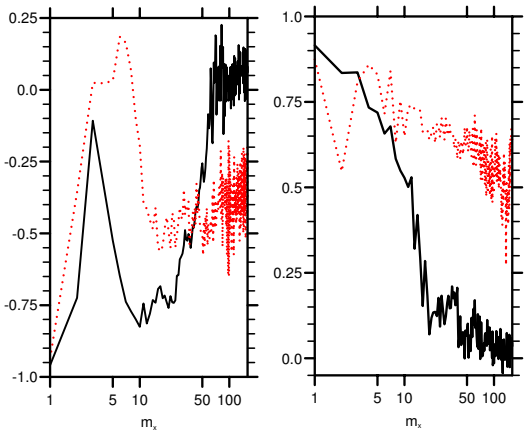

Figure 2.28: The wavenumber spectra of time averaged cross–correlation between velocity and magnetic fluctuations $\langle C_{\mathbf{v},\mathbf{b}}(m_x, y^*)\rangle_t$ calculated for both MHD (red dotted line) and Hall MHD (black full line), are reported for $y^* = 0.2$ (left) and $y^* = 0.8$ (right).

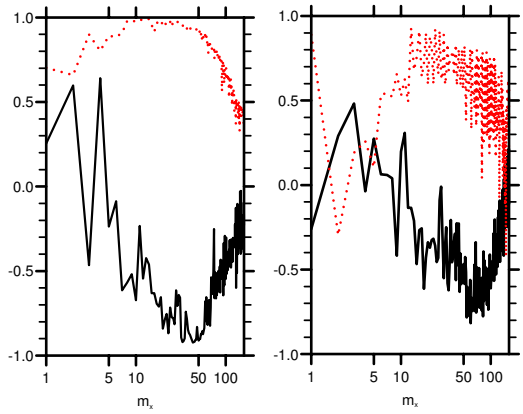

Figure 2.29: The wavenumber spectra of time averaged cross–correlation between the x–component of the velocity fluctuations and density $\langle C_{v_x,n}(m_x, y^*)\rangle_t$ calculated for both MHD (right) and Hall MHD (left). Curves refer to two different values of y^*, namely $y^* = 0.8$ (red dotted line) and $y^* = 0.2$ (black full line).

tral counterpart of the spontaneous generation of small–scale magnetosonic mode fluctuations, starting from Alfvénic turbulence. As a further evidence Region A seems to be completely emptied out of fluctuations at the smallest scales with respect to Region B. This is a characteristic we found also in the purely MHD simulation. To better describe the phenomenon of different correlations, in Figs. 2.28 and 2.29 we report, for two values of y, at a single time, the Fourier spectra of the cross–correlations between velocity and magnetic field fluctuations, (Fig. 2.28) respectively, and between the x component of the velocity and density fluctuations (Fig. 2.29). As it can be seen the strong correlation between $\delta\mathbf{v}$ and $\delta\mathbf{b}$ observed at small wave–vectors decays for higher wave–vectors in both Regions A and B. Alfvénic fluctuations at the Hall scale k_H^{-1} become dispersive, and the Hall term breaks the strong link between velocity and magnetic field that is characteristic of MHD [13]. The high correlations between the x component of the velocity and density which are present in Region B, is lost in Region A, instead.

2.6 Conclusions

To summarize, we numerically investigated the time evolution of forced compressible Hall MHD in a 2.5D configuration. We found that small–scale structures are spontaneously excited during the nonlinear evolution, these structures being characterized by a strong anti–correlation between density and magnetic field intensity at higher β, while, on average, the strong anti–correlation is destroyed for lower β values. These structures have been observed in space plasma during the numerous crossing of the MPBL by the Cluster mission. We conjecture that the observed structures are generated by nonlinear effects, that is they correspond to a magnetosonic–mode turbulence rather than to an ensemble of soliton–like ordered structures [39, 40]. The anti–correlation between density and magnetic field intensity is mainly efficient at the scale length where the Hall effect takes place. Then this kind of turbulence is a genuine result of Hall MHD.

Chapter 3

"Bursty Turbulence" in Laboratory Plasmas

Turbulent plasma fluctuations are commonly observed at the edge of laboratory plasmas [109–112]. These fluctuations can propagate from the hot plasma core to the region between the plasma edge and the wall of the device, namely the *Scrape–Off Layer* (SOL). *Bursts* in laboratory plasmas are generally observed as the generation and transport of high density structures localized both in space and time [46, 113, 114]. Moreover a strong correlation has been found between bursts in the SOL and the density limit in tokamak [115–117], as well as between electrostatic fluctuations in the edge plasma of RFP and magnetic relaxation events at the center of the plasma column [118]. This suggests that enhancement of transport, sudden and localized (both in space and in time), may be responsible for the disruptive limit. We named the complex dynamics of bursts in space and in time "bursty turbulence". However, despite of a wealth of experimental data, there is little direct quantitative or even qualitative understanding of these measurements in terms of the basic theory of *edge plasma turbulence*, which has advanced rapidly in the past few years [9, 112, 119]. Investigating bursty turbulence is then of primary interest not only as a non trivial example of nonlinear dynamics, but also for fusion devices, where a suppression of turbulent bursts might be welcomed [112, 120].

Since the magnetic field is stationary ($\partial \mathbf{B}/\partial t \simeq 0$), the edge turbulence assumes, with a good approximation, an electrostatic nature and develops essentially in a two-dimensional plane, *i. e.* the plane perpendicular to $\mathbf{B}$. Then, the most interesting dynamics lye in the radial–poloidal plane of a

toroidal or linear device. Moreover the radial velocity of bursts corresponds, to a good approximation, to the $\mathbf{E}\times\mathbf{B}$ drift ($\mathbf{E}$ is the electric field) [121,122]. In this Chapter we numerically investigate dynamics of two–dimensional $\mathbf{E}\times\mathbf{B}$ turbulence in a polar geometry, similar to a section, perpendicular to the mean magnetic field, of a linear device. The bursty turbulence is generated and maintained by a random forcing term. No dissipative terms are artificially introduced into the simple evolution equations, rather bursts (or *blobs*) interact and propagate radially before being absorbed by boundaries. Even if the model is very simple, a good agreement between simulation results and real data is observed in particular concerning the shape of bursts, the electrostatic potential and the statistics of the radial flux. Some turbulent statistical properties of the bursty turbulence are then investigated and discussed.

3.1 Intermittent turbulence in laboratory plasmas

Intermittency is often referred to the anomalous scaling behaviour of turbulent fluctuations, and this is known in literature as the process of intermittency in fully developed turbulence [12, 123]. A signature of intermittency in turbulent measurements is a non–gaussian amplitude of *Probability Distribution Function* (PDF), *i. e.* the presence of longer tails caused by the appearance of large-amplitude events [124]. This kind of intermittency is ubiquitous in the edge of magnetic confinement laboratory plasmas including tokamaks [9], RFPs [118], and linear devices [46,125–127]. The intermittency in these environments is generally attributed to the creation and propagation of filamentary magnetic field–aligned structures [111].
At least to a rough level, this kind of process is actually different from intermittency in fully developed turbulence. However, it is clear that blobs represent a non–homogeneous process both in space and time, and in this sense we can call this process as "intermittency".
The relative density fluctuation levels of plasma, at the edge of devices, are generally large, typically $\delta n/n > 10\%$, compared to the relatively small turbulence levels near the core ($\delta n/n \simeq 1\%$) [112]. Large amplitude fluctuations in measurements are therefore due to the transit of high-density structures through the low-density edge region. The outward propagation of these struc-

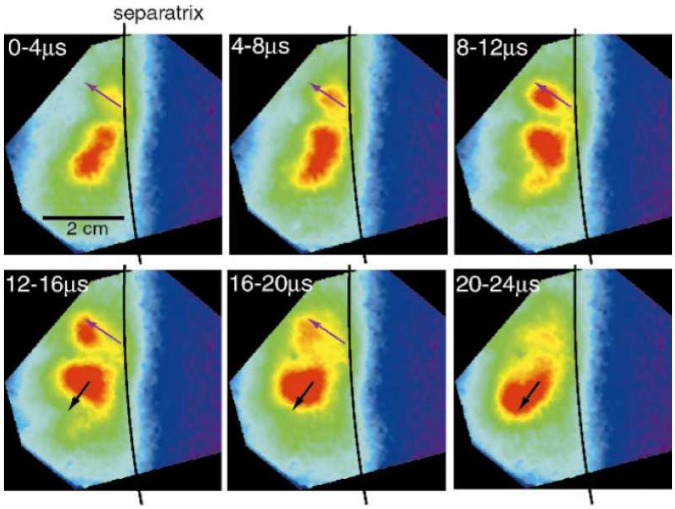

Figure 3.1: 2D images of edge turbulence in the the Alcator C-Mod tokamak [113]. A sequence of images taken with a camera at 4 $ms/frame$ and 250000 $frames/s$. The movement of two locally bright "blobs" is tracked over several frames showing their velocity of up to 1 $cm/20\ \mu s$. The separatrix delimits the SOL.

tures results in significant particle transport in the edge of magnetic confinement devices. Typical 2D–imaging of a burst in a tokamak device[1], detected at different times by a camera, is shown in Fig. 3.1 [113]. The structure was moving from the hot core toward the edge of the camera.
In Fig. 3.2 the time trace of the plasma density n (Fig. 3.2–A), the poloidal electric field E_θ (Fig. 3.2–B) and the radial flux (Fig. 3.2–C)

$$\Gamma = \frac{1}{B_T}\langle nE_\theta \rangle$$

are shown. Here, B_T is the toroidal magnetic field (data come from measurements near the wall of another tokamak device[2] [122]). Each spike (enhancement of plasma density) corresponds to a burst that propagate outward from the core. Such peaks can be caused by an intermittent formation of objects in the plasma periphery, like the blob shown in Fig. 3.1.

[1]The device is the Alcator C-Mod. This project is a compact size and high performance tokamak located at the Massachusetts Institute of Technology.

[2]T–10 Tokamak is a device located in the Russian Research Centre Kurachatov Institute, Institute of Nuclear Fusion, Moscow.

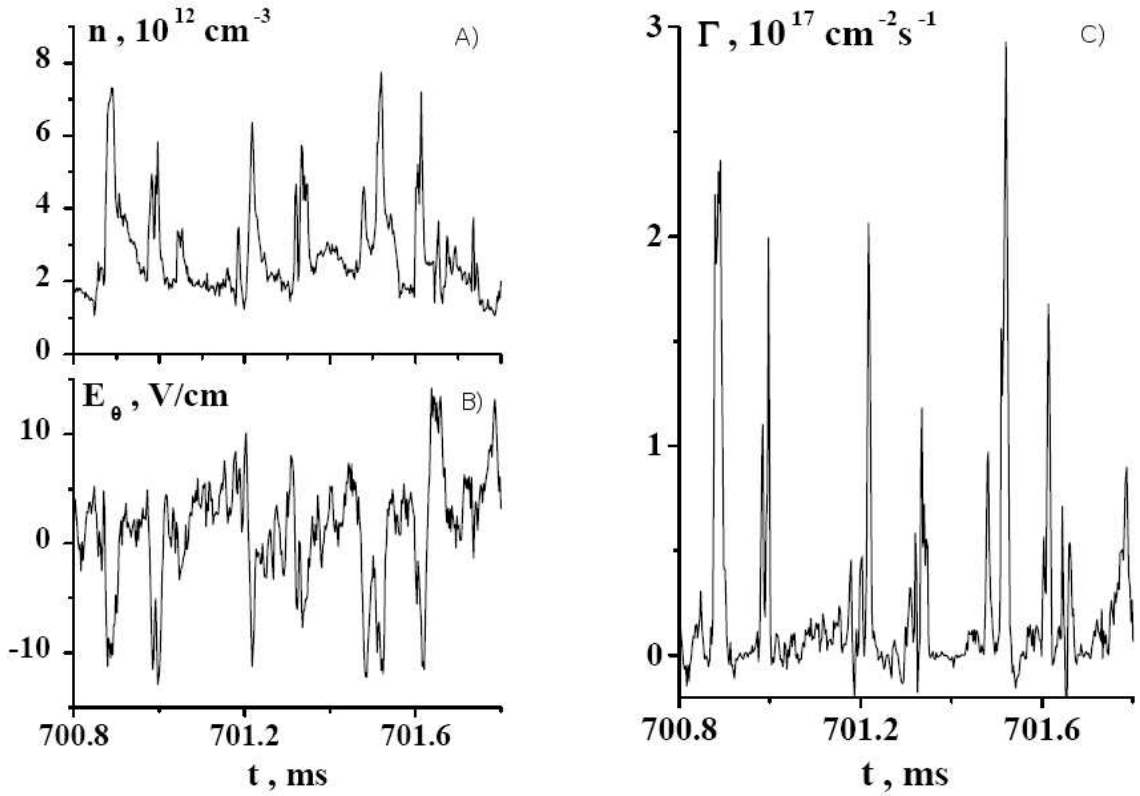

Figure 3.2: Intermittent signals in the SOL of T–10 Tokamak [122]: A) Time evolution of the plasma density, B) the poloidal electric field and C) the radial particle flow Γ. Plasma density exceeds $\simeq 3$ times the density of background plasma. Density and poloidal electric field signals seem to be correlated, this is a signature that every spike *transports* poloidal electric field fluctuation.

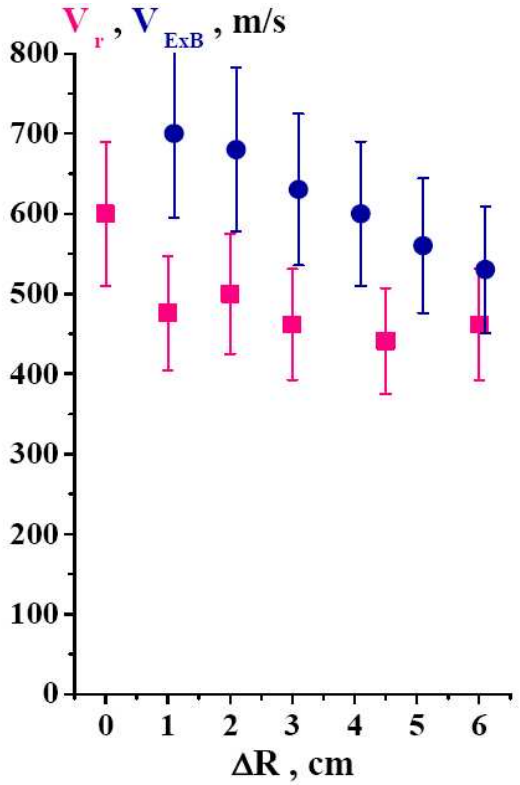

Figure 3.3: The radial distributions of radial speed V_r of the plasma objects and radial electric drift velocity $V_{E\times B}$. Data comes from observation in T–10 Tokamak [122].

Once structures are produced and ejected into the low-density region, they continue to propagate across the magnetic field lines due to the $\mathbf{E}\times\mathbf{B}$ drift velocity:

$$\mathbf{V_{E\times B}} = \frac{\mathbf{E}\times\mathbf{B}}{|\mathbf{B}|^2} \tag{3.1}$$

This hypotesis comes from observations of structures that move with high outward radial speed V_r, comparable with $V_{E\times B}$ (see Fig. 3.3) . This can be assumed as an evidence for the fact that the radial motion of the plasma is defined by the poloidal electric field fluctuations, and so it is consistent with the assumption of an electrostatic turbulence [112, 121, 122, 128, 129].
A typical bursty event, taken from T–10 Tokamak [122], is shown in Fig. 3.4.

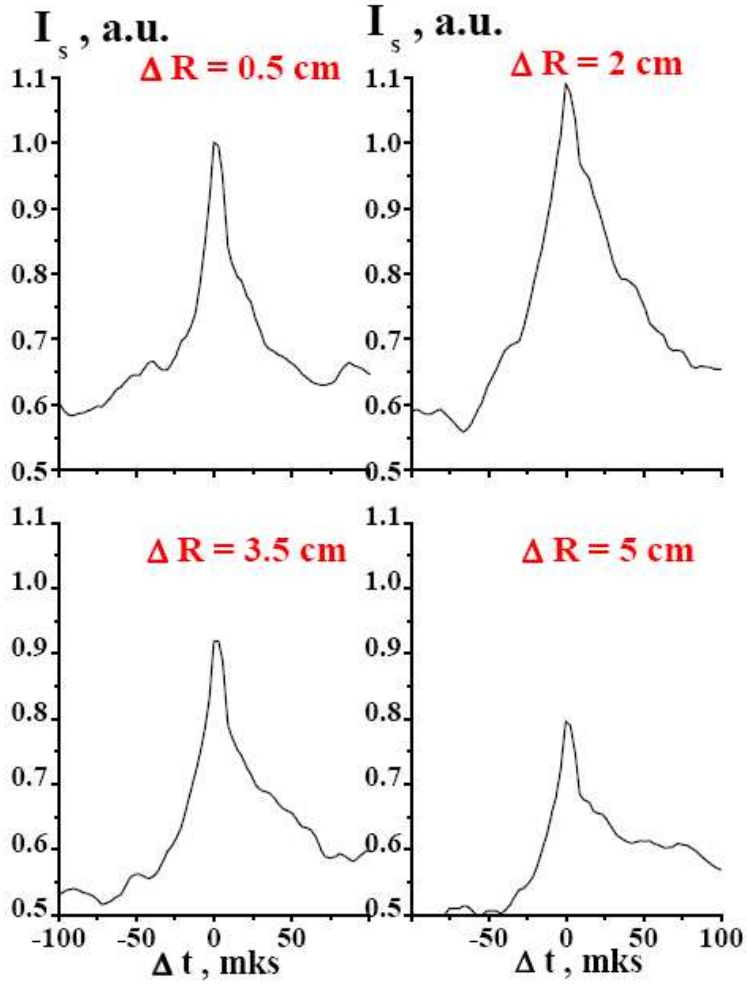

Figure 3.4: Conditional averaging results of the saturation current signals I_s in different radial location in the T–10 Tokamak. The I_s signal is proportional to the radial shape of a blob that is moving from the right to the left side of the plot. The amplitude diminishes with increasing the radius.

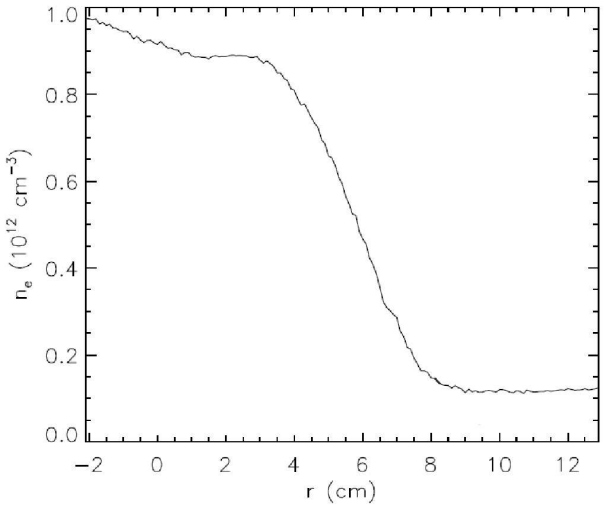

Figure 3.5: Spatial profile of the density in the LAPD experiment($x = 0$ at the limiter edge).

In the plots, conditional averages of the saturation current I_s, which is proportional to the shape of the signal, are shown at different radial distances. A typical steep front and smooth tail is displayed. As it can be seen, the shape of bursts is more asymmetric near boundaries, and the amplitude decreases moving away from the core.
In the LAPD experiment (see Fig. 1.10) steep gradients in plasma density are observed behind the limiter, along with very large amplitude fluctuations. Fig. 3.5 shows a measurement of the radial profile of plasma density (n_e) downstream from the limiter. The observed density gradient is very steep with a scale length of the order of a few centimeters. In the limiter shadow, the density profile is quite flat, similar to the profiles observed in the SOL of tokamaks [130]. The density behind the limiter represents a significant fraction of the core density, indicative of substantial cross-field particle transport. Two–dimensional measurements in the LAPD show that blobs are isolated structures with a dipolar potential, very similar to that observed in tokamaks. The conditional average of many blob events using the saturation current signal (I_{sat}) as a function of radial position is shown in Fig. 3.6–(a) [46, 131]. The conditional average was used by authors [46] to reconstruct the blob shape. The blob event is asymmetric in time, with

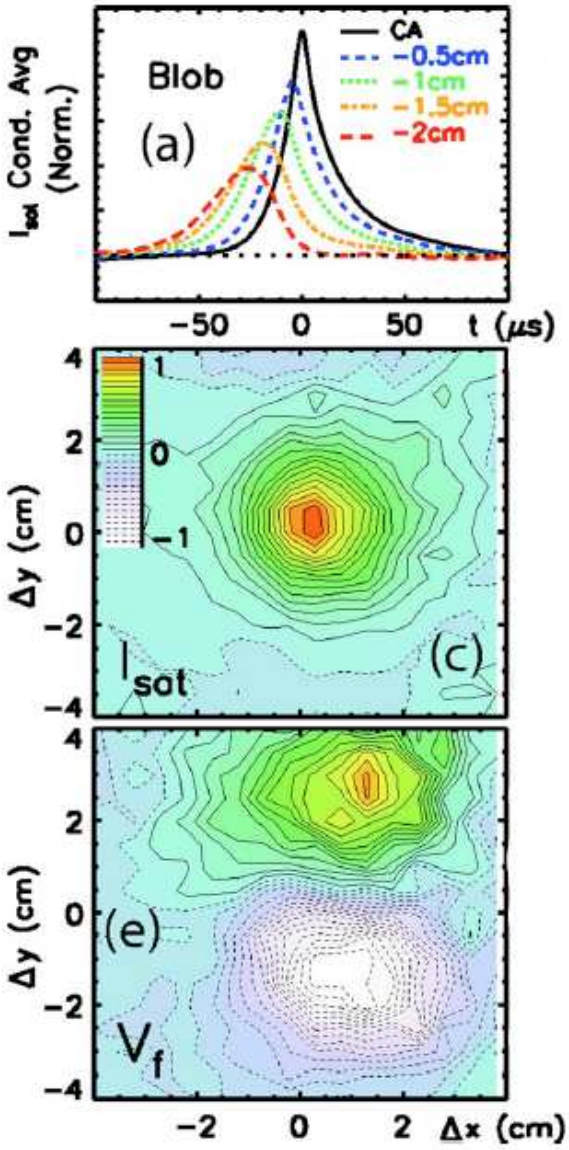

Figure 3.6: Cross–conditional average of I_{sat} on the linear probe array for a blob: (a) two-dimensional cross–conditional averages of blob; (c) I_{sat} and (e) the electrostatic potential V_f. All 2D conditional averages are normalized to the maximum of the absolute value of the average, and the color bar in (c) applies also to (e).

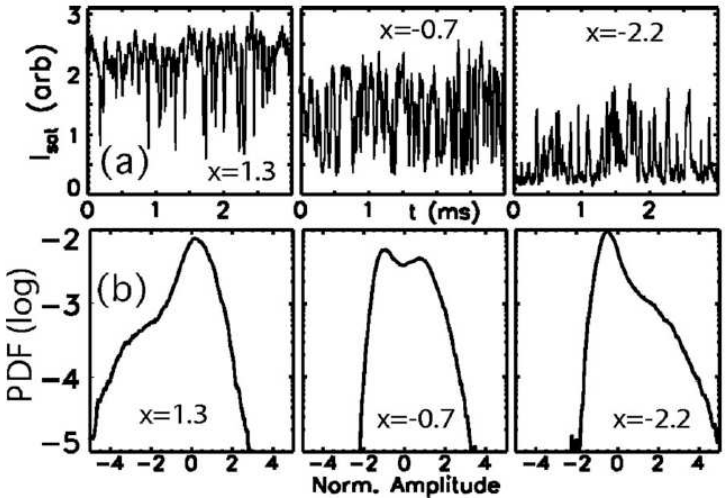

Figure 3.7: (a) Example of raw I_{sat} signals at three spatial locations (before the density gradient on the left panel, within the density gradient in the middle panel, and near the edge on the right panel). (b) PDFs of the signal's amplitude at the same three locations [46].

a fast rise and a slow decay. The average shape of blob appears to travel across the probe array out into the low–density region with a speed of about $10^3 m/sec$. Figures 3.6 (c) and (e) show the $2D$ cross–conditional average of I_{sat} and V_f [46,132], respectively, for blob events (the fixed probe was located near the edge). The blob is clearly an isolated, detached structure. The V_f measurements clearly show a dipolar structure of the potential associated with the blob. The potential structure is consistent with $\mathbf{E} \times \mathbf{B}$ propagation almost entirely from the core to the edge.

In Fig. 3.7(a) an example of I_{sat} signals measured at three different radial locations is shown. On the core side of the gradient region the signal is dominated by downward–moving events, while on the low–density side of the gradient region the signal is dominated by upward–moving events. The upward–moving events in the low–density region are density enhancements or blobs, similar to those observed in the edge of many magnetic confinement devices [123, 130, 133].

Several mechanisms have been proposed for the generation of the above structures [134–140], but the effective mechanism is yet unclear [141–144].

The following features of an averaged bursty event can be remarked:

1. density enhancements near the boundaries essentially propagating outward;
2. averaged positive signal is asymmetric, showing an abrupt increase and a smoother decrease. This can be interpreted as a radial movement of plasma objects with a steep front followed by a long tail;
3. the radial flux displays an intermittent–behaviour;
4. the radial velocity of structures is approximately due to the $\mathbf{E}\times\mathbf{B}$ drift;
5. blobs exhibit a dipolar structure of the electrostatic potential;
6. the amplitude of averaged bursts has a radial dependence.
7. the skewness of PDF of amplitudes depends on the distance from the core.

3.2 A simple "E × B" model

We built–up a numerical model which tries to reproduce some of the features just described. The model we used to investigate the generation of electrostatic $\mathbf{E}\times\mathbf{B}$ turbulence is kept as simpler as possible. We consider a column of plasma of radius a, described by the charge densities for the α^{th} specie ρ_α. We use a cylindrical geometry with coordinates (r,θ,t), and we assume that a constant magnetic field is maintained along the axis of the column $\mathbf{B}=B_0\hat{e}_z$. Dynamics, as sketched in Fig. 3.8, develop on the (r,θ) plane. We assume that all quantities keep constant along the z coordinate. At the center of the polar plane we put a source of charges, by assuming that they are continuously generated at a rate F_α. Charge–difference generates an electric field which can be written in terms of a potential $\phi(r,\theta,t)$, so that they undergo to the $\mathbf{E}\times\mathbf{B}$ drift with velocity defined by Eq. (3.1). The dynamic behaviour of the system can be described by the following dimensionless equations:

$$\frac{\partial n}{\partial t} = -\left(\mathbf{u}\cdot\nabla\right)n + f \tag{3.2}$$

$$\nabla^2\phi = n \tag{3.3}$$

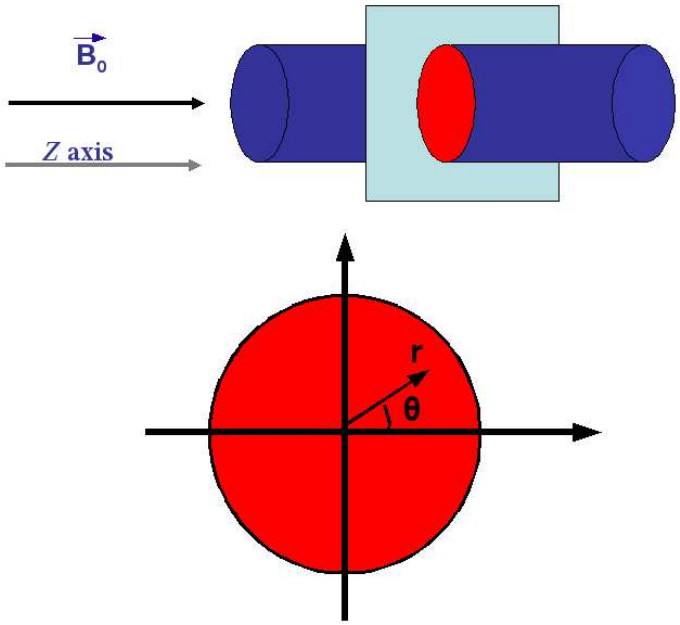

Figure 3.8: A sketch of the geometric approximation used in the "$\mathbf{E} \times \mathbf{B}$" model.

where $n(r, \theta, t) = n_e - n_i$ is the charge density difference, and $f(r, \theta, t) = F_e - F_i$ is the forcing rate. By using dimensionless quantities, lengths are measured in terms of a (namely $0 \leq r \leq 1$), charges are written in terms of $n_\alpha = \rho_\alpha / \rho_0$ (being ρ_0 a reference charge unit), velocity to $\mathbf{u} = \mathbf{V}_{\mathbf{E}\times\mathbf{B}}/u_{dr}$, being $u_{dr} = \rho_0 a / \epsilon_0 B_0$ the drift speed of a charge unit, the potential to a characteristic field $\rho_0 a^2/\epsilon_0$, and times to a/u_{dr}. The velocity of fluid is given by

$$\mathbf{u}(r, \theta, t) = -\nabla\phi \times \hat{e}_z \tag{3.4}$$

A perfect absorption for the charge density has been assumed at the boundary $r = 1$, so that we avoid the introduction of artificial dissipative terms in the simple evolution equation Eq. (3.2). At the boundary $r = 1$ the potential is assumed to vanish on average, namely $\langle \phi(1, \theta, t) \rangle_\theta = 0$.
Let us consider Eqs. (3.2)–(3.4) in a periodic two–dimensional domain by assuming homogeneity, and let us introduce the Fourier decomposition

$$\phi(\mathbf{x}, t) = \sum_{\mathbf{k}} \phi_{\mathbf{k}}(t) e^{i\mathbf{k}\cdot\mathbf{x}} \tag{3.5}$$

and

$$n(\mathbf{x},t) = \sum_{\mathbf{k}} n_{\mathbf{k}}(t) e^{i\mathbf{k}\cdot\mathbf{x}} \tag{3.6}$$

By using these definitions from equations (3.3) and (3.4) we obtain

$$\phi_{\mathbf{k}}(t) = -\frac{n_{\mathbf{k}}(t)}{k^2} \tag{3.7}$$

and

$$\mathbf{u}_{\mathbf{k}}(t) = i n_{\mathbf{k}} \frac{\mathbf{k}\times\hat{e}_z}{k^2} \tag{3.8}$$

Finally by using Eqs. (3.5)–(3.8), after some algebra we obtain the evolution equation for the Fourier coefficients of the density fluctuations

$$\frac{\partial n_{\mathbf{k}}(t)}{\partial t} - \sum_{\mathbf{p}+\mathbf{q}=\mathbf{k}}^{\Delta} M_{\mathbf{k},\mathbf{p},\mathbf{q}} n_{\mathbf{p}}(t) n_{\mathbf{q}}(t) = f_{\mathbf{k}}(t) \tag{3.9}$$

where

$$M_{\mathbf{k},\mathbf{p},\mathbf{q}} = \frac{1}{2}\frac{\mathbf{q}\cdot\mathbf{p}}{p^2+q^2}$$

Equation (3.9) has the same mathematical aspect of the usual Navier–Stokes equation for turbulence [11], so we expect that nonlinear interactions will be responsible for the energy transfer among scales. An equation can be written for the two–points correlations

$$N_{\mathbf{k}}(t) = \langle n_{\mathbf{k}}(t) n_{-\mathbf{k}}(t)\rangle$$

thus obtaining from Eq. (3.9):

$$\frac{\partial N_{\mathbf{k}}(t)}{\partial t} - \sum_{\mathbf{p}+\mathbf{q}=\mathbf{k}} M_{\mathbf{k},\mathbf{p},\mathbf{q}} \langle n_{-\mathbf{k}}(t) n_{\mathbf{p}}(t) n_{\mathbf{q}}(t)\rangle = \langle n_{-\mathbf{k}}(t) f_{\mathbf{k}}(t)\rangle \tag{3.10}$$

When we assume a statistically stationary state we see that the third–order moment for density is related only to the correlations between the forcing term and the density, but is independent on $N_{\mathbf{k}}(t)$. Of course this is due to the absence of a classical dissipative term proportional to a power of k, and this situation makes bursty turbulence very interesting, even from a theoretical point of view. The third–order moment, mainly in a inhomogeneous situation, can be better investigated in the real space, so in the following section we recover an equation like (3.10) in the inhomogeneous case.

3.3 The third–order mixed correlations

We can investigate the properties of turbulence by investigating the time evolution of the average "energy" associated to the charge density. Using the same procedure as Monin and Yaglom [145], let us consider two points $\mathbf{r}$ and $\mathbf{r}' = \mathbf{r} + \ell$ separated by a distance ℓ, and let us write the evolution equations for fields calculated at both points

$$\begin{aligned} \partial_t n + u_\alpha \partial_\alpha n &= f \\ \partial_t n' + u'_\alpha \partial'_\alpha n' &= f' \end{aligned}$$

the suffix " $'$ " refers to quantities calculated at $\mathbf{r}'$ ($\partial'_\alpha \equiv \partial/\partial r'_\alpha$). We assume that quantities calculated at one point are independent with respect to derivatives made with the other point, namely $\partial'_\alpha n = \partial_\alpha n' = 0$. By subtracting the second equation from the first, and by defining the differences $\Delta n = n' - n$ and $\Delta f = f' - f$, using the independence of densities calculated at two points with respect to derivatives, we get

$$\partial_t \Delta n + u'_\alpha \partial'_\alpha \Delta n + u_\alpha \partial_\alpha \Delta n = \Delta f$$

Then by adding and subtracting the following quantity $u_\alpha \partial'_\alpha \Delta n$ on the r.h.s of the equation we obtain

$$\partial_t \Delta n + \Delta u_\alpha \partial'_\alpha \Delta n + u_\alpha \left(\partial_\alpha + \partial'_\alpha\right) \Delta n = \Delta f$$

The equation for the averaged energy can be derived by multiplying the equation by $2\Delta n$ and averaging, so that

$$\partial_t \langle \Delta n^2 \rangle + \langle \partial'_\alpha \Delta u_\alpha \Delta n^2 \rangle + \langle u_\alpha \left(\partial_\alpha + \partial'_\alpha\right) \Delta n^2 \rangle = 2 \langle \Delta n \Delta f \rangle$$

(we used the incompressibility of the velocity field, say $\partial_\alpha u_\alpha = 0$). By assuming that the system is locally homogeneous[3] we can say that, when

[3]Local homogeneity is different from global homogeneity. Actually systems that are far from being globally homogeneous can be locally homogeneous. Local homogeneity means that statistics are very rapidly varying with respect to ℓ, relative to its variation with respect to $\mathbf{X} = (\mathbf{r} + \mathbf{r}')/2$, provided that ℓ is sufficiently small. On this basis when derivatives with respect to $\mathbf{r}$ and $\mathbf{r}'$ are transformed into derivatives with respect to ℓ and $\mathbf{X}$, the differentiation with respect to $\mathbf{X}$ is negligible compared to that with respect to ℓ. The operation calculus of local homogeneity is that derivatives with respect to r_α and r'_α within the averaging operation can be commuted to outside the average such that they become derivatives with respect to ℓ_α and $-\ell_\alpha$.

applied to difference quantities $\partial/\partial r'_\alpha = \partial/\partial \ell_\alpha$ and $\partial/\partial_\alpha = -\partial/\partial \ell_\alpha$, so that

$$\partial_t \langle \Delta n^2 \rangle + \frac{\partial}{\partial \ell_\alpha} \langle \Delta u_\alpha \Delta n^2 \rangle + \langle u_\alpha \left(\partial_\alpha + \partial'_\alpha \right) \Delta n^2 \rangle = 2 \langle \Delta n \Delta f \rangle \tag{3.11}$$

Equation (3.11) can be simplified by assuming that the system, for long times, reaches a statistically stationary state, so that the time derivative is put to zero, and that the system is isotropic. This last assumption can be worked out by assuming that quantities depend solely on r and not on θ, so that using the radial coordinate as α, and $r' = r + \ell$, we get

$$\frac{1}{\ell} \frac{\partial}{\partial \ell} \left[\ell \langle \Delta u_r \Delta n^2 \rangle \right] + \langle u_\alpha \left(\partial_\alpha + \partial'_\alpha \right) \Delta n^2 \rangle = 2 \langle \Delta n \Delta f \rangle$$

This equation can be formally integrated, finally obtaining an equation for the third–order mixed correlation function:

$$\langle \Delta u_r \Delta n^2 \rangle = -\frac{1}{\ell} \int_0^\ell dy \langle u_r \left[\frac{\partial}{\partial r} + \frac{\partial}{\partial r'} \right] \Delta n^2 \rangle y + \frac{2}{\ell} \int_0^\ell dy \langle \Delta n \Delta f \rangle y \tag{3.12}$$

The first term on the r.h.s. is due to large scale non homogeneity of the charge density, while the second term is due to correlations between the forcing and the charge density. This correlation is assured by the fact that the charge density is absorbed at the external wall and it is injected through the forcing term inside the inner annulus. Of course, this means that our system is intrinsically inhomogeneous, giving rise to inhomogeneous bursty turbulence. Intermittency, in form of bursts, means that turbulence is inhomogeneous, and in some sense this term plays the role of a dissipative term. It is interesting to compare our equations with the similar equations known as the Yaglom–Obukov equations for a passive scalar, for example the temperature T, within a turbulence [146]. The equation that describe this physical system is

$$\partial_t T + u_\alpha \partial_\alpha T = \kappa \partial_\alpha^2 T \tag{3.13}$$

where κ is the thermal diffusivity and the second term is a dissipative term. Note that the difference with our case is the fact that the velocity field *is not an independent variable*, while in equation (3.13) the velocity field is derived from the Navier–Stokes equation without the back–reaction of the temperature (that is, in fact, assumed as a passive scalar). Another difference is the presence of the dissipation, that is absent in our simulation, and the

presence of forcing. By using the same technique used in deriving equation (3.12), it can be obtained [146] the equation for $\langle \Delta T^2 \rangle$

$$\begin{aligned} \frac{\partial \langle \Delta T^2 \rangle}{\partial t} &+ \frac{\partial}{\partial \ell_\alpha} \langle \Delta u_\alpha \Delta T^2 \rangle = -\frac{4}{3} \frac{\partial}{\partial \ell_\alpha} (\epsilon \ell_\alpha) + \\ &+ 2\kappa \frac{\partial^2}{\partial \ell_\alpha^2} \langle \Delta T^2 \rangle - \langle u_\alpha (\partial_\alpha + \partial'_\alpha) \Delta T^2 \rangle \end{aligned} \tag{3.14}$$

where

$$\epsilon = 3\kappa \langle \left(\frac{\partial T}{\partial x_\parallel} \right)^2 \rangle$$

is the dissipation rate of temperature field, defined positive. In the inertial range of turbulence, where the thermal diffusivity is set to zero, and when the physical system is globally homogeneous, the last two terms on the r.h.s. of equation (3.15) disappear and we get the famous Yaglom–Obukov 4/3–law for the third–order mixed correlations of stationary turbulence. Since the diffusion rate for temperature is definite positive the Yaglom–Obukov relation gives a negative value for the third–order mixed correlation, that implies the existence of a cascade of $\langle \Delta T^2 \rangle$ towards smaller scales. In this case, the independence of the temperature from the forcing term is assumed, because the forcing term is supposed to be active only at the largest scales. In our case we cannot make this assumption because the forcing term, as showed in experiments, is spatially localized so that its power spectrum must be defined over a large number of wave–vectors, namely of possible scales, and any scale separation can exist in our case.

3.4 Numerical simulation of forced bursty turbulence

We performed numerical simulations of the $\mathbf{E} \times \mathbf{B}$ system, using a second–order upwind scheme for space, since the continuity equation has an intrinsic hyperbolic form (see Chap. 2 for more details), and a second–order Runge–Kutta scheme in time. The results have been obtained through a sequence of long time runs, in order to achieve a statistically stationary state of bursty turbulence. For each time step we use a *LU–decomposition technique* [97] to invert the Poisson equation (3.3) and obtain the potential field $\phi(r, \theta, t)$, then we evaluate $\mathbf{u}$ by Eq. (3.4) and compute the field $n(r, \theta, t + \Delta t)$ by Eq. (3.2).

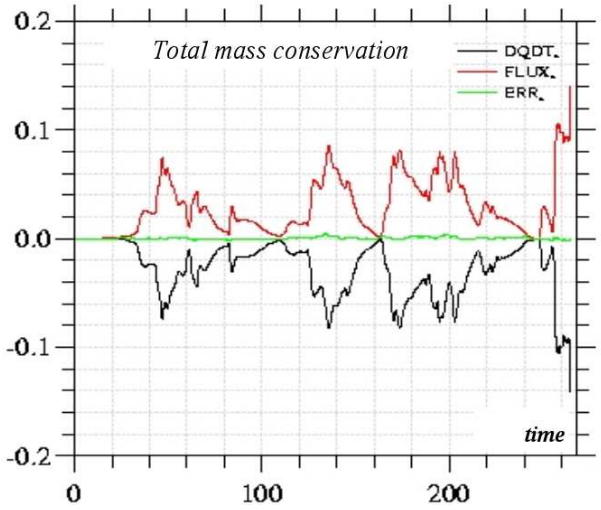

Figure 3.9: We report the value of dQ/dt (black line) and $\oint \Gamma \cdot \hat{r} d\theta$ (red line) [cfr. equation (3.15) in the text]. The numerical error (green line), given by the sum of these two contributions, is 5×10^{-4}.

The simulation needs long CPU time in order to obtain large statistics, so we use parallel computing with MPI directives[4]. The external forcing term $f(r, \theta, t)$ has been constructed as a gaussian profile along the r direction such that $f = 0$ for $r \geq 1/3$ and a superposition of five Fourier modes in θ, with random phases. Finally amplitudes of the external forcing are changed every time to maintain constant the charge difference n within the annulus $r \leq 1/3$. The numerical scheme, in absence of the forcing term in Eq. (3.2), conserves the total charge density $N = n_i + n_e$, namely it satisfies with a good approximation the following equation:

$$\frac{dQ}{dt} + \oint N \left(\mathbf{u} \cdot \frac{\mathbf{r}}{r} \right) d\theta = 0 \tag{3.15}$$

where

$$Q = \int_0^1 r dr \int_0^{2\pi} N(r, \theta, t) d\theta$$

[4]All these simulation are performed at the *High Performance Computing Center* of the *University of Calabria*, Cosenza (Italy), by using the 64–processors *HP Alpha Server Voyager*.

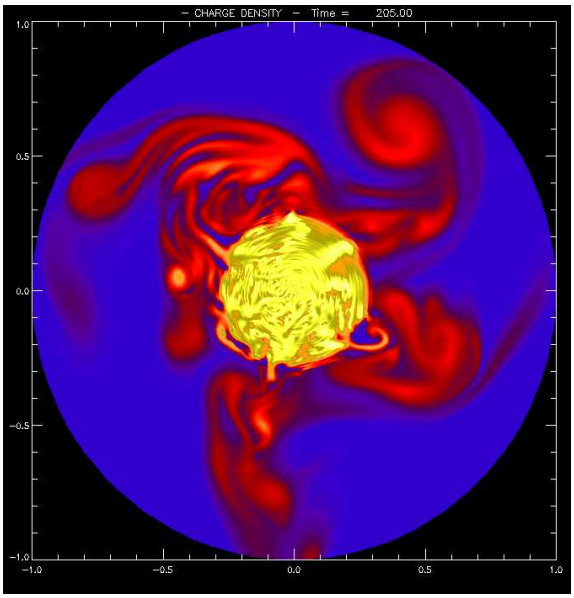

Figure 3.10: $2D$–polar contour of the density n_i at $t = 205$.

is the total charge inside the volume, and the second term represents the flux of charge through the boundary. In Fig. 3.9 we show the quantity dQ/dt, the charge flux and the sum Δ of these two. Analytically, Δ should be vanishing. Numerically, this is not exactly true, due to the truncation error of the numerical scheme. However, it is clear that the total charge is numerically conserved with a numerical error of the order of $\Delta \simeq 5 \times 10^{-4}$.
Figs. 3.10–3.14 show the $2D$–polar contour levels of the charge density at different times of the simulation. It appears the system generates bursts that, on average, are transported towards the external boundary, where they are absorbed by the wall. During the nonlinear dynamics, bursts interact among each other, their shape is distorted and small–scales structures are generated. Bursts have a dipolar structure, as shown in Fig. 3.15. In Fig. 3.16 we report the radial profile of two bursts that can be compared with Figs. 3.6–(a) and Fig. 3.4: also in our case, bursts have a steep front and a long tail.
This is a qualitative picture of the bursty turbulence generated in the system, that is analogous to what have been recently observed in a linear laboratory plasma device.

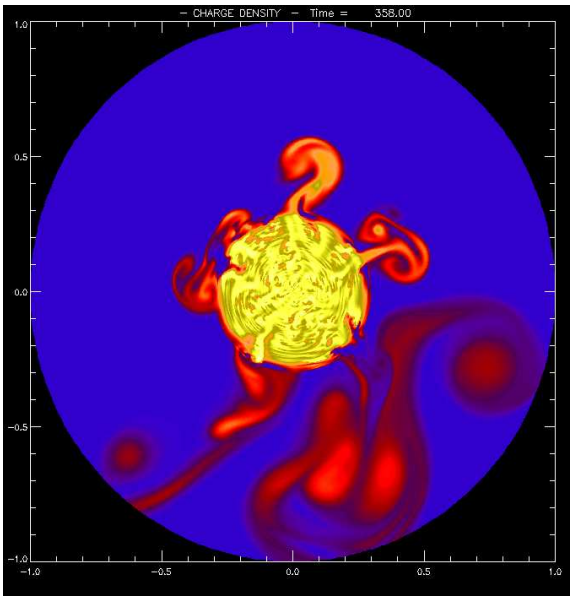

Figure 3.11: $2D$–polar contour of the density n_i at $t = 358$.

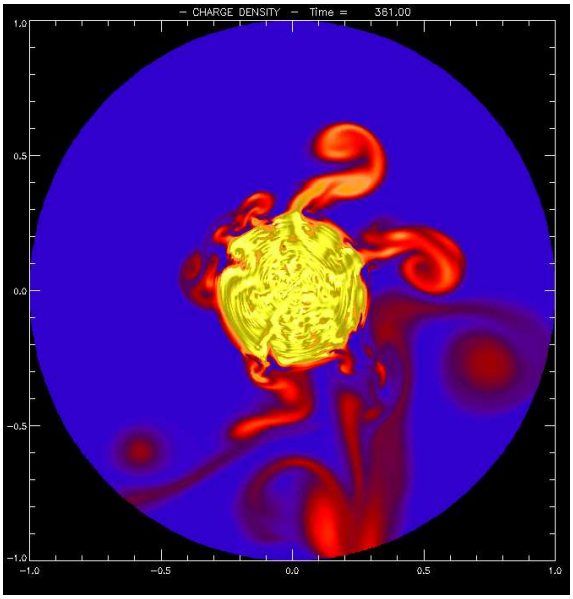

Figure 3.12: $2D$–polar contour of the density n_i at $t = 361$.

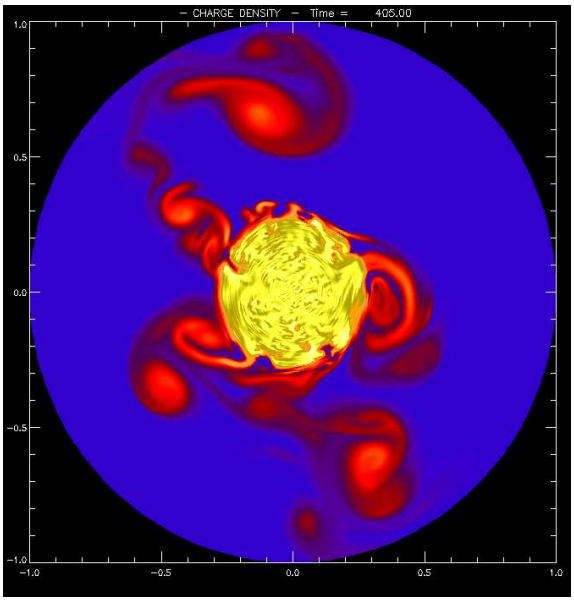

Figure 3.13: $2D$–polar contour of the density n_i at $t = 405$.

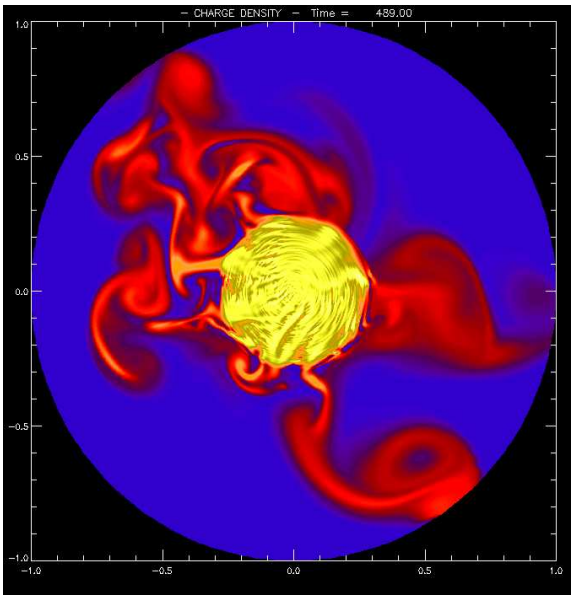

Figure 3.14: $2D$–polar contour of the density n_i at $t = 489$.

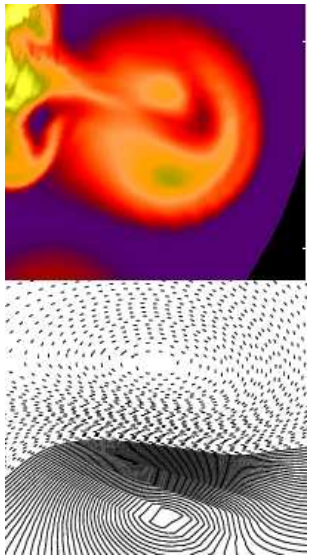

Figure 3.15: 2D images of a single burst (upper panel) and its electrostatic potential ϕ (lower panel). In the lower panel solid line–contour indicate $\phi > 0$, while dotted line–contour for $\phi < 0$. Blobs have a dipolar electrostatic potential as in observations (compare with Fig. 3.6).

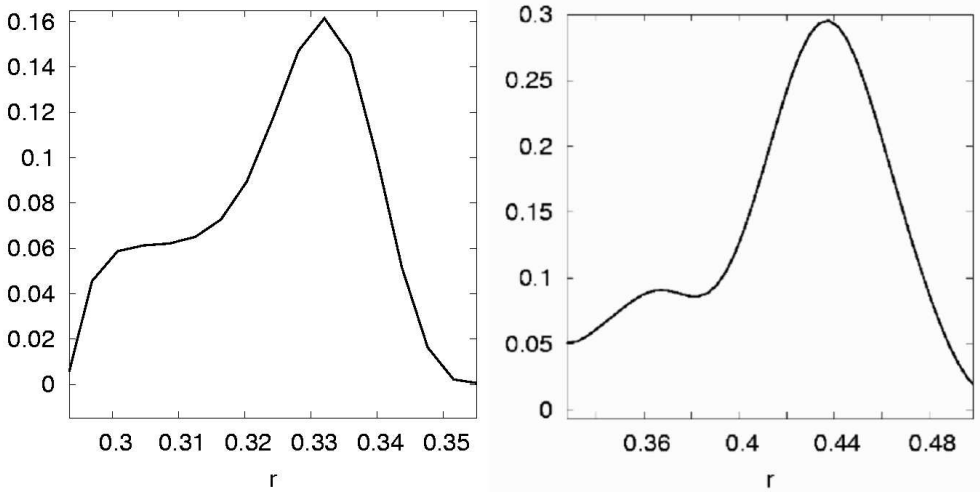

Figure 3.16: The radial profile at $t = 1027$ for two different bursts (left $\theta = \pi/4$, right $\theta = \pi/2$) that are propagating outward from the central region.

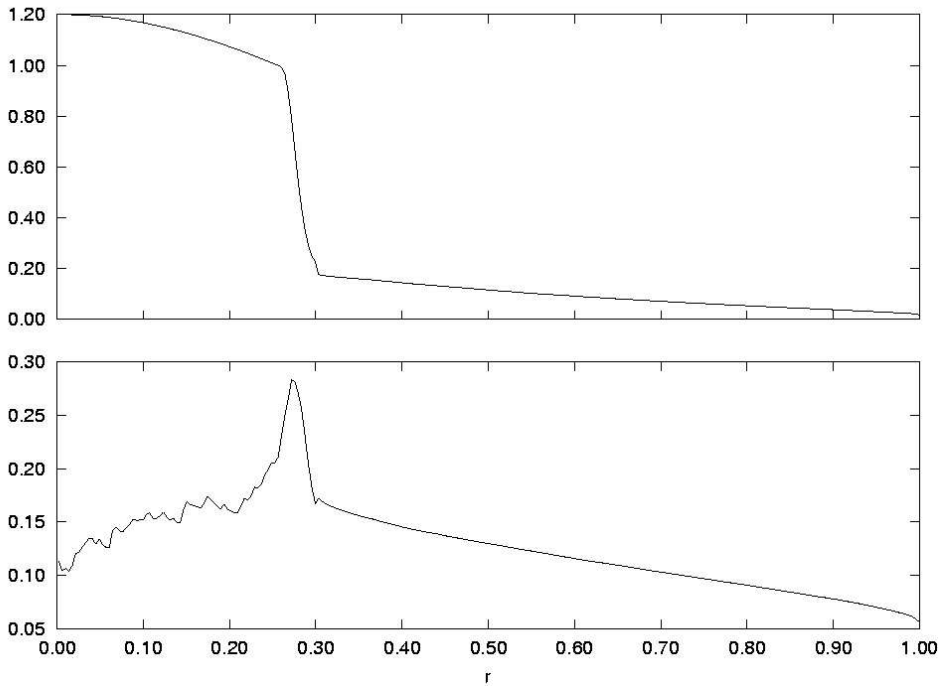

Figure 3.17: The large–scale profile of density $\hat{n}(r)$ (upper panel), and the standard deviation $\sigma(r)$ (lower panel). Note that the $\hat{n}(r)$ profile is similar to the density profile of the LAPD experiment, reported in Fig. 3.5.

3.5 Statistical properties of the "E × B turbulence"

First of all we calculated the large–scale profile of density $\hat{n}(r) = \langle n(r,\theta,t)\rangle$ (brackets mean averaging over time and θ) and of the standard deviation $\sigma(r) = \langle [n(r,\theta,t) - \hat{n}(r)]^2\rangle^{1/2}$. In figures 3.17 we report both profiles. It is evident that, beyond the central region where a strong gradient exists, the radial profile of density is quite smooth, that is the turbulence can be considered as locally homogeneous. This property can be used in the following to investigate the third–order mixed correlations.

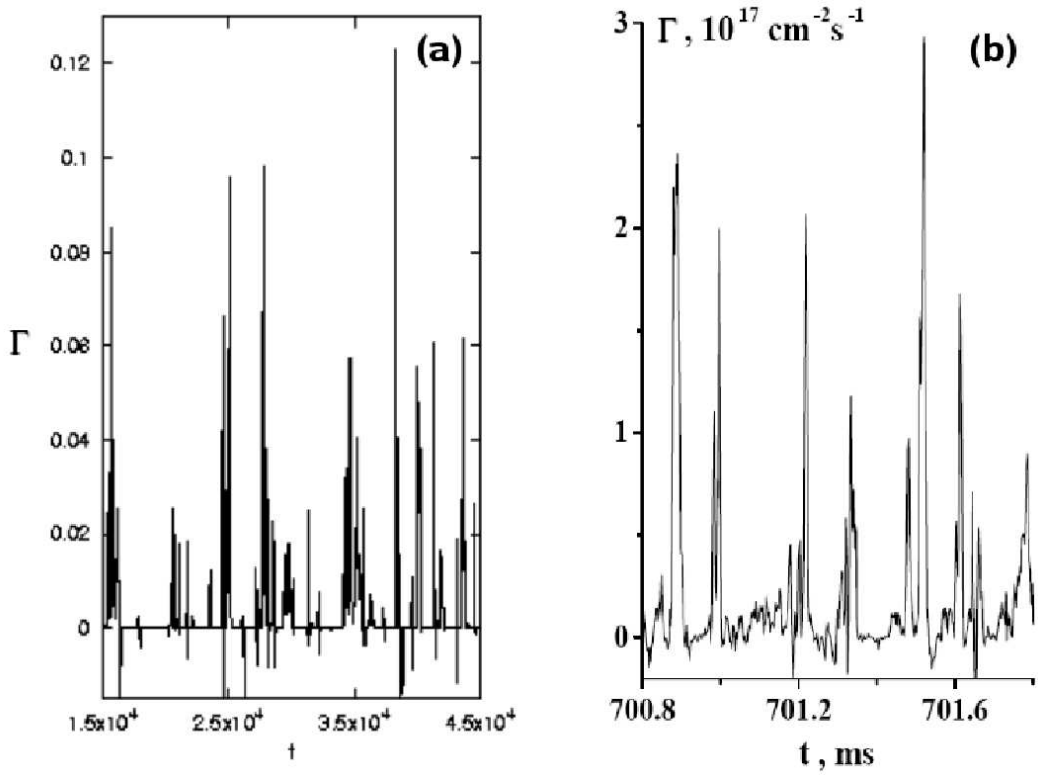

Figure 3.18: The radial flux Γ in a fixed value of the domain ($r = 0.85, \theta = \pi/3$) in the panel (a). In the panel (b) a typical flux signal in experiments [121, 122].

3.5.1 The radial current

Time evolution of the electrostatic radial ion current is a quantity of primary interest in the bursty turbulence. This field is defined as

$$\Gamma(r, \theta, t) = n_i u_r = -n_i (\nabla \phi)_\theta \tag{3.16}$$

A plot of $\Gamma(r, \theta, t)$ as a function of time for $r = 0.85$ and $\theta = \pi/3$ is shown in Fig. 3.18–(a). For comparison we show in the panel (b) of the same figure a typical flux signal taken near the edge of a tokamak device [121, 122]. Strong radial bursts appear for all values of r and θ. Of course the $\mathbf{E} \times \mathbf{B}$–direction is privileged, so that the current flowing towards the wall is statistically favored, as it can be seen in Fig. 3.19, where we report the PDF of Γ calculated for

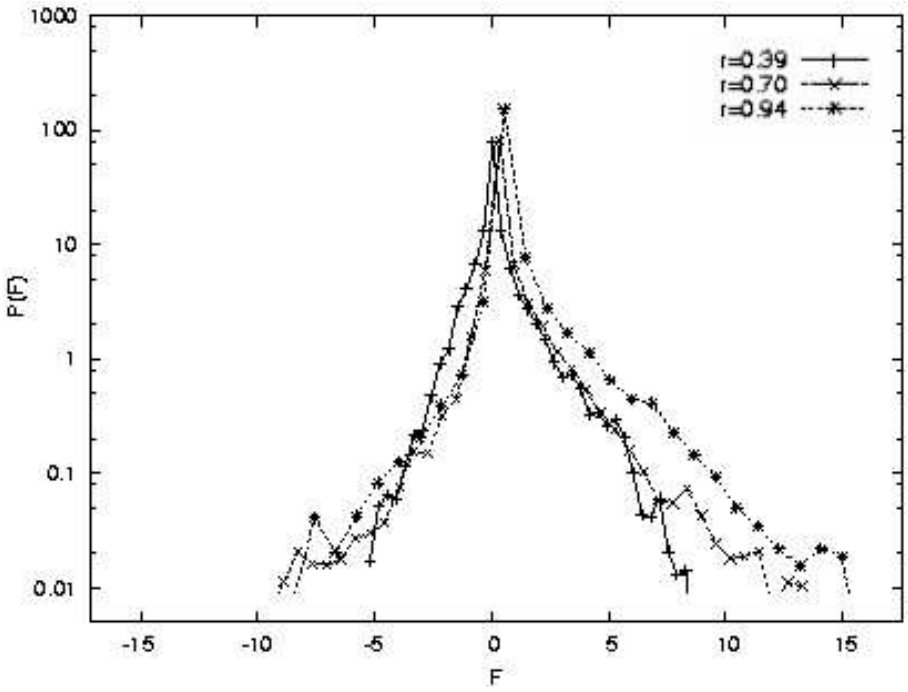

Figure 3.19: PDF of radial flux at three different radial locations.

different r and θ. While the dynamics seems to be statistically independent on θ, there is a dependence on r, namely the negative part of the current flux calculated near the center of the cylinder is enhanced with respect to the flux calculated near the wall.

3.5.2 Statistics of the bursts energy, waiting times and duration times

We analyzed statistically the sequence of bursts observed, and in particular we investigate quantities of physical relevance as the total energy associated to different bursts (*bursts energy*), the duration of bursts (*waiting time*) and the time differences between two consecutive bursts (*time duration*). Since statistics does not have an angular dependence, we integrate in the θ–direction. These quantities are interesting because they can be used as a

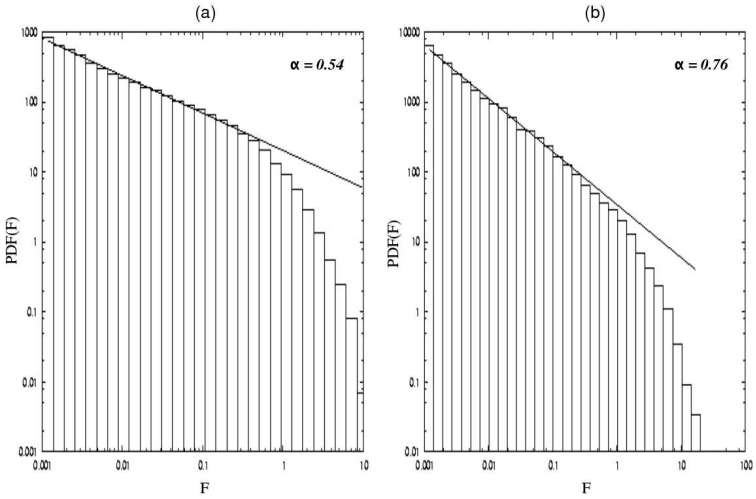

Figure 3.20: PDF of the flux $|\Gamma|$ at $r = 0.39$ (a), and $r = 0.94$ (b) in *log–log* scale. This quantity measures the bursts energy.

rough test to discriminate between some different models of the bursty dynamic [136, 141].
In Fig. 3.20 the absolute value of radial flux, at two different radial distances, namely near the forcing region (Fig. 3.20–(a)) and at the boundaries (Fig. 3.20–(b)), is shown. The analogous for waiting times is reported in Fig. 3.21. Finally we report time duration statistics in Fig. 3.22. As it can be seen, there is a clear power law for bursts energy and waiting time both, with exponents that depend on the radial position. The situation for time duration statistic is more confused and a clear power law does not seem to exist. Power laws are very interesting because they are the signature for the presence of memory among bursts. Of course, this memory is mediated by non linear interactions. In fact charges are injected without any correlation at the center of the numerical domain, and nonlinear interactions are able to build up correlations. Moreover nonlinear interactions act like a kind of self–organization process, by generating localized bursts through a kind of “phase–locking” process [141]. This kind of process is typical of turbulence and also of processes described by Self–Organized Criticality (SOC) [147].

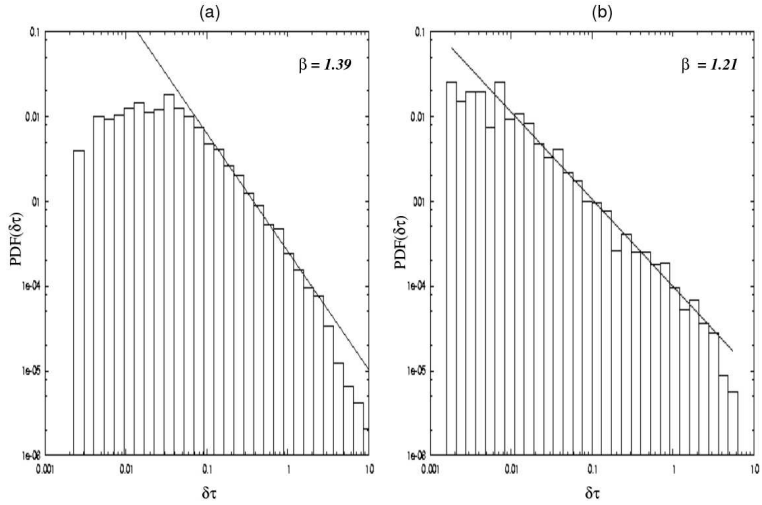

Figure 3.21: PDF of waiting times at $r = 0.39$ (a), and $r = 0.94$ (b), in *log–log* scale.

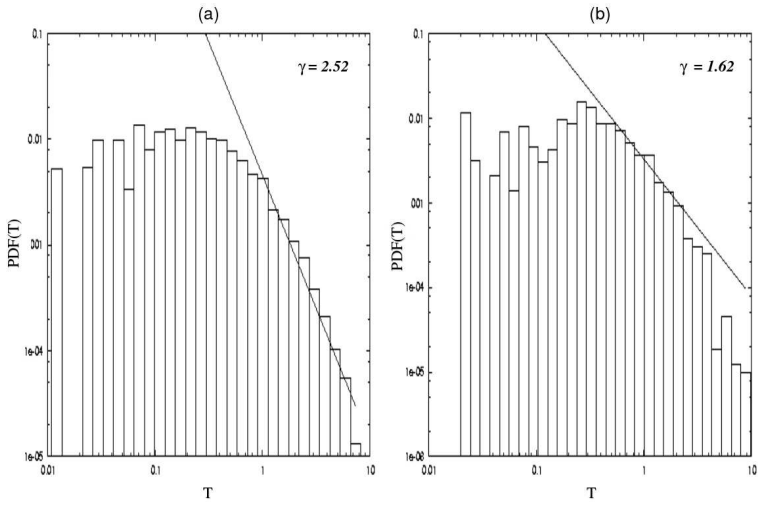

Figure 3.22: PDF of duration times at $r = 0.39$ (a), and $r = 0.94$ (b), in *log–log* scale.

3.5.3 The third–order mixed correlations

We calculated the third–order mixed correlations

$$S_3 \doteq \langle \Delta u_r \Delta n^2 \rangle$$

by averaging over θ and time, at some different radial positions. In figure 3.23 we report the scaling evolution of the quantity $-S_3/\ell$. As we can see, at least when we are quite far away from the point $r = 1/3$ above which the forcing term is set to zero, two main ranges can be recognized, namely a range of small–scales where the third order correlations behave approximately as

$$S_3 \sim -B(r)\ell \log \ell$$

and a range of large–scales where it behaves as

$$S_3 \sim -A(r)\ell$$

where $A(r)$ and $B(r)$ are two constants that depend on the radial position r. These two scaling laws are due to both terms in equation (3.12) respectively. The situation is almost similar to low–Reynolds number turbulence, where a clear inertial range is hardly observed [148]. Following Ref. [148], equation (3.12) can be written in the form

$$S_3 = -\frac{2}{\ell} \int_0^\ell y F(r, y) dy \tag{3.17}$$

where

$$F(r, y) = \frac{1}{2} \left\langle u_r \left[\frac{\partial}{\partial r} + \frac{\partial}{\partial r'} \right] \Delta n^2 \right\rangle - \langle \Delta n \Delta f \rangle$$

represents generalized input rate of turbulence. Assuming the existence of a local maximum of $F(r, y)$ at $y = \ell_m$, we can expand it in terms of the logarithm of the relative distance from ℓ_m [148]:

$$F(r, y) \simeq F(r, \ell_m) - a_1(r) \left[ln \left(\frac{y}{\ell_m} \right) \right]^2 + \cdots + a_{n-1}(r) \left[ln \left(\frac{y}{\ell_m} \right) \right]^n + \ldots \tag{3.18}$$

From dimensional considerations, this expression can be rewritten as:

$$F(r, y) \simeq 2\chi(r) \psi \left(\frac{y}{\ell_m} \right) \tag{3.19}$$

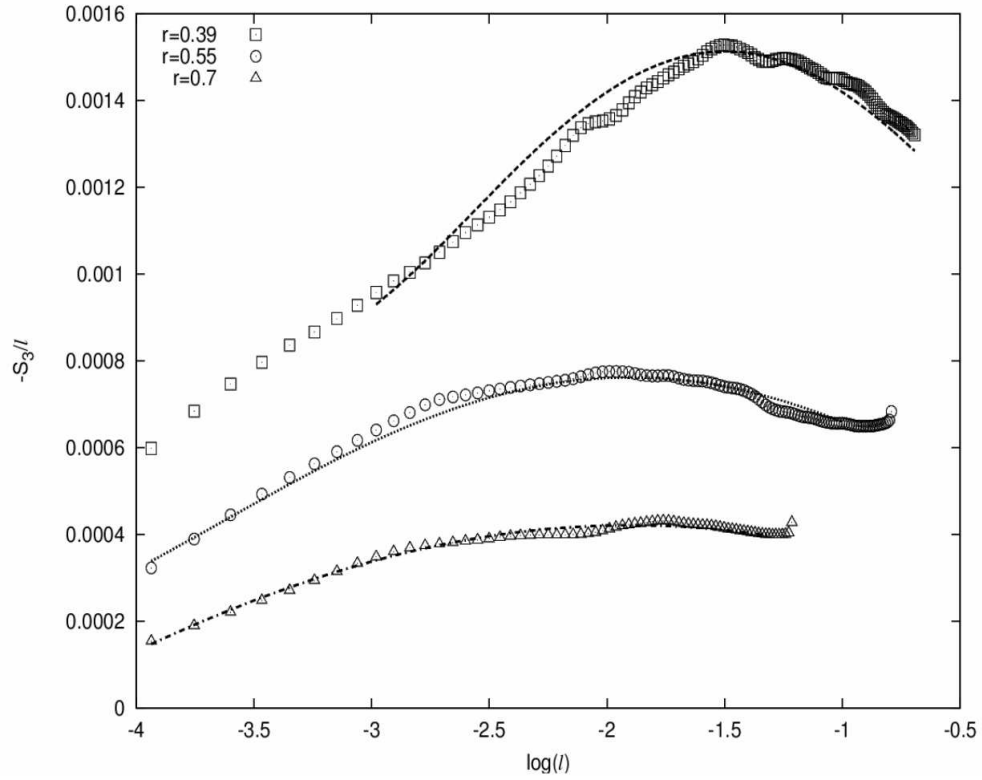

Figure 3.23: Third–order mixed correlations at three different radial positions (symbols) ($r = 0.39$, $r = 0.55$, and $r = 0.70$, as reported on the figure) and the best fit curves representing the Taylor logarithmic development described in Eq. (3.20) (curves).

r	$\chi(r)$	$H_2(r)$	$H_4(r)$
0.39	1.5×10^{-3}	0.26	3.7×10^{-2}
0.55	7.6×10^{-4}	0.17	9.6×10^{-4}
0.70	4.2×10^{-4}	0.17	2.5×10^{-3}

Table 3.1: Parameters of fits reported in Fig. 3.23.

where $\psi(y/\ell_m) = \psi(1)$ within the inertial range. By using Eq. (3.19) in Eq. (3.17), the main contribution to the integral comes from $\psi(1)$ so that

$$S_3 = -\chi\psi(1)\ell$$

and taking into account the *Yaglom law* [146] for d–dimensional turbulence

$$S_3 = -\frac{4}{d}\tilde{\chi}\ell$$

where $\tilde{\chi}$ is the usual constant energy dissipation rate, we obtain $\psi(1) = 2$. When the inertial range has not yet appeared, we can use the logarithmic expansion, substituting Eq. (3.18) in Eq. (3.17), thus obtaining:

$$S_3 \simeq -2\chi(r)\ell \left\{ 1 - H_2(r) \left[ln\left(\frac{\ell}{\ell_m}\right)\right]^2 + H_4(r) \left[ln\left(\frac{\ell}{\ell_m}\right)\right]^4 \right\} \qquad (3.20)$$

Here $\chi(r)$ is a fictitious energy "dissipation" rate, that depends on r due to the large–scale inhomogeneity. Equation 3.20 has been fitted on our numerical results, and the best fit curves are reported in Fig. 3.23. The best–fit parameters are listed in Table 3.1 for the three radial distances. It is evident that Eq. (3.20) is able to reproduce numerical results. When we consider a point far away from $r = 1/3$ the first correction $H_2(r)$ suffices for the best fit. Near $r = 1/3$, where the gradient density is sharp, nonlinear interactions not yet fully developed, so that the correction $H_4(r)$ is more important.

3.6 Conclusions

To summarize, we adopted a very simple model, in a $2D$–polar geometric approximation, of electrostatic turbulence in which the only effect taken into

account is the $\mathbf{E} \times \mathbf{B}$–drift. We numerically investigate nonlinear dynamics of a forced bursty turbulence. During the evolution, many blobs are ejected from the core of the polar domain and propagates radially toward the boundaries. Even if the model is derived from strong approximations, this bursty turbulence has properties similar to that observed in both toroidal and linear devices, namely:

1. intermittent, positively skewed, radial flux near boundaries (far from the forcing region), that indicates outward–propagating bursts;
2. blobs exhibit a dipolar electrostatic potential;
3. the typical radial profile of a blob is a steep front followed by a long tail.

Moreover we investigated turbulence properties by analyzing energy and waiting time statistics of bursts events. We found power laws for both quantities. The presence of power laws, in a randomly forced turbulence, is a clear evidence that this kind of phenomenology is strongly related and characterized by nonlinear interactions, which produce a kind of self–organization and give rise to a dynamics similar to one of SOC models.
By analyzing the third–order mixed correlation, we found that the Yaglom–Obukov law is able to fit our numerical results, identifying the relevance of every contribution (nonlinear transport, inhomogeneity, inertial range, dissipation).
As a general outlook, we think that this simple model can be implemented and, by introducing suitable boundary perturbations, the radially–outward flux of matter can be reduced. Through this, we can suggest a control strategy to increase confinement time inside devices, one of the most important challenge in the problem of thermonuclear energy production. The work towards this aim is still in progress.

Chapter 4

Nonlinear Phenomena in RFP Devices: Multiple–Helicity and Quasi–Single–Helicity States

In the complex picture of the RFP turbulence, in which turbulent fields evolve stochastically over a broad range of modes, sometimes happens that the spectral structure of the magnetic field is dominated by few poloidal and toroidal modes. These states are known as *Quasi–Single–Helicity* states (QSH). At variance to *Multiple–Helicity* (MH) states, where many $m = 1$ poloidal modes with different toroidal numbers n have comparable amplitudes, a QSH state is characterized by a single mode ($m = 1$, $n = n_D$) that dominates the spectrum [149,150]. Results of a wide range of observations on different RFPs (cf., e.g., Ref. [151]) shows that sometimes QSH states spontaneously emerge from a MH background [152, 153] within a RFP discharge, thus generating a MH $\rightarrow$ QSH transition. In general, $n_D > 1$ depends on the aspect ratio of experiments, namely, the minor over the major radius of the toroidal device (see Fig. 1.7). This phenomenon is very interesting in order to understand the problem of the turbulent transport and the disruption of the magnetic confinement during plasma discharges.

The physical mechanism responsible for the occurrence of QSH states has not yet been identified. Some authors [154] conjectured that simple dynamical models should be used to describe the intermittent behaviour, that is a parameterization as a function of dissipative coefficients [154–156].

To describe the appearance of QSH during RFP's discharge, we consider a simplified model of MHD theory. The dynamics of low–frequency plas-

mas described by Magnetohydrodynamics (MHD) is interesting because it represents the first approach to the study of a wide variety of phenomena in laboratory plasmas [14]. In some fusion devices (the RFP configuration is an example) or in the solar corona, where the plasma is embedded in a strong magnetic field B_0, the β parameter (that is, the ratio between the kinetic and magnetic pressure) is low ($\beta \simeq 10^{-1}$ as an order of magnitude estimate). In this situation, dynamics of turbulence is mainly confined to the plane perpendicular to B_0, while Alfvénic fluctuations propagate along the field [14,157–159]. Compressible MHD equations are then approximated [157] by the so–called Reduced Magnetohydrodynamics (RMHD).
With numerical simulation of RMHD equations, using a simplified model obtained from a Galerkin approximation [160], we will show how the nonlinear dynamic of RMHD turbulence, without dissipation, is able to generate a process of *self–organization* similar to an inverse cascade. A single Fourier mode dominates over the whole energy spectrum. This leads to statistically stationary states which are similar to QSH [161]. Our results are roughly in agreement with the emergence of QSH states, both in numerical simulations and real experiments, in RFP plasmas [161].

4.1 Magnetic turbulence in RFP devices

The strong magnetic turbulence in the RFP configuration causes a deformation and a destruction of magnetic surfaces. In a toroidal geometry, fluctuations can be represented as a superimposition of Fourier modes

$$b(r,\theta,\phi) = \sum_{m,n} \hat{b}(r,m,n) e^{i(m\theta+n\phi)} \tag{4.1}$$

where r is the radial coordinate, θ and ϕ are the poloidal and the toroidal angular coordinates respectively, while integers m and n are the associated wavenumbers of the Fourier development [162]. In Fig. 4.1 we report a typical magnetic spectrum, for a fixed value of r and $m = 1$, in which several toroidal modes n are present. Generally the radial position in which measurements are taken is located near the boundaries, where typically, in RFP devices, the magnetic field changes sign (see Fig. 1.8) and a high level of fluctuations develops. These states are known as *Multi–Helicity* states (MH), they produce reconnection of magnetic field lines on the so–called *resonant surfaces* [163]. These surfaces are identified by the relation $q(r) = m/n$,

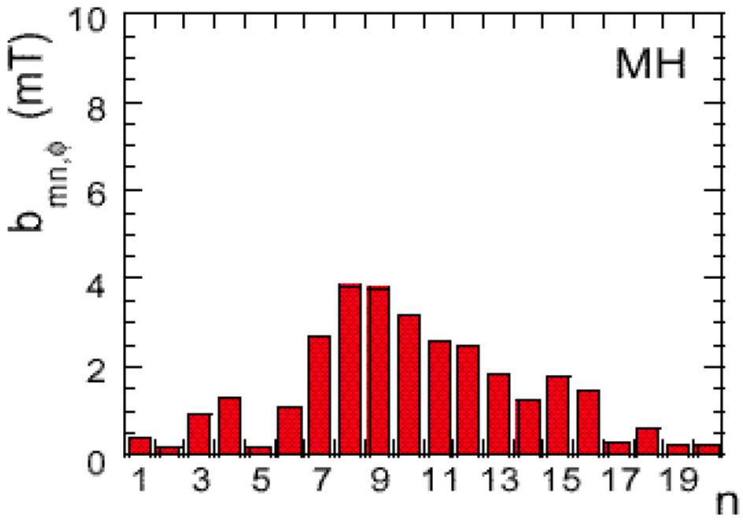

Figure 4.1: An example of toroidal magnetic spectrum, for $m = 1$ at $r/a \simeq 0.85$ (a is the minor radius of the device as sketched in Fig. 1.7) in a highly turbulent case (MH states).

where $q(r)$ is defined by Eq. (1.1). In tokamaks where few modes interact $q > 1$. In the RFP, due to high number of resonant surfaces that nest near the inversion region, $q < 1$. Nonlinear interactions that develop during MH states can lead to a consistent loss of energy, but, on the other hand, they are responsible of the typical magnetic profile of the RFP through a process named *dynamo effect*. The most important mechanism for the inversion of the toroidal magnetic field near the edge is due to the nonlinear evolution of the poloidal wavenumber $m = 1$ (*tearing instability*) [14]. This instability causes a plasma flux in the poloidal direction converting a fraction of B_P (poloidal component) in B_T (toroidal component) in the opposite direction, producing so the inversion of B_T near the edge [164]. This dynamo effect is *laminar* and corresponds to a state in which few modes ($m = 1, n$) are present [165]. In addition to the laminar dynamo effect, a *turbulent dynamo* effect can exist, and it is due to the nonlinear interaction between modes with $m = 0$ and $m = 1$, become resonant near the inversion region. An electric field $\mathbf{E} = \mathbf{V} \times \mathbf{B}$, parallel with respect to B_P, is associated to these fluctuations that sustain the typical RFP configuration at the boundaries.

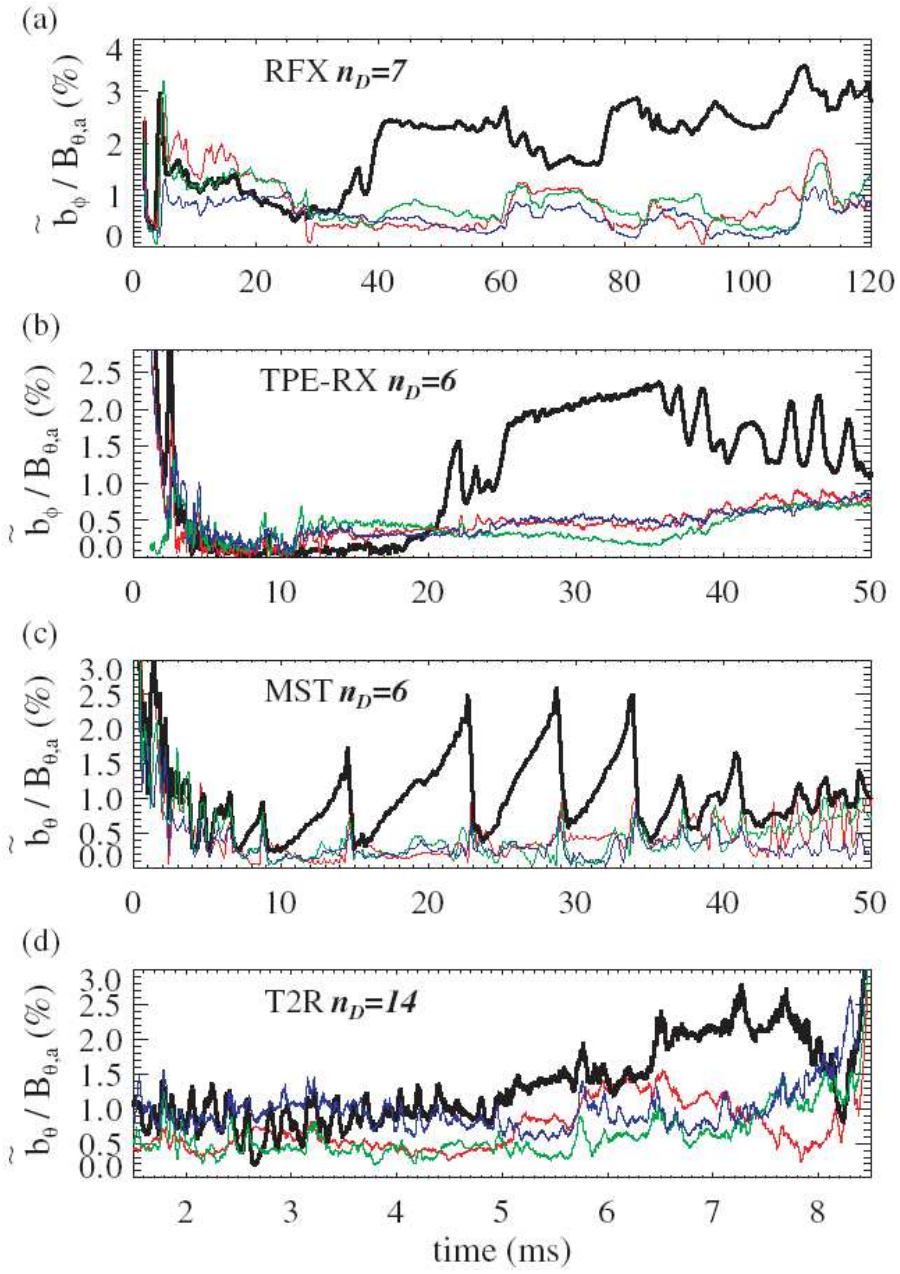

Figure 4.2: Time traces of $(m = 1, n)$ mode amplitudes normalized to the edge poloidal magnetic field for four RFP devices, namely: (a) RFX; (b) TPE–RX; (c) MST; (d) EXTRAP T2R. See Ref. [151] for more details. Magnetic modes are represented with different colors. During plasma discharge the dominant wavenumber n_D (black line) grows and take energy from secondary modes (green, blue and red line). The value of n_D depends on the device.

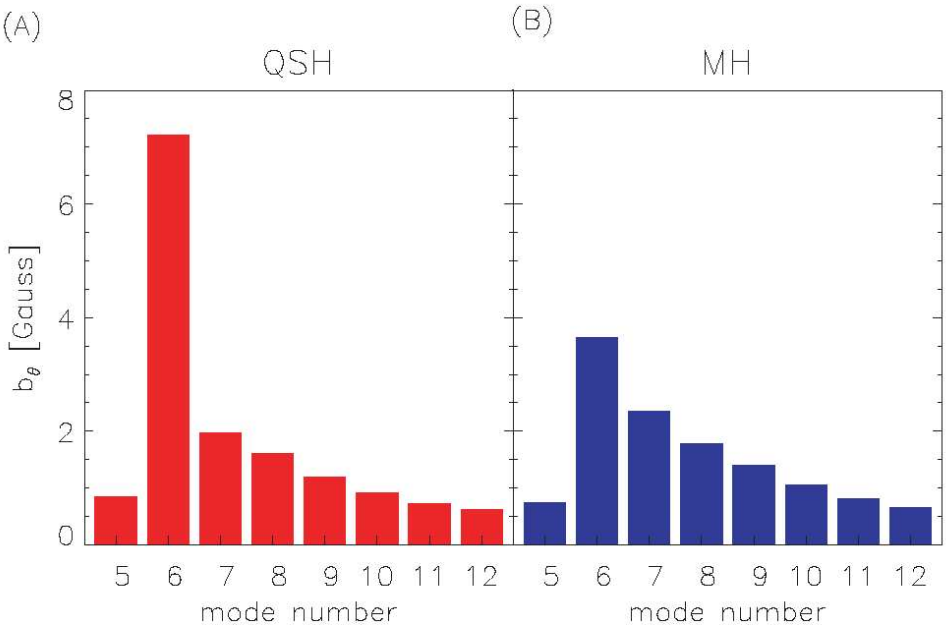

Figure 4.3: Toroidal wave number n spectrum of magnetic fluctuations with the poloidal wavenumber $m = 1$: (A) for QSH and (B) for MH.

4.2 Observations of Quasi–Single–Helicity states

A very interesting phenomenon was recently discovered in a RFP plasma [149–151], that is the spontaneous appearance, during several plasma discharge, of time periods in which the turbulence seems to disappear[1]. This means that MH states *turn off* and give rise to states characterized by few magnetic modes. These states, due to the presence of few modes with $m = 1$ and a fixed value of n, are called Quasi–Single–Helicity states (QSH). They can grow during the discharge in spite of highly turbulent MH states. As shown in Fig. 4.2, during some periods of the order of some milliseconds, a single magnetic mode emerges from the *turbulent sea* and dominates the magnetic spectrum. This dominant wavenumber (n_D) takes energy from other modes, but, after a short period, this state can disappear and decays again in a MH state. In Fig. 4.3 we report a comparison of the toroidal magnetic

[1]QSH states were first observed in the RFX experiment. Consorzio RFX is a research organization promoted by CNR, ENEA, Università di Padova and Acciaierie Venete S.p.A. within the framework of the Euratom – ENEA Association.

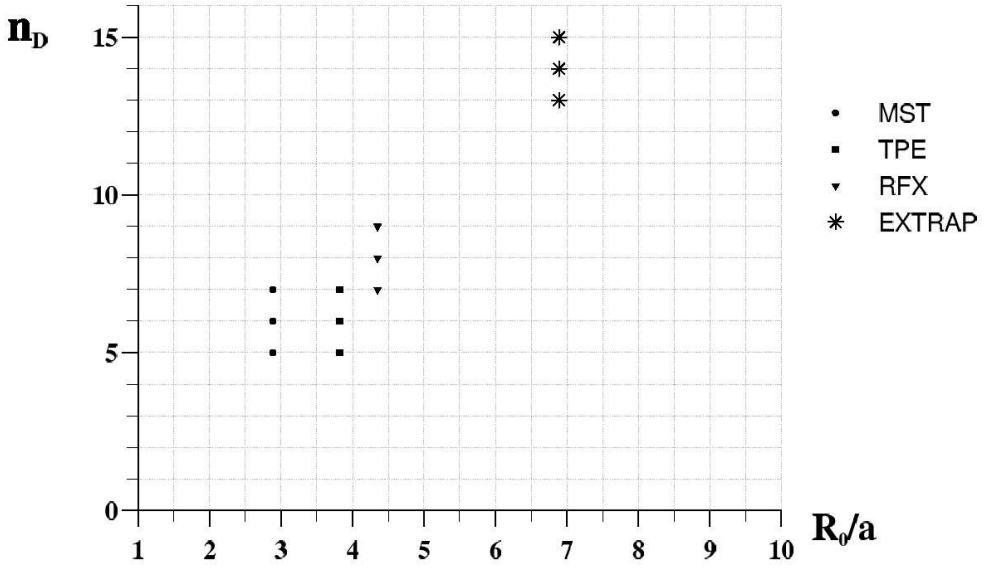

Figure 4.4: Most observed dominant modes $\{n_D\}$ as a function of the aspect ratio. In every RFP device n_D can assume different values, but ranges in a narrow distribution.

spectrum between a QSH and a MH state. Generally, during a QSH state, the dominant mode n_D has an energy that is more or less $2 \div 4$ times the energy of all other modes. This interesting states have been commonly observed in several RFP devices [151, 152, 165, 166].
The number of the most energetic magnetic mode seems to be strongly related to the aspect ratio. This means that every device has a different dominant toroidal mode, that, during the plasma discharge, sometimes emerges from MH states as shown in Fig. 4.2. In Fig. 4.4 we report the most frequent dominant modes n_D observed as a function of R_0/a in different RFP devices. There is a strong dependence on the aspect ratio, *i. e.* the value of n_D increases with R_0/a [151, 165, 166].
Generally in every experiment there is more than one n_D, so, for every RFP, a group of $\{n_D\}$ can be identified. The set of $\{n_D\}$ is chosen on the base of purely observative criteria. By the way, some techniques to identify QSH states exist. To measure how much the magnetic spectrum is *narrow*, let us

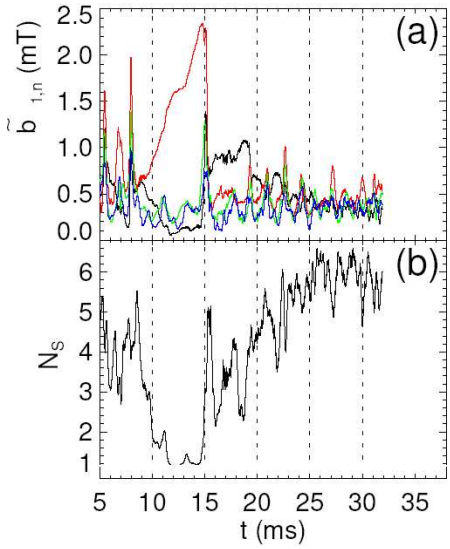

Figure 4.5: Time evolution of (a) magnetic $m = 1$ spectrum and (b) N_S during the appearance of a QSH state. During the period $t \in [10 \div 15]$ ms the dominant mode ($m = 1$, $n_D = 6$) grows and $N_S \to 1$.

introduce the following parameter:

$$N_S(t) = \left[\sum_n \left(\frac{E_b(m = 1, n, t)}{\sum_n E_b(m = 1, n, t)} \right)^2 \right]^{-1} \tag{4.2}$$

where $E_b(m = 1, n, t)$ is the magnetic energy of the Fourier expansion in Eq. (4.1), for a fixed value of r. This parameter represents a measure of the distribution of the magnetic energy in the total spectrum. If many modes are excited then $N_S \to \infty$, while if only a single mode is present (ideal case of a Single Helicity state) $N_S \to 1$. The parameter N_S is known as the *spectral spread* [153, 167]. To better understand the role of the parameter N_S, we show in Fig. 4.5 the comparison between $N_S(t)$ and the magnetic spectrum as a function of time. During a *few modes–state* this parameter assumes lower values.

4.3 The MHD approach

To describe the appearance of QSH during RFP's discharges, we consider a simplified model of the Magnetohydrodynamic theory (MHD). The dynamics of low–frequency plasmas described by MHD is interesting because it represents the first approach to the study of a wide variety of phenomena in both laboratory and astrophysical plasmas [14].
As discussed in Chapter 2, starting from the fluid theory, one can obtain the set of compressible MHD equations [14]. In the incompressible case, assuming for simplicity a constant density, the dimensionless ideal equations that describe low–frequency (lower than the ion cyclotron frequency) of a magneto–fluid are:

$$\frac{\partial \mathbf{v}}{\partial t} = -(\mathbf{v}\cdot\nabla)\mathbf{v} + (\nabla\times\mathbf{b})\times\mathbf{b} - \nabla p \tag{4.3}$$

$$\frac{\partial \mathbf{b}}{\partial t} = \nabla\times(\mathbf{v}\times\mathbf{b}) \tag{4.4}$$

$$\nabla\cdot\mathbf{v} = 0 \tag{4.5}$$

where $\mathbf{v}$ and $\mathbf{b} = \mathbf{B}/\sqrt{4\pi\rho_0}$ represent the dimensionless velocity and the Alfvén velocity field respectively, ρ_0 is the mass density, p the kinetic pressure. By introducing the vector potential $\mathbf{a}$, the $\mathbf{b}$ field, that satisfy $\nabla\cdot\mathbf{b}$, can be obtained through the relation $\mathbf{b} = \nabla\times\mathbf{a}$. Eqs. (4.3)–(4.5) describe the behaviour of an incompressible plasma in the ideal (dissipation–free) case. Ideal MHD has three quadratic constants of motion [14]. Two of them, namely the total energy $E = \langle v^2\rangle + \langle b^2\rangle$ and the cross helicity $H_C = \langle\mathbf{v}\cdot\mathbf{b}\rangle$, are invariant in each configuration (brackets denote ensemble averages). A third topological quadratic invariant depends on the geometry: in three–dimensional MHD configurations the magnetic helicity $H_M = \langle\mathbf{a}\cdot\mathbf{b}\rangle$ is conserved, while the mean–square magnetic potential $A = \langle a^2\rangle$ is conserved in a $2D$ context.

4.4 A simple model: inviscid Reduced Magnetohydrodynamics

When the plasma is embedded in a strong magnetic field B_0, the β parameter (that is, the ratio between the kinetic and the magnetic pressure) is

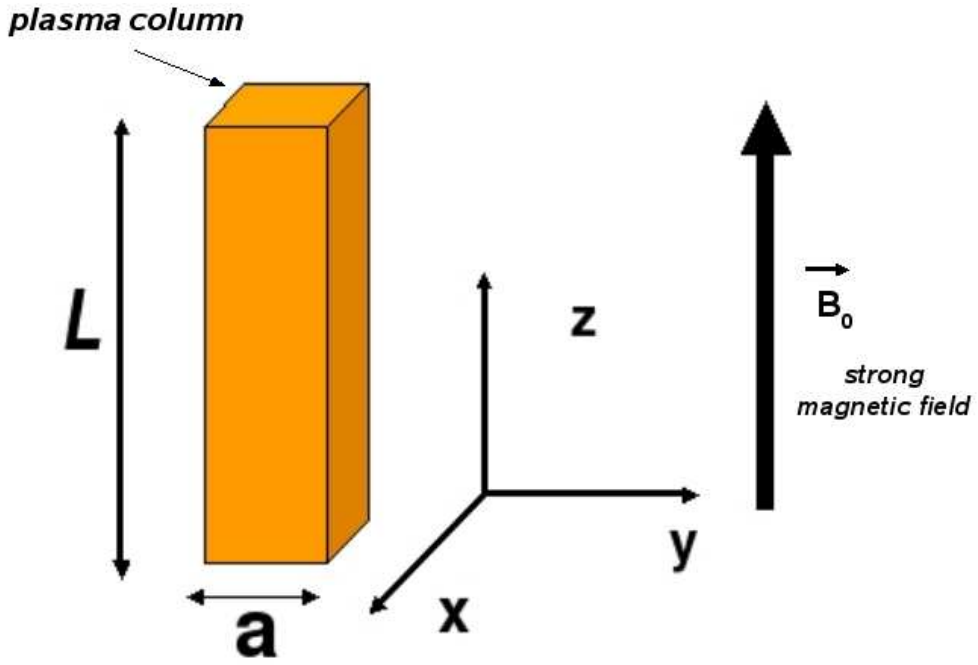

Figure 4.6: A sketch of the geometric approximation for the RMHD model. The small–aspect ratio plasma column ($a/L << 1$) is embedded in a strong axial magnetic field $\mathbf{B}_0$ ($\beta << 1$).

much lower than one. In this situation the dynamics of turbulence is confined to the plane perpendicular to B_0, while Alfvénic fluctuations propagate along the field [14, 157–159]. Compressible MHD equations are then approximated [157–159] by the so–called Reduced Magnetohydrodynamics (RMHD). The simplest model of RMHD approximation deals with a plasma column of low aspect ratio $a/L << 1$ (a and L being, respectively, the basis size and the height of the plasma column), embedded in a strong magnetic field $\mathbf{B}_0 = B_0\ \mathbf{e}_z$ (B_0 is constant and $\mathbf{e}_z$ is the unit vector along the axis of the column). In Fig. 4.6 we shown a sketch of the plasma geometry.
We use Fourier transforms in the transverse $\mathbf{r} = (x, y)$ plane, say, on a $2D$ box of size a, for both velocity

$$\mathbf{v}(\mathbf{r}, z, t) = \sum_{\mathbf{k}} v_{\mathbf{k}}(z, t)\ \mathbf{e}(\mathbf{k}) \exp(i\mathbf{k} \cdot \mathbf{r})$$

and magnetic field

$$\mathbf{b}(\mathbf{r}, z, t) = \sum_{\mathbf{k}} b_{\mathbf{k}}(z, t)\ \mathbf{e}(\mathbf{k}) \exp(i\mathbf{k} \cdot \mathbf{r})$$

fluctuations, where $\mathbf{e}(\mathbf{k})$ is a unit vector perpendicular to $\mathbf{B}_0$. The wave vectors are defined as $\mathbf{k} = (2\pi/a)\mathbf{m}$, where $\mathbf{m} = (m_x, m_y)$ is a couple of integers, and satisfy, due to the solenoidal condition of velocity and magnetic field, $\mathbf{k} \cdot \mathbf{e}(\mathbf{k}) = 0$. After some algebra, ideal RMHD equations can be written in the following dimensionless form:

$$\begin{aligned} \frac{\partial v_{\mathbf{k}}}{\partial t} &= \frac{1}{R_0}\frac{\partial b_{\mathbf{k}}}{\partial z} + \sum_{\mathbf{k}=\mathbf{p}+\mathbf{q}}^{\Delta} C_{\mathbf{k},\mathbf{p},\mathbf{q}}\ (p^2 - q^2)\ (v_{\mathbf{p}} v_{\mathbf{q}} - b_{\mathbf{p}} b_{\mathbf{q}}) \\ \frac{\partial b_{\mathbf{k}}}{\partial t} &= \frac{1}{R_0}\frac{\partial v_{\mathbf{k}}}{\partial z} + \sum_{\mathbf{k}=\mathbf{p}+\mathbf{q}}^{\Delta} C_{\mathbf{k},\mathbf{p},\mathbf{q}}\ k^2\ (b_{\mathbf{p}} v_{\mathbf{q}} - v_{\mathbf{p}} b_{\mathbf{q}}) \end{aligned} \tag{4.6}$$

where $C_{\mathbf{k},\mathbf{p},\mathbf{q}} = (p_x q_y - p_y q_x)/2kpq$ and R_0 represents 2π times the aspect ratio. Fourier coefficients are normalized to $B_0/(4\pi\rho_0)^{1/2}$ (that is, the Alfvén speed), wave vectors to a^{-1}, and times to $a(4\pi\rho_0)^{1/2}/B_0$. The convolution sum is extended over all the infinite number of wave vectors $\mathbf{p}$ and $\mathbf{q}$ which satisfy the triad relation $\mathbf{k} = \mathbf{p} + \mathbf{q}$.
In Eqs. 4.6, if $R_0 \to \infty$ the propagation term along the z–axis disappears and the RMHD system reduces to the 2D–MHD configuration, namely a plane perpendicular to the mean magnetic field $\mathbf{B}_0$. In the incompressible 2D–MHD, quadratic invariants in the Fourier space are:

$$E(t) = \sum_{\mathbf{k}} [|v_{\mathbf{k}}|^2 + |b_{\mathbf{k}}|^2] \tag{4.7}$$

$$H_C(t) = \sum_{\mathbf{k}} Re[v_{\mathbf{k}}\ b^*_{\mathbf{k}}] \tag{4.8}$$

$$A(t) = \sum_{\mathbf{k}} \frac{|b_{\mathbf{k}}|^2}{k^2} \tag{4.9}$$

The "rugged invariants" [168] [Eqs. (4.7)–(4.9)] play a key role because they survive for each finite consistent truncation of wave vectors $(\mathbf{k}, \mathbf{p}, \mathbf{q})$, which satisfy the triad–interaction relation. In other words E, H_C, and A remain invariant for each individual triad of wave vectors $\mathbf{k} = \mathbf{p} + \mathbf{q}$ among the

infinite terms of Eq. (4.6) even when the infinite set of values for $\{\mathbf{k}, \mathbf{p}, \mathbf{q}\}$ is truncated to a finite set. It can be easily realized that in presence of B_0 in the RMHD approximation the third topological invariant is lost: H_M is trivially zero, and even if the nonlinear operator is formally $2D$, since the presence of the Alfvénic transport the square root of the vector potential cannot survive as a constant of motion.

4.4.1 The equilibrium ensemble of 2D–MHD

Turbulence is an out–of–equilibrium process, because an energy cascade is present. However, when the dissipative term is set to zero, the infinite set of equations for the Fourier modes of the fields evolve in time. In this case an asymptotic distribution of fields over the infinite range of wavevectors can be described through a classical *equilibrium ensemble* of statistical mechanics [169].
Information on spectral properties of 2D–MHD can be obtained in terms of the moments of a *statistical distribution* [170, 171]. To get some insight into this phenomenon, let consider now the equilibrium distribution of a 2D–MHD fluid in an inviscid case ($\nu = \mu = 0$). In the *canonical ensemble* [14] the equilibrium distribution is defined by the *Gibbs function*:

$$\rho = \frac{1}{Z} exp(-\alpha E - \epsilon A - \gamma H_C) \tag{4.10}$$

where α, ϵ and γ are Lagrange multipliers, and Z is a normalization quantity. It is found that in the 2D–MHD, as we are going to demonstrate, quite in contrast to the hydrodynamical case, cascade properties do not depend on the geometry (cf., e.g., Ref. [14] and references therein): energy is even peaked at large wave vectors, while an *inverse cascade*[2] leads to the formation of a large–scale magnetic field. Generally, if the distribution function has a gaussian shape like

$$\rho(x) = \frac{1}{Z} \exp\left[-\frac{1}{2} \sum_{i,\ j} A_{ij} x_i x_j\right] \tag{4.11}$$

[2]The direct cascade process in turbulence is the transfer of energy by nonlinear interactions from larger to smaller eddies. The inverse process (inverse cascade) is a back–transfer of energy from smaller to larger scales.

by using gaussian integral properties, it can shown that $\langle x_i x_j \rangle = A_{ij}^{-1}$. Thus, evaluating coefficients of the matrix A_{ij}, one can obtain the equilibrium distribution of any quadratic function $x_i x_j$. Now, by building a phase space with the real and imaginary part of v and b (4–dimensions space), taking into account Eqs. (4.7)–(4.9) , after some algebra, one obtains [14, 172]:

$$E_k(k) = \frac{\alpha + \frac{\beta}{k^2}}{\alpha\left(\alpha + \frac{\beta}{k^2}\right) - \gamma^2} \tag{4.12}$$

$$E_b(k) = \frac{\alpha}{\alpha\left(\alpha + \frac{\beta}{k^2}\right) - \gamma^2} \tag{4.13}$$

$$H_c(k) = -\frac{\frac{\alpha}{k^2}}{\alpha\left(\alpha + \frac{\beta}{k^2}\right) - \gamma^2} \tag{4.14}$$

and

$$A(k) = -\frac{\frac{\gamma}{2}}{\alpha\left(\alpha + \frac{\beta}{k^2}\right) - \gamma^2} \tag{4.15}$$

From Eq. (4.15), it is clear that the conservation of A implies concentration of energy at small k vectors. The effect of addensation of $E_b(k)$ at large scales is the effect of an *inverse cascade* of A with respect to the total energy E. Moreover, by using Eq. (4.13) and (4.12) one can obtain:

$$E_b(k) - E_k(k) \simeq \frac{\beta}{k^2} \tag{4.16}$$

This last equation means that there is an equipartition of energy at larger k–vectors. The equipartition of kinetic and magnetic energy at small–scales is commonly observed in several laboratory and space plasmas [13, 173]. What happens when the third invariant is lost, that is not so clear. Even if in principle the inverse cascade cannot take place, some numerical results concerning the *inviscid equations* are needed to explore this situation. Presumably, there should be no dominance of magnetic energy at large scales since $\langle v^2 \rangle - \langle b^2 \rangle \sim \epsilon$ [14]. An equipartition between kinetic and magnetic energy should be the result of the dynamics.

4.5 The numerical technique

We consider a particular class of solutions of Eq. (4.6) represented, for each value of z (mean magnetic field direction), by a finite number of Fourier

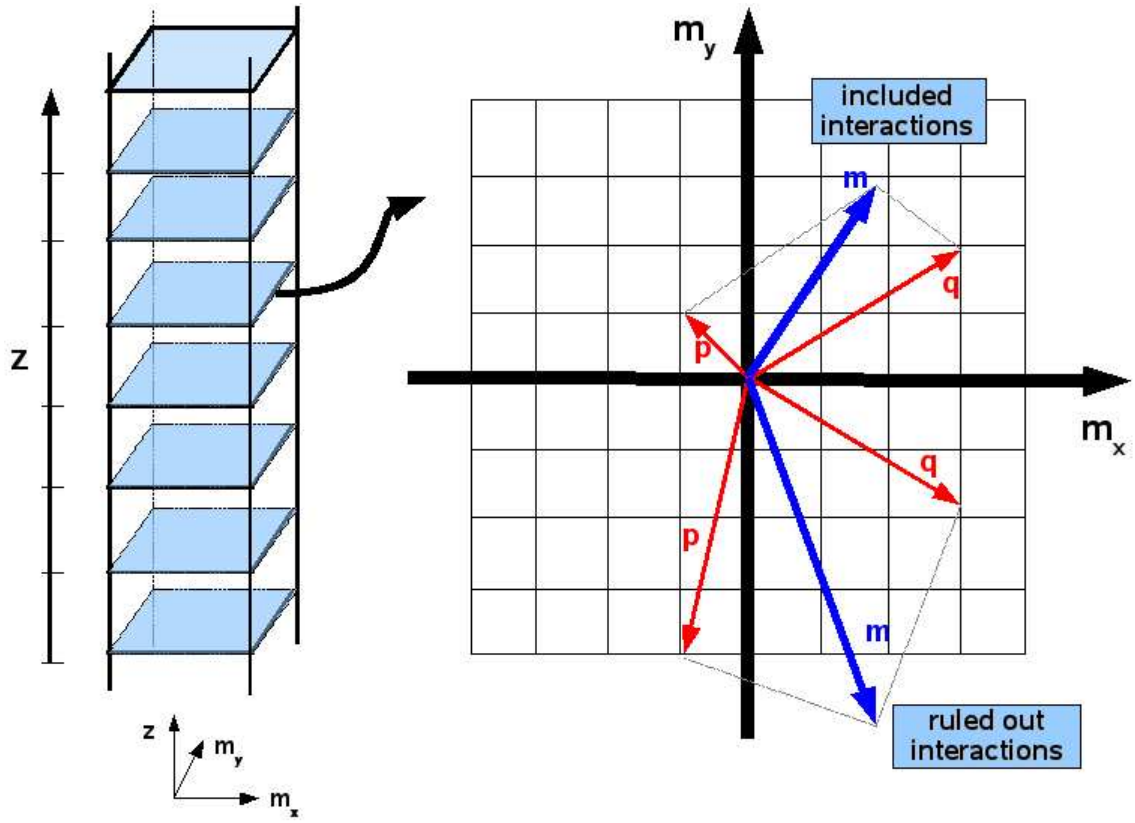

Figure 4.7: A sketch of the numerical technique. On the left the plasma column of Fig. 4.6 in the $\mathbf{m}$–z space, we divide the z axis in N_z planes. On the right is represented a single plane z_i. In this plane we adopt the Galerkin truncation to choose only interactions that lie in a Fourier two–dimensional space with $-N \leq m_x \leq N$ and $-N \leq m_y \leq N$.

modes (Galerkin approximation). Without losing generality, we put $a = 2\pi$. Then we retain only the Fourier components of both $\mathbf{v_k}(z,t)$ and $\mathbf{b_k}(z,t)$, for which $\mathbf{m}$ lies on a square of size $(2N+1)^2$; that is, $-N \leq m_x \leq N$ and $-N \leq m_y \leq N$. Eq. (4.6) is filtered out; that is, we drop all nonlinear interaction terms which involve at least one wave vector outside the above range. In this way, we restrict the infinite sum on the right–hand side of Eq. (4.6) to a sum over a finite number of terms. In Fig. 4.7 the numerical procedure of Galerkin truncation is sketched. This procedure can be used in two different ways: (i) as a filter for large–eddy simulations [11]; (ii) as a definition of a class of low–order dynamical models, where nonlinear interactions are restricted to N modes [15, 168, 174]. In our case, since we would like to observe phenomena relative to the largest scales of the flow, we use the filter to investigate the nonlinear evolution of a truncated model. The model is refined by dividing the z axis into N_z different planes.
Numerical integrations have been carried out using a second–order Runge–Kutta scheme in time. The transport term is solved through a second order centered finite difference scheme for $\partial/\partial z$, with periodic boundary conditions. We use parallel computing with MPI directives[3]

4.6 The appearance of QSH states in RMHD

Initial values of the real and imaginary parts of the fields are randomly chosen, uniformly distributed in the range (-1, 1), over all Fourier modes and for all values of z. The time step used in the computation is 5×10^{-4} eddy–turnover times. This assures, as checked "a posteriori", that the two rugged invariants are conserved up to eight significant digits. Here we report results relative to $N = 16$ and $N_z = 512$. In Fig. 4.8, the time evolution of the three invariants is shown. While both E and H_C remain constant, the square of the vector potential is an oscillating quantity. However, from our simulations we found that these oscillations are relatively narrow, namely, $|A(t) - A(0)|/A(0) \leq 0.02$; that is, $A(t)$ is not exactly conserved, but it looks to be quasi–invariant.
To see what this means on the rearrangement of energy over different modes we evaluate the spectral magnetic energy $E^{(M)}_{m,n}(t)$ in the poloidal–toroidal wavenumber plane (m,n). This has been obtained by performing a $1D$

[3]All these simulation are performed at the *Dipartimento di Fisica* of the *University of Calabria*, Cosenza (Italy), by using the 16–processors *Digital Alpha Server Telesio*.

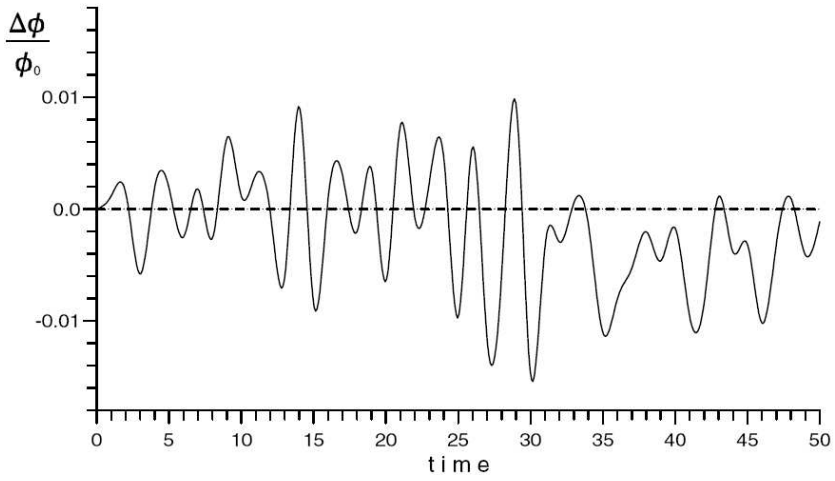

Figure 4.8: The time evolution of $\Delta\phi/\phi_0$ is reported. Here ϕ_0 represents the initial value of a given invariant (say, energy, cross helicity, or the square of the vector potential). While energy and cross helicity are constant (dotted lines at $\Delta\phi = 0$), the square of the vector potential results to be an oscillating quantity, even if the oscillations have a small relative amplitude, $|\Delta\phi/\phi_0| \leq 0.02$.

Fourier transform along the z axis on $b_{\mathbf{k}}(z,t)$, thus recovering the coefficients $b_{\mathbf{k},k_z}(t)$ ($k_z = 2\pi n/L$ is the wavevector in the parallel z direction). Then $E^{(M)}_{m,n}(t)$ have been obtained as averages of $|b_{\mathbf{k},k_z}(t)|^2$ over shells of unitary amplitude centered on $m = \sqrt{m_x^2 + m_y^2}$. From Fig. 4.9 we see the presence of a kind of *self–organization* of RMHD turbulence: at initial time $t = 0$, modes are randomly spreaded over the entire plane (m, n), while, as time goes on ($t = 50$ in our example), energy is concentrated only over a few modes at large scales. In particular, the mode $(m = 1, n = n_0)$ dominates over all other modes. In Fig. 4.10 the time behaviour of $E_b(m = 1, n, t)$, for different wavenumbers n, is shown.
However, the process just described as a redistribution of energy among the modes is not an inverse cascade process, rather it is more like a kind of self–organization for RMHD turbulence. Turbulence, strongly influenced by the $2D$ character of the nonlinear term, self–organizes in the transverse plane to select the mode $m = 1$. Moreover, to understand the dominance of a single n–wavenumber, let us consider the case where both $v_{\mathbf{k},kz}(t)$ and $b_{\mathbf{k},kz}(t)$ are proportional to

$$\exp\left[i(\mathbf{k}\cdot\mathbf{C_A} + k_z\ B_0)t\right]$$

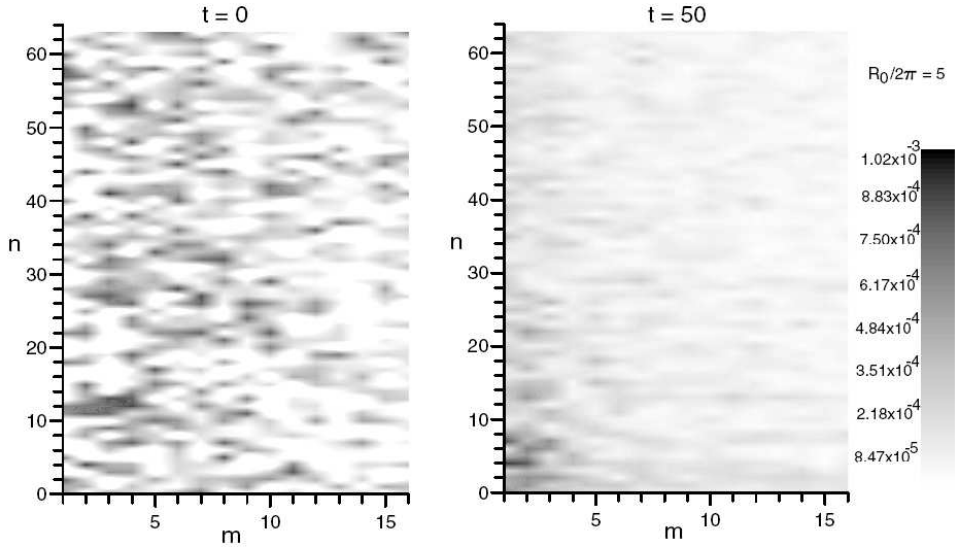

Figure 4.9: The magnetic energy spectrum $E^{(M)}_{m,n}(t)$ is reported on the plane (m, n) for two different times, namely, $t = 0$ (left panel) and $t = 50$ (right panel), for the RMHD case when the aspect ratio is $R_0/2\pi = 5$. The kinetic energy spectrum $E^{(K)}_{m,n}(t)$ displays the same kind of structure.

where $\mathbf{C_A}$ is the largest–scale Alfvén speed in the transverse plane. Using this ansatz in Eq. (4.6), we can realize that the nonlinear term is non oscillating, only when the condition $|\mathbf{k}|C_A/B_0 \sim k_z/R_0$ is fulfilled. In fact a resonance process appears when this situation is verified. This means that once self–organization starts on the transverse plane, i.e., when a mode $m = 1$ is generated, a single $\mathbf{B}_0$ parallel wavevector is selected with wavenumber $n_0 > 1$ proportional to the aspect ratio, say:

$$n_0 \sim (R_0/2\pi) \cdot (C_A/B_0) \tag{4.17}$$

In Fig. 4.11 we report magnetic spectra of modes with $m = 1$ for different values of n, where it is shown that a dominating value n_0 (or a narrow band of values $n \lesssim 3$) is effectively selected. As we show in the right panel of Fig. 4.11, the value of n_0 depends on the aspect ratio used in the computation. When the number of modes N is varied, we find no fundamental differences with the above results. For example, both $N = 8$ and $N = 16$ give $n_0 = 4$ for $R_0/2\pi = 5$, while $n_0 = 3$ for $N = 4$. To what extend a single mode is selected by the nonlinear dynamics can be investigated by defining, in analogous way,

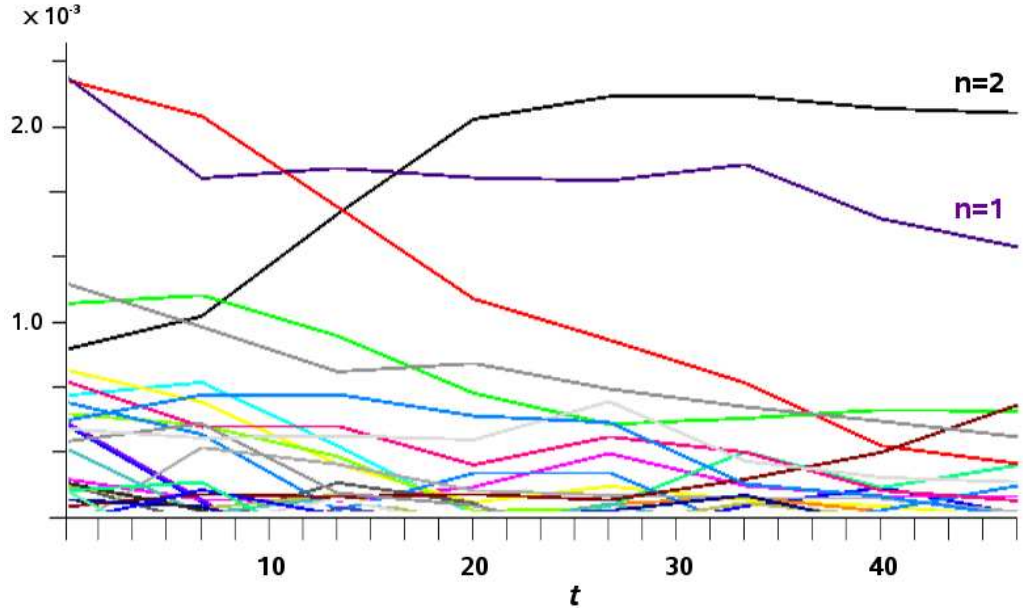

Figure 4.10: Time traces of $E_b(m = 1, n, t)$, for different n. The black line represents the most energetic mode, in this case $n_D = 2$.

the spectral spread parameter N_S of Eq. (4.2) [153]. As the $m = 1$ modes toroidal spectrum becomes poorer, N_S decreases. A spectrum with $N_S = 1$ is a pure single helicity spectrum, but this is a condition never realized up to now in experiments. In Fig. 4.12 we report both the time evolution of N_S and the values of the spectral spread for different values of the aspect ratio. It can be found that N_S decreases with time, which means that a state with a single dominant mode is reached. Moreover, an asymptotic N_S value increases with the aspect ratio $N_S \sim R_0/2\pi$. When we vary the number of modes N, we find a little dependence, namely the larger N is, the more the QSH states become evident. For example, at time $t = 50$ for $N = 4$, we get $N_S \simeq 13.7$, while $N_S \simeq 12.2$ and $N_S \simeq 10.8$, respectively, for $N = 8$ and $N = 16$. The state $(m = 1, n_0)$ selected by the self–organization is surprisingly similar, even quantitatively, to what has been observed as a QSH state in the RFP dynamics. In Fig. 4.12 (right panel), we superposed the values we obtained for n_0, with the values of the dominating toroidal mode observed, within a narrow band of values, both in real experiments and numerical simulations. The agreement is evident. In the same way, in

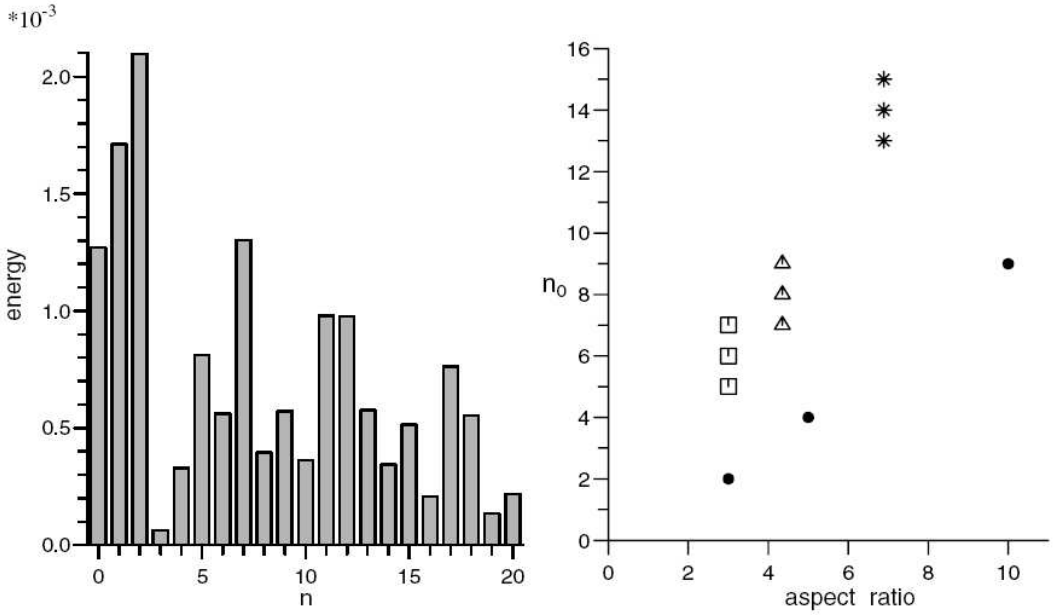

Figure 4.11: In the left panel we report the magnetic energy spectra of modes with $m = 1$, as a function of the poloidal wavenumber n for $R_0/2\pi = 3$ for a single simulation. In the right panel we report the dominant mode n_0, averaged over some simulations made with different initial values of the fields, as a function of the aspect ratio $R_0/2\pi$. Data from our model (black circles) are superimposed to data of three different experiments, namely, the Madison Symmetric Torus (MST, squares), reversed field experiment (RFX, up–pointing triangles), and EXTRAP–T2R (stars) (cf. Refs. [149–152, 166]). The discrepancy between the values of n_0 we found and those found in experiments should be due to geometrical factors which are absent in our model. By the way, as real experiments, the dominant wavenumber increase with the aspect ratio.

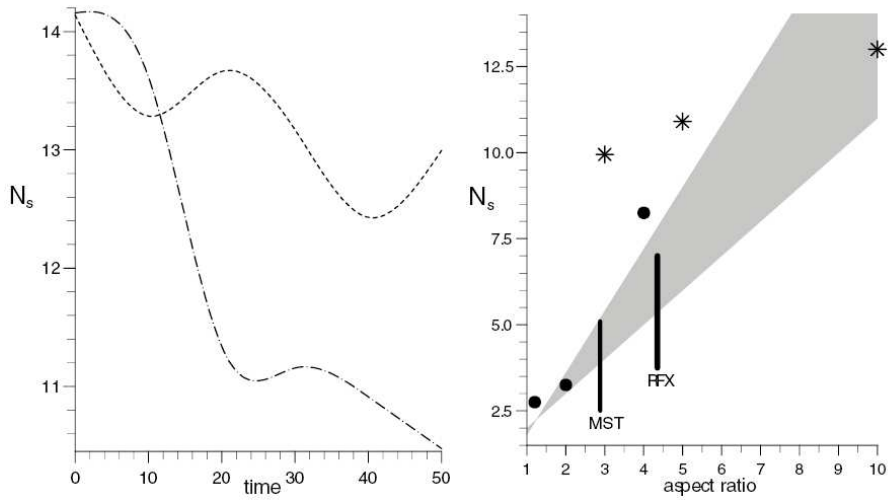

Figure 4.12: In the left panel, we report the time evolution of the spectral spread N_S for simulations performed with two different aspect ratios, namely, $R_0/2\pi = 5$ (dot–dashed line) and $R_0/2\pi = 10$ (dashed line), for a single simulation. In the right panel, we report the spectral spread, averaged over some simulations made with different initial values of the fields, as a function of the aspect ratio $R_0/2\pi$. Data from our model are represented as stars. Black dots represent data from different numerical simulations [151, 166], while the gray triangular band represents the range of results found in [153]. Typical experimental ranges from both RFX and MST devices (vertical bars) are also reported (cf. Refs. [151, 152, 166].

the right panel of Fig. 4.12, we superposed the averaged values of N_S as a function of the aspect ratio, with the values, or the range of values, observed for N_S both in real experiments and numerical simulations. Even in this case the agreement with RFP experiments [6] and numerical simulations is evident. The right panels of Figs. 4.11 and 4.12 represent average values obtained through some different simulations with different initial conditions, while the left panels of the same figures represent a single realization. We would also like to report the fact that the spectral kinetic energy $E^{(K)}_{m,n}(t)$, obtained in the same way as described above through averages of $|v_{\mathbf{k},k_z}(t)|^2$, shows exactly the same self–organizing behaviour. The analogous QSH state has been observed in experiments in RFP devices and reported recently in the literature [175].

4.7 Conclusions

We conjecture that the process of self–organization we identified should be one of the basic features which is at the heart of the experimental evidences of QSH states ($m = 1, n_0$) in RFP turbulent dynamics. In fact, as we showed above, the statistically stationary states we obtained are analogous to QSH observed in RFP experiments and numerical simulations. Even if it seems remarkable that, using a very crude model, we find agreement with real experiments and more complex numerical simulations, we actually use an inviscid model, and comparisons with real experiments or numerical simulations must be taken with care. In fact, both numerical simulations and experiments are intrinsically dissipative. In our case, dissipative terms, typically proportional to ξk^2 (ξ is a dissipative coefficient), can be added to the Eq. (4.6). This leads to a dissipation of the higher wavevectors. As a result the self–organization process, which leads to the dominance of the $m = 1$ mode, appears to be more evident: in presence of dissipative terms, a "clean" $m = 1$ mode quickly emerges from our numerical computation. Actually, the transitions $MH \rightarrow QSH$ and vice–versa have been interpreted [154] as the result of a bifurcation in the phase space of the RFP dynamics, having the Hartman number $H \propto (\eta\nu)^{-1/2}$ as the control parameter (η and ν being, respectively, the inverse Lundquist number and the inverse magnetic Reynolds number). A transition region when the parameter H is set equal to a critical value H_{crit} in the range $2000 \lesssim H_{crit} \lesssim 3000$ has been evidenced in some numerical simulations [154, 156]. In this region the dynamics of the system

has been interpreted as a kind of temporal intermittency alternating laminar phases (QSH states) to chaotic phases (MH states). The quantitative comparison of our inviscid results with both numerical simulations and experiments must be seen simply as evidences for a different point of view, say, that the occurrence of QSH states should be simply the results of a genuine nonlinear self–organization process of MHD turbulence. We conjecture that dissipative effects eventually become necessary in the destruction of the QSH state, rather than in their birth. In fact, as the growth of the magnetic island at large scales reaches its final state, it could be destroyed through dissipative processes related to coalescence of magnetic islands and annihilation at magnetic X points [14, 176].

Conclusions

We investigated the complex behaviour of plasma in different physical systems. By modeling turbulence with simplified theories, we performed high resolution numerical simulations in order to understand nonlinear processes both in laboratory and space plasmas. The three complex phenomena that we treated can be summarized as follows:

1. The nonlinear dynamics of a compressible Hall Magnetohydrodynamic (HMHD) plasma have been investigated in a $2+\frac{1}{2}D$ geometric configuration, by performing direct numerical simulations. Two main features occur at small–scales where the Hall effect dominates, namely: i) an increase of the compressibility of the system and the breakdown of the strong link between velocity and magnetic field typical of usual MHD; ii) the excitation of small–scale fluctuations characterized by an anti–correlation between density and magnetic field intensity. Finally, we performed comparisons between our model's results and Cluster satellite data, which turn out to be in very good agreement.

2. We numerically investigated dynamics of two–dimensional $\mathbf{E} \times \mathbf{B}$ turbulence in a polar geometry, similar to a poloidal section of laboratory devices. The "bursty turbulence" has been generated and maintained by a random forcing term. Bursts (or *blobs*) interact and propagate radially before being absorbed by boundaries. Even if the model is very simple, a good agreement between simulation results and real data is observed, in particular concerning the shape of bursts, the electrostatic potential and the statistics of the radial flux. Some turbulent statistical properties of the "bursty turbulence" have been investigated and discussed.

3. Using a simplified model of Reduced MHD, obtained from a Galerkin approximation, we shown how the nonlinear dynamic of RMHD tur-

bulence, without dissipation, is able to generate a process of *self–organization* similar to an inverse cascade. A single Fourier mode dominates over the whole magnetic energy spectrum. Our results are roughly in agreement with the emergence of Quasi–single–Helicity states, commonly observed in several Reversed–Field Pinch experiments.

Being in good agreement with laboratory and space plasmas observations, results we obtained encourage us to continue, by using other numerical simulations, to investigate and to obtain a more detailed description of the plasma complexity. In future works we want to study the HMHD system in a 3D geometric approximation, with high resolution simulation, in order to get more information about the turbulent cascade process. Moreover we want to study the effect of the electron pressure gradient in the electric field and speculate about its influence in other space plasmas observations. By changing boundary condition in our code, we can also study the role of the Hall effect into other astrophysical plasmas as the *cusp region*, the *bow shock*, and the *solar wind*.
Also the work on the "bursty turbulence" is still in progress. We will perform longer and high–resolution simulations. Moreover, we will analyze burst shape by using more sophisticated techniques, as the Proper Orthogonal Decomposition (POD) [177]. As a general outlook, we think that this simple model can be implemented and, by introducing suitable boundary perturbations, the radially–outward flux of matter can be reduced. Through this, we can suggest a control strategy to increase confinement time inside devices, one of the most important challenge in the problem of thermonuclear energy production.

Bibliography

[1] Badii, R., Politi, A., *Complexity. Hierarchical Structures and Scaling in Physics*, Cambridge Univ. Press (1997).

[2] Anderson, P. W., *The Economy as an Evolving Complex System*, Addison Wesley Publishing Company (1988).

[3] Noback, C. R., Strominger, N. L., Demarest, R. J., Ruggiero, D. A., *The Human Nervous System: Structure and Function*, Humana Press (2005).

[4] Restrepo, J. G., Ott, E., Hunt, B. R., *Phys. Rev. Lett.*, **97**, 094102 (2006).

[5] Ott, E., *Chaos in Dynamical Systems*, Cambridge Univ. Press (1993).

[6] Eckmann, J. P., Ruelle, D., *Rev. Mod. Phys*, **57**, 617 (1985).

[7] Bohr, T., Jensen, M. H., Paladin, G., Vulpiani, A., *Dynamical Systems Approach to Turbulence*, Cambridge Univ. Press (1998).

[8] Kolmogorov, A. N., *Dokl. Akad. Nauk SSSR*, **30**, 9 (1941).

[9] Wootton, A. J., Carreras, B. A., Matsumoto, H., McGuire, K., Peebles, W. A, Ritz, C. P., Terry, P. W., Zweben, S. J., *Phys. Fluids B*, **2**, 2879 (1990).

[10] Hunt, J. C. R., Vassilicos, J. C., *Turbulence Structure and Vortex Dynamics*, Cambridge Univ. Press (2001).

[11] Pope, S. B., *Turbulent Flows*, Cambridge Univ., Cambridge, England (2000).

[12] Frisch, U., *Turbulence: the Legacy of A. N. Kolmogorov*, Cambridge Univ. Press (1995).

[13] R. Bruno, Carbone, V., *Living Rev. Solar Phys.*, **2**, 4 (2005).

[14] Biskamp, D., *Nonlinear Magnetohydrodynamics*, Cambridge Univ. Press (1997).

[15] Holmes, P., Lumley, J. L., Berkooz, G., *Turbulence, Coherent Structures, Dynamical Systems and Symmetry*, Cambridge Univ. Press (1998).

[16] Kivelson, G., Russell, C. T., *Introduction to Space Physics*, Cambridge Univ. Press (1995).

[17] Bateman, G., *MHD Instabilities*. Cambrige, MA: MIT Press (1978).

[18] Basu, S., MacKenzie, E., Coley, W. R., Sharber, J. R., Hoegy, W. R., *J. Geophys. Res.*, **95**, 7799 (1990).

[19] Tu, C. Y., Marsh, E., *Space Science Rev.*, **73**, Nos. 1–2 (1995).

[20] Tu, C. P., Marsh, E., *MHD Structures, Waves and Turbulence in the Solar Wind: Observations and Theories*, Kluwer Academic (1997).

[21] Sibeck, D. G., Paschmann, G., Treumann, R. A., Fuselier, S. A., Lennartsson, W., Lockwood, M., Lundin, R., Ogilvie, K. W., Onsager, T. G., Phan, T. -D., Roth, M., Scholer, M., Sckopke, N., Stasiewicz, K., Yamauchi, M., *Space Science Reviews*, **88**, 207 (1999).

[22] Escoubet, C. P., Schmidt, R., Goldstein, M. L., *Space Science Reviews*, **79**, 11 (1997).

[23] Horton, W., Crabtree, C., Doxas, I., Weigel, R. S., *Phys. Plasmas*, **9**, 3712 (2002).

[24] Chen, J., *Phys. Fluids B*, **5** , 2663 (1993).

[25] Bhattacharjee, A., Ma, Z. W., Xiaogang Wang *Phys. Plasmas*, **5**, 2001 (1998).

[26] Overskei, D., Politzer, P. A., *Phys. Fluids*, **19**, 683 (1976).

[27] Dunlop, M., Haaland, S., Balogh, A., Sonnerup, B., Glassmeier, K.-H., Soucek, J., Paschmann, G., Reme, H., Fazakerley, A., *Geophysical Research Abstracts*, **5**, 05154 (2003).

[28] Mozer, F. S., Bale, S. D., Phan, T. D., Osborne, J. A., *Phys. Rev. Lett.*, **91**, 245002 (2003).

[29] Mozer, F. S., Bale, S. D., Phan, *Phys. Rev. Lett.*, **89**, 015002 (2002).

[30] Dunlop, M., Haaland, S., Balogh, A., Sonnerup, B., Glassmeier, K.-H., Soucek, J., Paschmann, G., Reme, H., Fazakerley, A., *EGS - AGU - EUG Joint Assembly, Abstracts from the meeting held in Nice*, 5154 (2003).

[31] Kaufmann, R. L., Konradi, A., *J. Geophys. Res.*, **78**, 6549 (1973).

[32] De Keyser, J., Darrouzet, F., Roth, M., Vaisberg, O. L., Rybjeva, N., Smirnov, V., Avanov, L., Nemecek, Z., Safrankova, J., *J. Geophys. Res.*, **106**, 25503 (2001).

[33] Mozer, F. S., Phan, T. D., Bale, S. D., *Phys. Plasmas*, **10**, 2480 (2003).

[34] Hasegawa, H., Fujimoto, M., Phan, T. -D., Reme, H., Balogh, A., Dunlop, M. W., Hashimoto, C., TanDokoro, R., *Nature*, **430**, 755 (2004).

[35] Fairfield, D. H., Otto, A, Mukai, T., Kokubun, S., Lepping, R. P., Steinberg, J. T., Lazarus, A. J., Yamamoto, T., *J. Geophys. Res.*, **105**, 21 (2000).

[36] Fujimoto, M., Terasawa, T., Mukai, T., Saito, Y., Yamamoto, T., Kokubun, S., *J. Geophys. Res.*, **103**, 4391 (1998).

[37] Wu, C. C., *Space Science Reviews*, **107**, 219 (2003).

[38] Drake, J. F., Gerber, J., Kleva, R. G., *J. Geophys. Res.*, **99** (A6), 11211 (1994).

[39] Stasiewicz, K., Shukla, P. K., Gustafsson, G., Buchert, S., Lavraud, B., Thide, B., Klos, Z. *Phys. Rev. Lett.*, **90**, 085002 (2003).

[40] Stasiewicz, K., *Phys. Rev. Lett.*, **93**, 125004 (2004).

[41] Krall, N. A., Trivelpiece, A. W., *Principles of Plasma Physics*, McGraw–Hill, New York (1973).

[42] Bishop, A. S., *Project Sherwood; the U.S. Program in Controlled Fusion*, Reading, Mass., Addison-Wesley Pub. Co. (1958).

[43] Wesson, J., *Tokamaks*, Oxford University Press, Oxford, United Kingdom (2003).

[44] Jenko, F., Dorland, W., Kotshenreuther, M., Rogers, B., N., *Phys. Plasmas*, **7**, 1904 (2000).

[45] Brochard, F., Gravier, E., Bonhomme, G., *Phys. Rev. E*, **73**, 036403 (2006).

[46] Carter, T. A., *Phys. Plasmas*, **13**, 010701 (2006).

[47] Matsumoto, H., Kojima, H., Miyatake, T., Omura, Y., Okada, M., Nagano, I., TsuiTsui, M., *Geophys. Res. Lett.*, **21**, 2915 (1994).

[48] Franz, J., Kintner, P., Pickett, J., *Geophys. Res. Lett.*, **1277** (1998).

[49] Ghosh, S., Siregar, E., Roberts, D. A., Goldstein, M. L., *J. Geophys. Res.*, **101**, 2493 (1996).

[50] Mangeney, A., Salem, C., Lacombe, C., Bougeret, J. -L., Perche, C., Manning, R., Kellogg, P. J., Goetz, K., Monson, S. J., Bosqued, J.-M., *Annales Geophysicae*, **17**, 307 (1999).

[51] Spangler, S., Fueselier, S. A., Fey, A., Anderson, G., *J. Geophys. Res.*, **93**, 845 (1988).

[52] Denton, R. E., Lessard, M. R., Labelle, J. W., Gary, S. P., *J. Geophys. Res.*, **103**, 23, 661 (1998).

[53] Stasiewicz, K., Khotyaintsev, Y., Berthomier, M., Wahlund, J.–E., *Geophys. Res. Lett.*, **27**, 173 (2000).

[54] Cattell, C. A., Dombeck, J., Wygant, J. R., Hudson, M. K., Mozer, F. S., Temerin, M. A., Peterson, W. K., Kletzing, C. A., Russell, C. T., Pfaff, R. F., *Geophys. Res. Lett.*, **26**, 425 (1999).

[55] Wardle, M., *Astrophysics and Space Science*, **292**, 317 (2004).

[56] Balbus, S. A., Terquem, C., *The Astrophysical Journal*, **552**, 235 (2001).

[57] Boyd, T. J. M., Sanderson, J. J., *The Physics of Plasmas*, Cambridge Univ. Press (2003).

[58] Cao, F., Kan J., R., *J. Geophys. Res.*, **96** (A4), 5859 (1991).

[59] Dmitruk, P., Matthaeus, W. H., *Phys. Plasmas*, **13**, 042307 (2006).

[60] Laveder, D., Passot, T., Sulem, P. L., *Phys. Plasmas*, **9**, 293 (2002).

[61] Laveder, D., Passot, T., Sulem, P. L., *Phys. Plasmas*, **9**, 305 (2002).

[62] Dreher, J., Laveder, D., Grauer, R., Passot, T., Sulem, P. L., *Phys. Plasmas*, **12**, 052319 (2005).

[63] Huba, J. D., Rudakov, L. I., *Phys. Rev. Lett.*, **93**, 175003 (2004).

[64] Huba, J. D., Rudakov, L. I., *Phys. Plasmas*, **10**, 3139 (2003).

[65] Ramos, J. J., Porcelli, F., Verástegui, R., *Phys. Rev. Lett.*, **89**, 055002 (2002).

[66] Deng, X. H., Matsumoto, H. *Nature*, **410**, 557 (2001).

[67] Knoll, D. A., Chacón, L., *Phys. Rev. Lett.*, **96**, 135001 (2006).

[68] Turner, L., *IEEE Transactions on Plasma Science*, **6**, 849 (1986).

[69] Ohsaki, S., *Phys. Plasmas*, **12**, 032306 (2005).

[70] Ilgisonis, V. I., *Plasma Phys. Control. Fusion*, **43**, 1255 (2001).

[71] Mininni, P. D., Alexakis, A., Pouquet, A., *J. Plasma Phys.*, in press.

[72] Mininni, P. D., Gómez, D., Mahajan, S. M., *The Astrophys. J.*, **587**, 472 (2003).

[73] Hirota, M., Yoshida, Z., Hameiri, E., *Phys. Plasmas*, **13**, 022107 (2006).

[74] Mahajan, S. M., Krishan, V., *Mon. Not. R. Astron. Soc.*, **359**, L27 (2005).

[75] Pu, Z. -Y. and Kivelson, M. G. *J. Geophys. Res.*, **88**, 841 (1983).

[76] Melrose, D. B., *Instabilities in Space and Laboratory Plasmas*, Cambridge Univ. Press (1995).

[77] Huba, J. D., *Phys. Rev. Lett.*, **72**, 2033 (1994).

[78] Lepping, R. P., Burlaga, L.F., *J. Geophys. Res.*, **84**, 7099 (1979).

[79] Petviashvili, V., Pokhotelov, O., *Solitary Waves in Plasmas and in the Atmosphere*, Gordon and Breach Science Publishers (1992).

[80] Shukla, P. K., *Phys. Rev. A*, **39**, 4758 (1989).

[81] Stasiewicz, K., Longmore, M., Shukla, P. K., Lavraud, B., Pickett, J., *Geophys. Res. Lett.*, **30**, 2241 (2003).

[82] Karpman, V. I., *Non–Linear Waves in Dispersive Media*, Pergamon Press, New York (1975).

[83] Infeld, E., Rowlands, G., *Nonlinear Waves, Solitons and Chaos*, Cambridge Univ. Press, U. K. (2000).

[84] Ohsawa, Y., *Phys. Fluids*, **29**, 1844 (1986).

[85] Ruderman, M. S., *J. Plasma Physics*, **67**, 271 (2002).

[86] Kolberg, Z., Liverts, E., Mond, M., *Phys. Plasmas*, **12**, 062113 (2005).

[87] Silin, I., Bücher, J., *Adv. Space Res.*, **37**, 1354 (2006).

[88] Rezeau, L., Belmont, G., Briand, C., Cornilleau–Wehrlin, N., Reberac, F., *Geophys. Res. Lett.*, **26**, (1999).

[89] Lühr, H., Klöcker, N., *Geophys. Res. Lett.*, **14**, 186 (1987).

[90] Treumann, R., Brostrom, L., LaBelle, J., Scopke, N., *J. Geophys. Res.*, **95**, 19099 (1990).

[91] Turner, J. M., Burlaga, L. F., Ness, N. F., Lemaire, J. F., *J. Geophys. Res.*, **82**, 1921 (1977).

[92] Krishan, V., Mahajan, S. M., *Phys. Fluids*, **16**, 4196 (2004).

[93] Matsumoto, Y., Hoshino, M., *J. Geophys. Res.*, **111**, A05213 (2006).

[94] Peyret, R., Taylor, T. D., *Computational Methods for Fluid Flow*, Springer–Verlag, New York (1983).

[95] Forsythe, G. E., Wasow, W. R., *Finite–Difference Methods for Partial Differential Equations*, Jhon Wiley & Sons, inc. (1960).

[96] Bender, C. M., Orszag, S. A. *Advanced Mathematical Methods for Scientists and Engeneers*, International Student Edition (1978).

[97] Press, W. H., Flannery, B. P., Teukolsky, S. A., Vetterling, W. T., *Numerical Recipes in FORTRAN 77: The Art of Scientific Computing*, Cambridge Univ. Press (1992).

[98] Guinot, V., *Godunov-type Schemes*, Elsevier Science (2003).

[99] Balsara, D., Spicer, D. S., *J. Comput. Phys.*, **149**, 270 (1999).

[100] Toro, E. F., *Shock–Capturing Methods for Free–Surface Shallow Flows*, John Wiley & Sons (2001).

[101] Liou, M. -S., Steffen, C. J., *J. Comput. Phys.*, **107**, 23 (1993).

[102] Brackbill, J. U., Barnes, D. C., *J. Comput. Phys.* **35**, 426 (1980).

[103] Dender, A., Kemm, F., Kröner, D., Munz, C. -D., Schnitzer, T., Wesenberg, M., *J. Comput. Phys.*, **175**, 645 (2002).

[104] Mininni, P. D., Gómez, D. O., Mahajan, S. M., *The Astrophys. J.*, **584**, 1120 (2003).

[105] Miura, A., *Phys. Rev. Lett.*, **49**, 779 (1982).

[106] Miura, A., Pritchett, P. L., *J. Geophys. Res.*, **87**, 7431 (1982).

[107] Miura, A., *J. Geophys. Res.*, **89** 801 (1984).

[108] Alfvén, H., *Phys. Rev.*, **107**, 632 (1957).

[109] Jha, R., Kaw, P. K., Mattoo, S. K., Rao, C. V. S., Saxena, Y. C., *Phys. Rev. Lett.*, **69**, 1375 (1992).

[110] Zweben, S., *Phys. Fluids*, **28**, 974 (1985).

[111] Krasheninnikov, S., *Phys. Lett. A*, **238**, 368 (2001).

[112] Terry, P. W., *Rev. Mod. Phys.*, **72**, 109 (2000).

[113] Zwebenb, S. J., Stotler, D. P., Terry, J. L., LaBombard, B., Greenwald, M., Muterspaugh, M., Pitcher, C. S., Hallatschek, K., Maqueda, R. J., Rogers, B., Lowrance, J. L., Mastrocola, V. J., Renda, G. F., *Phys. Plasmas*, **9**, 1981 (2002).

[114] Antar, G., Y., Devynck, P., Garbet, X., Luckhardt, S. C., *Phys. Plasmas*, **8**, 1612 (2001).

[115] Greenwald, M., *Plasma Phys. Controlled Fusion*, **44**, R27 (2002).

[116] Antar, G. Y., Krasheninnikov, S. I., Devynck, P., Doener, R. P., Hollmann, E. M., Boedo, J. A., Luckhardt, S. C., Conn, R. W., *Phys. Rev. Lett.*, **87**, 065001 (2001).

[117] Ratynskaia, S. V., Demidov, V. I., Rypdal, K., *Phys. Rev. E*, **65**, 066403 (2002).

[118] Antoni, V., Carbone, V., Martines, E., Regnoli, G., Serianni, G., Vianello, N., Veltri, P., *Europhys. Lett.*, **54**, 51 (2001).

[119] Hasegawa, A., Wakatani, M., *Phys. Rev., Lett.*, **50**, 682 (1983).

[120] Carbone, V., Lepreti, F., Veltri, P., *Phys. Rev. Lett.*, **90**, 055001 (2003).

[121] Kirnev, G. S., Budaev, V. P., Grashin, S. A., Gerasimov, E. V., Khimchenko, L. N., *30th EPS Conference on Contr. Fusion and Plasma Phys., St. Petersburg, ECA*, **27A**, P-3.121 (2003).

[122] Kirnev, G. S., Budaev, V. P., Grashin, S. A., Gerasimov, E. V., Khimchenko, L. N., *Plasma Phys. Controlled Fusion*, **46**, 621 (2004).

[123] Antar, G. Y., Counsell, G., Yu, Y., Labombard, B., Devynck, P.,*Phys. Plasmas*, **10**, 419 (2003).

[124] Sorriso–Valvo, L., Carbone, V., Veltri, P., Consolini, G., Bruno, R., *Geophys. Res. Lett.*, **26**, 1801 (1999).

[125] Yu, G. Q., Krasheninnikov, S. I., *Phys. Plasmas*, **10**, 4413 (2003).

[126] Nielsen, A. H., Pecsell, H. L., Rasmussen, J., *Phys. Plasmas*, **3**, 1530 (1996).

[127] Carter, T., *Bull. Am. Phys. Soc.*, **47**, 201 (2002).

[128] Martines, E., Hron, M., STückel, J., *Plasma Phys. Controlled Fusion*, **44**, 351 (2002).

[129] Oynes, F. J., Olsen, O. -M., Pécseli, H. L., Fredriksen, A., Rypdal, K., *Phys. Rev. E*, **57**, 2242 (1998).

[130] Carreras, B. A., *IEEE Trans. Plasma Sci.*, **25**, 1281 (1997).

[131] J. C., Perez, Horton, W., Bengston, R. D., Carter, T. A., *Phys. Plasmas*, **13**, 055701 (2006).

[132] Boedo, J. A., Rudakov, D., Moyer, R., Krasheninnikov, S., Whyte, D., McKee, G., Tynan, G., Schaffer, M., Stangeby, P., West, P., Allen, S., Evans, T., Fonck, R., Hollmann, E., Leonard, A., Mahdavi, A., Porter, G., Tillack, M., Antar, G., *Phys. Plasmas*, **8**, 4826 (2001).

[133] Endler, M., *J. Nucl. Mater.*, **84**, 266 (1999).

[134] Hassan, A., Kulsrud, K., *Phys. Fluids*, **22**, 2097 (1979).

[135] Horton, W., *Phys. Fluids B*, **1**, 524 (1989).

[136] Diamond, P., Hahn, T., *Phys. Plasmas*, **2**, 3640 (1995).

[137] Newman, D., Carreras, B., Diamond, P., Hahm, T., *Phys. Plasma*, **3**, 1858 (1996).

[138] Politzer, P. A., *Phys. Rev. Lett.*, **84**, 1192 (2000).

[139] Smolyakov, A., Diamond, P., Malkov, M., *Phys. Rev. Lett.*, **84**, 491 (2000).

[140] Manfredi, G., Roach, C. M., *Phys. Plasmas*, **10**, 2824 (2003).

[141] Boffetta, G., Carbone, V., Giuliani, P., Veltri, P., Vulpiani, A., *Phys. Rev. Lett.*, **83**, 4662 (1999).

[142] Krommes, A., Ottaviani, M., *Phys. Plasmas*, **6**, 3731 (1999).

[143] Antoni, V., Carbone, V., Cavazzana, R., Regnoli, G., Vianello, N., Spada, E., Fattorini, L., Martines, E., Serianni, G., Spolaore M., Tramontin, L., Veltri, P., *Phys. Rev. Lett.*, **87**, 045001 (2001).

[144] Spada, E., Carbone, V., Cavazzana, R., Fattorini, L., Regnoli, G., Vianello, N., Antoni, V., Martines, E., Serianni, G., Spolaore, M., Tramontin, L., *Phys. Rev. Lett.*, **86**, 3032 (2001).

[145] Danaila, L., Anselmet, F., Zhou, T., Antonia, R. A., *J. Fluid Mech.*, **430**, 87 (2001).

[146] Monin, A. S., Yaglom, A. M., *Statistical Fluid Mechanics*, **2**, MIT Press, Cambridge (1975).

[147] Bak, P., Tang, C. and Wiesenfeld, K., *Phys. Rev. Lett.*, **59**, 381 (1987).

[148] Sreenivasan, K. R., Bershadskii, A., *J. Fluid Mech.*, **554**, 477 (2006).

[149] Martin, P., *Plasma Phys. Controlled Fusion*, **41**, A247 (1999).

[150] Escande, D. F., Martin, P., Ortolani, S., Buffa, A., Franz, P., Marrelli, L., Martines, E., Spizzo, G., Cappello, S., Murari, A., Pasqualotto, R., Zanca, P., *Phys. Rev. Lett.*, **85**, 1662 (2000).

[151] Spizzo, G., Franz, P., Piovesan, P., Predebon, I., Bolzonella, T., Cappello, S., Cravotta, A., Escande, D. F., Frassinetti, L., Ortolani, S., Paccagnella, R., Terranova, D., the RFX team, Chapman, B. E., Craig, D., Prager, S. C., Sarff, J.S., the MST team, Brunsell, P., Malmberg, J. -A., Drake, J., the EXTRAP T2R team, Yagi, Y., Koguchi, H., Hirano, Y., the TPE-RX team, White, R. B., Sovinec, C., Xiao, C., Nebel, R. A., Schnack, D. D., *Nucl. Fusion*, **43**, 1855 (2003).

[152] Marrelli, L., Martin, P., Spizzo, G., Franz, P., Chapman, B. E., Craig, D., Sarff, J. S., Biewer, T. M., Prager, S. C., Reardon, J. C., *Phys. Plasmas*, **9**, 2868 (2002).

[153] Ho, Y. L., Schnack, D. D., Nordlund, P., Mazur, S., Satherblom, H. -E., Scheffel, J., Drake, J. R., *Phys. Plasmas*, **2**, 3407 (1995).

[154] Cappello, S., Escande, D. F., *Phys. Rev. Lett.*, **85**, 3838 (2000).

[155] Montgomery, D., *Plasma Phys. and Contr. Fusion* , **34**, 1157 (1992).

[156] Shan, X., Montgomery, D., *Plasma Phys. Controlled Fusion*, **35**, 619 (1993).

[157] Strauss, H. R.,*Phys. Fluids*, **19**, 134 (1976).

[158] Rosenblut, M. N., Monticello, D. A., Strauss, H. R., White, R. B., *Phys. Fluids*, **19**, 1987 (1976).

[159] Zank, G. P., Matthaeus, W. H., *J. Plasma Phys.*, **48**, 85 (1992).

[160] Dubois, T., Jauberteau, F., Temam, R., *Dynamic Multilevel Methods and the Numerical Simulation of Turbulence*, Cambridge Univ. Press (1999).

[161] Servidio, S., Carbone, V., *Phys. Rev. Lett.*, **95**, 045001 (2005).

[162] Holmes, J. A., Carreras, B. A., Hender, T. C., Hicks, H. R., Lynch, V. E., An, Z. G., Diamond, P. H., *Physics of Fluids*, **28**, 261 (1985).

[163] Franz, P., Marrelli, L., Piovesan, P., Chapman, B. E., Martin, P., Predebon, I., Spizzo, G., White, R. B., Xiao, C., *Phys. Rev. Lett.*, **92**, 125001 (2004).

[164] Kusano, K., Sato, T., *Nucl. Fusion*, **30**, 2075 (1990).

[165] Martin, P., Buffa, A., Cappello, S., D'Angelo, F., Franz, P., Marrelli, L., Martines, E., Ortolani, S., Spizzo, G., Bilato, R., Bolzonella, T., Costa, S., Murari, A., Paccagnella, R., Pasqualotto, R., Terranova, D., Zanca, P., *Phys. Plasmas*, **7**, 1984 (2000).

[166] Martin, P., Marrelli, L., Spizzo, G., Franz, P., Piovesan, P., Predebon, I., Bolzonella, T., Cappello, S., Cravotta, A., Escande, D. F., Frassinetti, L., Ortolani, S., Paccagnella, R., Terranova, D., the RFX team, Chapman, B. E., Craig, D., Prager, S. C., Sarff, J. S., the MST team, Brunsell, P., Malmberg, J. -A., Drake, J., the EXTRAP T2R team, Yagi, Y., Koguchi, H., Hirano, Y., the TPE-RX team, White, R. B., Sovinec, C., Xiao, C., Nebel, R. A., Schnack, D. D., *Nucl. Fusion*, **43**, 1855 (2003).

[167] Finn, J. M., Nebel, R., Bathke, C., *Physics of Fluids B*, **4**, 1262 (1992).

[168] Carbone, V., Veltri, P., *Astron. Astrophys.*, **259**, 359 (1992).

[169] Huang, K., *Statistical Mechanics*, John Wiley & Sons, (1990).

[170] Fyfe, D., Montgomery, D., *J. Plasma Phys.*, **16**, 181 (1976).

[171] Kraichnan, R. H., Montgomery, D., *Rep. Prog. Phys.*, **43**, 547 (1980).

[172] Stribling, T., Matthaeus, W. H., *Phys. Plasmas*, **2**, 1979 (1990).

[173] Horbury, T. S., Forman, M. A., Oughton, S., *Plasma Phys. Control. Fusion*, **47**, B703 (2005).

[174] Franceschini, V., *Physica (Amsterdam)*, **6** D, 285 (1983).

[175] Piovesan, P., Craig, D., Marrelli, L., Cappello, S., Martin, P., *Phys. Rev. Lett.*, **93**, 235001 (2004).

[176] Malara, F., Veltri, P., Carbone, V., *Phys. Fluids B*, **4**, 3070 (1992).

[177] Vecchio, A., Carbone,V. , Lepreti, F., Primavera, L., Sorriso–Valvo, L., Veltri, P., Alfonsi, G., Straus, Th., *Phys. Rev. Lett.*, **95**, 061102 (2005).